Correlative FIB-SEM and TEM investigation of the magnesium electrode

Andrzej Sankowski

University of Nottingham

School of Chemistry

A thesis submitted for the degree of Doctor of Philosophy

Nottingham, September 2024

Declaration of Originality

I, Andrzej Sankowski, hereby declare that this doctoral thesis has been written by myself, is the result of my own scientific research and has not been submitted in candidature for any other degree.

Signature:

Abstract

The lithium-ion battery (LIB) has been at the forefront of innovations in energy storage since its commercialisation over 30 years ago. As we reach the practical specific capacity limit of current state-of-the-art materials, novel and innovative battery technologies are required to satiate the requirements of energy intensive applications such as electric vehicles. A lithium metal negative electrode has been proposed to increase the energy density. However, the high reactivity causes poor cycling performance due to electrolyte degradation, dendrite formation and safety issues. The magnesium electrode offers a solution that has double the theoretical volumetric capacity of the lithium electrode while simultaneously mitigating dendritic growth, reducing raw material costs and greatly increasing sustainability. Previous work has shown that traditional LIB electrolytes are not compatible with magnesium metal, and the plating and stripping mechanism that underpins how magnesium electrodes cycle is poorly understood.

Here the mechanism of magnesium plating and stripping in glyme-based electrolytes is explored with various additional additives. This thesis show that in the pure electrolyte solution, interphase formation is critical to stable cycling but that this is accompanied by significant degradation and accumulation of inactive Mg. It establishes the three-dimensional chemical composition of Mg deposits in the different electrolyte formulations using a combination of focused ion beam-scanning electron microscopy (FIB-SEM), energy dispersive x-ray spectroscopy (EDX) and transmission electron microscopy (TEM). We use these findings to develop a mechanistic understanding of the electrochemical cycling performance of magnesium metal negative electrodes. In situ electrochemical quartz crystal microbalance (EQCM) measurements are used to evaluate the plating and stripping efficiency of the electrodes and to identify non-electrochemical degradation reactions between Mg and the electrolyte solutions.

Publications

1) Wadge, M. D., Bird, M. A., **Sankowski, A.**, Constantin, H., Fay, M. W., Cooper, T. P., O'Shea, J.N., Khlobystov, A. N., Walsh, D. A., Nanostructured, Alkaline Titanate-Converted, and Heat-Treated Ti6Al4V Microspheres via Wet-Chemical Alkaline Modification and their ORR Electrocatalytic Response. Adv. Mater. Interfaces, **2023**, 10, 2201523
2) Dimogiannis,K., **Sankowski**, **A.,** Holc, C., Parmenter, C. D. J., Newton, G. N., Walsh, D. A., O'Shea, J., Khlobystov, A. N., Johnson, L. R., Structure and chemical composition of the Mg electrode during cycling in a simple glyme electrolyte. Energy Storage Mater., **2024,** 67, 103280. https://doi.org/10.1016/j.ensm.2024.103280
3) **Sankowski, A.,** O'Shea, J., Khlobystov, A. N., Johnson, L. R., Structural and chemical composition of the Mg electrode in a chloride glyme electrolyte (In draft)
4) **Sankowski. A.,** O'Shea, J., Khlobystov, A. N., Johnson, L. R., Oxygen evolution reaction activity of Cobalt oxide encapsulated in Multiwalled carbon nanotubes (In draft)

Acknowledgements

Firstly, I would like to thank my supervisors Prof Lee Johnson, Prof Andrei Khlobystov and Dr James O'Shea for the opportunity to undertake a PhD and for their advice and encouragement during these 4 years of my study. I would also like to thank Prof Graham Newton and Prof Darren Walsh for their academic support as well.

I'd also like to thank both the Nottingham Applied Materials & Interfaces and Nottingham Nanocarbon group members, both former and current for their encouragement, discussions, and pleasant working environments to grow over the last 4 years. In particular, I'd like to thank Dr Konstantinos Dimogiannis for his mentorship during the start of my studies and his contribution towards the electrochemical work in Chapter 3. I'm also grateful for the help provided by the nano and microscale research centre during my PhD and especially Dr Christopher Parmenter and Dr Michael Fay for their help with FIB-SEM and TEM respectively.

Also, many thanks to my friends Dr Ganesh Vailaya, Miss Jo Searle and Miss Margaret Smith for supporting me through my PhD and for making it a very enjoyable 4 years. I'd like to express my gratitude to my mother and my sister, Alexandra and Alicja, for their love and support through my life along with Cookie, Figure Ac. Finally, I'd like to thank my late father, Andrew who passed away during my studies, for always encouraging me to do my best and always being there for me when I needed someone to talk to, you may be gone but you'll never be forgotten.

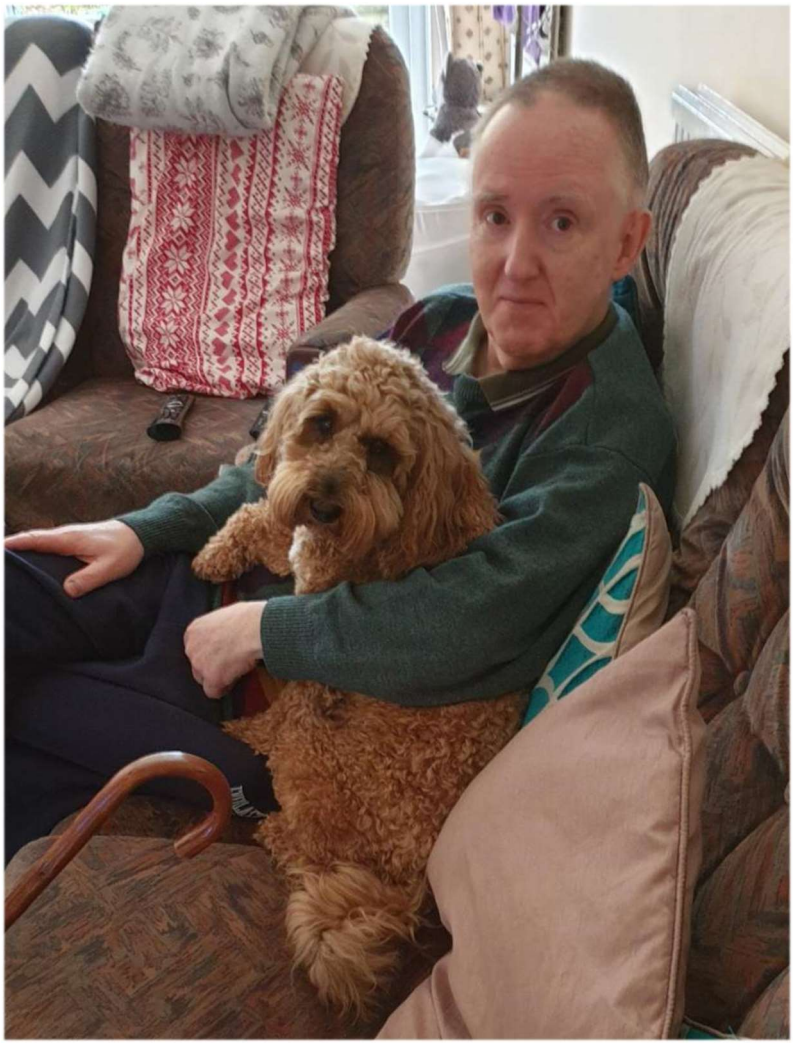

Figure Ac, A photo of my dad and our dog Cookie.

List of Abbreviations

1G	1,2-dimethoxyethane
2G	Diglyme
4G	Tetraglyme
A/B	Salt A dissolved in solvent B
APC	All phenyl complex
$Bi(OTf)_3$	Bismuth Triflate
CE	Coulombic efficiency
CEI	Cathode Electrolyte Interphase
CV	Cyclic voltammogram
DME	1,2-dimethoxyethane
EDX	Energy Dispersive X-ray Spectroscopy
EELS	Electron Energy Loss Spectroscopy
EQCM	Electrochemical quartz crystal microbalance
FEG	Field emission gun
FFT	Fast Fourier Transform
FIB	Focused Ion Beam
FIB-SEM	Focused Ion Beam Scanning Electron Microscopy
FTIR	Fourier-transform Infrared
GC	Glassy carbon
HFIP	Hexafluoroisopropanol

ICPMS	inductively coupled plasma mass spectrometry
IL	Ionic liquid
LCO	Lithium cobalt oxide
LIB	Lithium-ion battery
LiTFSI	lithium bis(trifluoromethanesulfonyl)imide
LMIS	Liquid metal ion source
LSV	Linear Sweep Voltammetry
m.p.e	Mass per electron
MACC	Magnesium aluminium chloride complexes
$Mg(BH_4)_2$	Magnesium borohydride
$Mg(TFSI)_2$	Magnesium bis(trifluoromethanesulfonyl)imide
$Mg[Al(hfip)_4]_2$	Magnesium tetrakis(hexafluoroisopropoxyl)aluminate
$Mg[B(hfip)_4]_2$	Magnesium tetrakis(hexafluoroisopropyloxy)borate
NMC	Lithium nickel manganese cobalt oxide
NMR	Nuclear Magnetic Resonance
$Pyr_{14}TFSI$	1-butyl-1-methylpyrrolidinium bis(trifluoromethanesulfonyl)imide
RE	Reference Electrode
RHE	Reversible hydrogen electrode

RMB	Rechargeable magnesium battery
SEI	Solid electrolyte interphases
SEM	Scanning Electrochemical Microscopy
SSI	Serial Slice and Imaging
STEM	Scanning transmission electron microscopy
TEM	Transmission Electron Microscopy
THF	Tetrahydrofuran
WE	Working Electrode
XPS	X-ray Photoelectron spectroscopy

Contents

Chapter 1: Introduction

1.1 Background

A major issue facing society today is that of climate change caused by global warming.[1] Since pre-industrial levels human-induced global warming has contributed to a global increase of approximately 1 °C, as shown in Figure 1.1a.[2] Fossil fuels such as oil, gas, and coal have been a key contributor to this increase.[1,3] In 2022, 331.5 Mtons of CO_2 were released into the atmosphere in the UK, with the largest contributors being transport and energy supply (Figure 1.1b).[3] The large, and over the past few decades increasing, consumption of fossil fuels and release of greenhouse gases has led to the general increase seen in global temperatures over this period, Figure 1.1a.[2,4]

In order to curb the impact of greenhouse gas emissions and keep the temperature increase below the COP26 climate summit goal of 1.5 °C by 2050.[5] Part of this goal can be achieved by transitioning away from combustion fuel sources to renewable sources of energy, such as wind and solar, and increasing the pace at which people transition to the use of electric vehicles.[5–7] Although the uptake of renewable energy sources is key, these sources can be intermittent, meaning any excess energy that they produce must be stored and used during peak hours. Additionally, the current mileage on current electric vehicles is low relative to their high cost.[6] Both of these issues would benefit from the improvement and development of current and future battery technologies.[8]

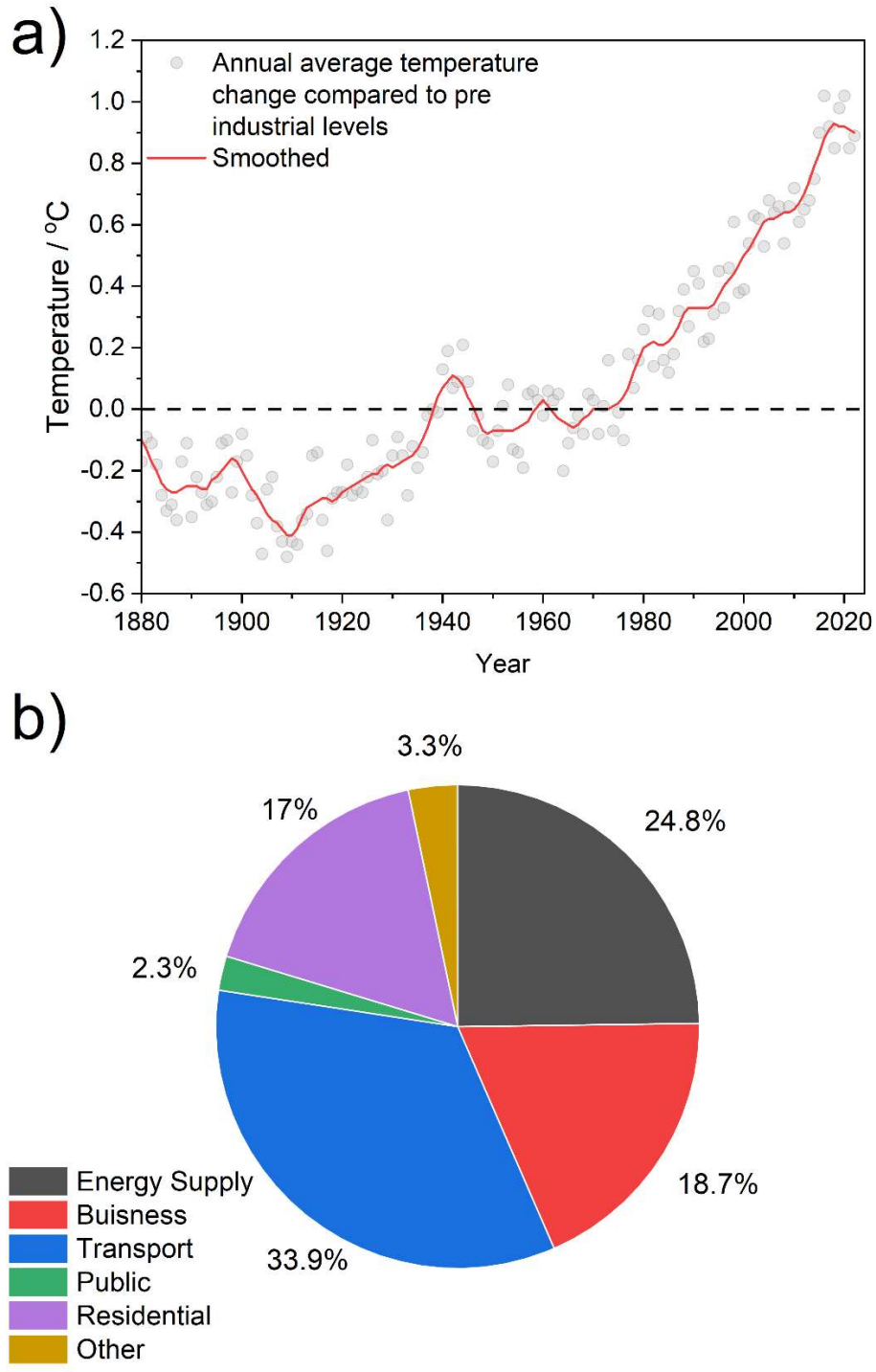

Figure 1.1, (a) the change in surface temperature each year between 1880 and 2022 relative to 1950-1980 average levels, dashed line[2] (b) percentage contributions to the total CO_2 emissions on the UK in 2022.[3]

1.2 Lithium-ion batteries

Fossil fuels revolutionised society, allowing the production of energy and fuel for transportation. Then, society was changed again with the development of lithium-ion batteries (LIBs).[9] The chemistry underpinning LIBs was discovered through research efforts in the 1980s, led by John Goodenough, Stanley Whittingham, and Akira Yoshino, who were awarded the Nobel Prize in Chemistry in 2019 for their contributions.[10,11] Following their initial breakthrough, LIBs were first commercialised in 1991 by Sony and have since allowed for the development of portable consumer electronics and, more recently, electric vehicles.[12]

The chemicals and structure of each component have changed over the years since their initial development. Now, current LIBs consist of a graphite negative electrode, a non-aqueous electrolyte, a separator, and a lithiated layered transition metal oxide, typically a cobalt oxide positive electrode.[13] Lithium-ion research in recent years has focused on finding a way to extract the last bits of available capacity from the battery through different positive electrode compositions, different electrolytes and lithium metal anodes.[14–16] In addition to the small amount of capacity that research is trying to extract from this technology, LIBs do have drawbacks.[17] Furthermore, some of the materials required for LIBs are found in politically unstable regions, such as cobalt which is mostly mined in the Democratic Republic of Congo.[18]

Many potential alternatives to LIBs have been investigated, such as the lithium-air battery, the lithium-sulfur battery and the magnesium battery, the latter of which this thesis will focus on.[19–21] Magnesium batteries present a potential alternative to LIBs as magnesium possesses a low reduction potential (-2.37 vs reversible hydrogen electrode (RHE)), high volumetric capacity (3833 mAh cm^{-3}) and is 1000x more abundant, which makes it an ideal anode material, a comparison between properties of magnesium and lithium is shown in table 1.[22,23] Magnesium batteries can't compete with LIBs in terms energy density for small scale applications, but they can for heavy load ones. Although

the advantages that magnesium batteries possess over LIBs, the research output in the area is lacking compared to that of LIBs, Figure 1.2.

Table 1.1, Comparison of properties between magnesium and lithium on their use in batteries.[22,24,25]

Properties	Magnesium Mg^{2+}	Lithium Li^{+}
Reduction potential / V vs RHE	-2.37	-3.04
Volumetric capacity / mAh cm^{-3}	3833	2046
Specific capacity / mAh g^{-1}	2205	3861
Cost / \$ kg^{-1}	2.5	13
Abundance / ppm	14000	13
Ionic radius / Å	0.72	0.76

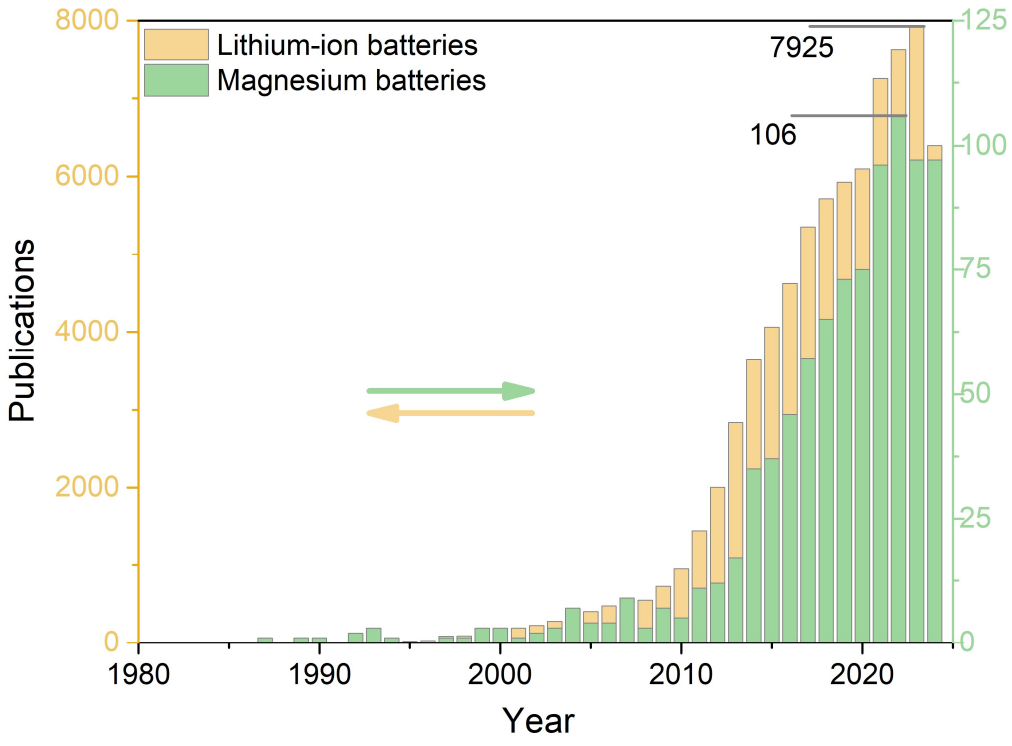

Figure 1.2, Comparison of the number of publications each year for searching "Lithium-ion batteries" and "Magnesium batteries" on Web of Science (as of 26/9/2024)

1.3 Magnesium batteries

1.3.1 Magnesium battery development

The rechargeable magnesium battery (RMB) was initially proposed in 1990 and began by investigating the nonaqueous electrochemistry of magnesium to evaluate the feasibility of making a secondary magnesium battery.[26] Although this work showed promise the nature of the electrolyte meant that the system suffered from poor anodic stability.[23] This initial work paved the way for Aurbach who developed a prototype system in 2000.[27]

The components of a magnesium cell are very similar to that of a LIB. It contains a positive electrode, typically consisting of an intercalation material such as molybdenum sulfide or vanadium oxide.[28,29] The negative electrode is normally magnesium metal as it is safe to handle and has a high volumetric capacity.[30] Electrolytes for magnesium vary in composition from Grignard's reagents to borohydrides and to halide free systems.[31–33]

In the years since this pioneering work, research has focused on looking into novel materials for magnesium battery cathodes for higher current density, electrolyte salts which aren't damaging to cell components and solvents which have a wide, stable voltage window.[34,35] Even though there have been significant advancements in these areas over the last couple of decades RMBs are still a long way off being commercialised because of two major issues. The first major issue which hinders the further development of RMBs and their commercialisation is that the positive electrodes are hindered by poor intercalation kinetics and the slow diffusion of Mg^{2+} through the structure due to the interaction between the magnesium di-cation and the anions of the host lattice.[36,37] The second hurdle research needs to overcome is that the current electrolyte systems are not compatible with both the magnesium negative electrode and the positive intercalation electrode, with the primary challenge being the reactivity of metallic magnesium. This is due to the passivation of the electrode surface with most common battery solvents, such as carbonates, and impurities which form a layer which is impermeable to Mg^{2+}.[21,26,38,39]

1.3.2 Magnesium battery electrolyte development

The electrolyte choice in RMBs has a large impact on the performance of the battery and its potential application, as it can affect the solubility of magnesium salts, the mobility of Mg^{2+} and the efficiency of magnesium plating and stripping.[35,40] As mentioned previously, impurities in the electrolytes cause the formation of passivation layers on the magnesium electrode surface; water impurities allow for the formation of MgO and $Mg(OH)_2$, which is impermeable to Mg^{2+}.[23] In addition to this, electrolyte salts can also decompose to form MgO, MgS and MgF_2, which are also impermeable to Mg^{2+}.[40] Also, due to the reactivity of magnesium most common battery solvents such as carbonates and salts such as PF_6^- and incompatible with magnesium.[41,42] The development of magnesium electrolytes since the initial work by Gregory et al. in 1990 has primarily focused on organic ether-based electrolytes.[26]

The original work by Gregory et al. laid the foundation for future developments into all phenyl complex (APC) electrolyte solutions, which are among the most widely used electrolyte systems for RMBs.[26,35] This work showed that RMBs were technically feasible, but the solvent/salt combination used at the time meant that the oxidative stability of the solvent was limited, which in turn limits the options for cathodes which can be used.[26] In the year 2000, a prototype system was developed by Aurbach et al. and managed to overcome the issue of limited oxidative stability by using a different electrolyte formulation.[27] The initial work by Gregory et al used magnesium organoborate electrolyte salts in tetrahydrofuran (THF) and these electrolytes were only stable up to a potential of ~1.9 V vs Mg^{2+}/Mg (Figure 1.3 a and b) whereas Aurbach's work with organomagnesium chloroaluminate salts in THF was stable up to a potential ~ 2.4 V vs Mg^{2+}/Mg (Figure 1.3 c).[27] This work was later built upon by Aurbach to use different glyme solvents such as tetraglyme (4G) and 1,2-dimethoxy ethane (DME).[43] In this work, it was also shown that in this electrolyte, the plating/stripping efficiency was 100 %, and the coulombic efficiency (CE) was 99.6 %, indicating that very little charge went into side processes such as electrolyte degradation.

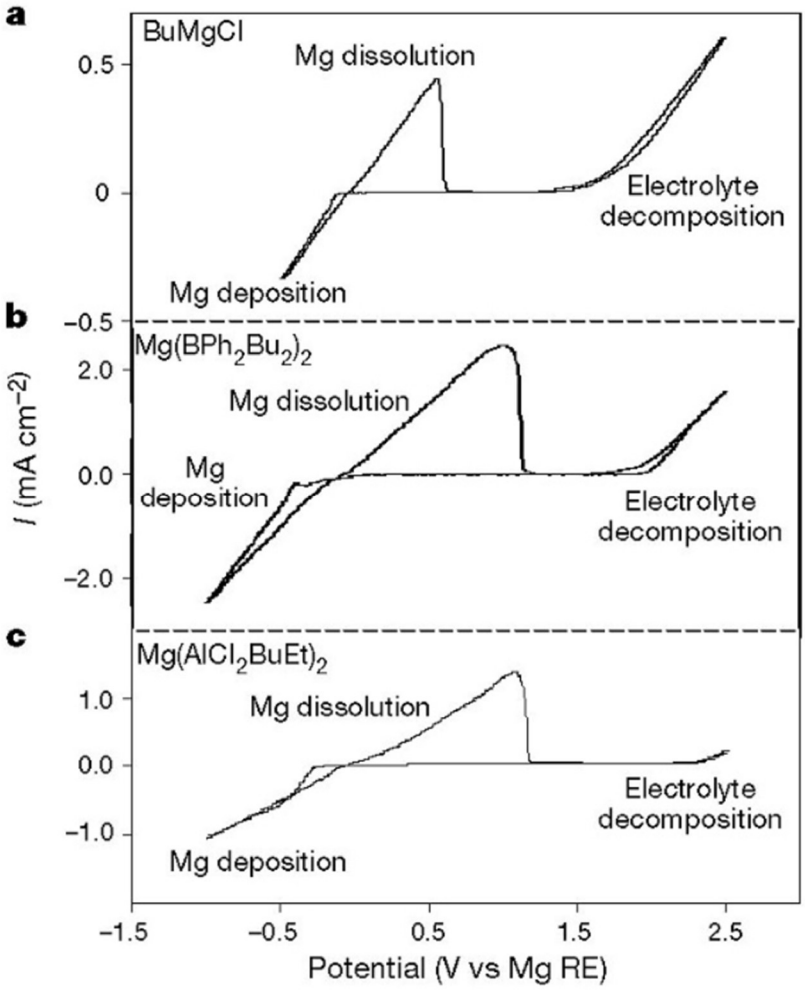

Figure 1.3, Comparison of cyclic voltammograms (CV)s of different electrolyte solutions for magnesium batteries. (a) 2 M BuMgCl in THF, (b) 0.25 M $Mg(BPh_2Bu_2)_2$ in THF and (c) 0.25 M $Mg(AlCl_2BuEt)_2$ in THF. Reproduced from Aurbach et al.[27]

Amido magnesium halides were another electrolyte salt introduced with organomagnesium halides. Liebenow et al. first tested these salts in the early 2000s, with the best-performing salt being hexamethyldisilazide magnesium chloride (HMDS MgCl).[44] This electrolyte combination performed better than the organoborates used by Gregory et al and enabled a similar workable potential window to the organomagnesium chloroaluminate electrolytes.[26,44]

These electrolyte combinations were the main focus of research until 2012.[45–48] The disadvantage of using chlorides is that they can be corrosive, thus making the RMB impractical.[49] Due to the corrosive nature of chloride, Mohtadi et al.

proposed the use of borohydride-based electrolytes.[49] Reversible magnesium plating and stripping were shown in 0.5 M $Mg(BH_4)_2$ in THF and had a CE of 40 %, Figure 1.4a. This showed that magnesium could be plated and stripped in chloride-free electrolytes, but the CE is poor, and there's a large overpotential between the plating and stripping of magnesium.

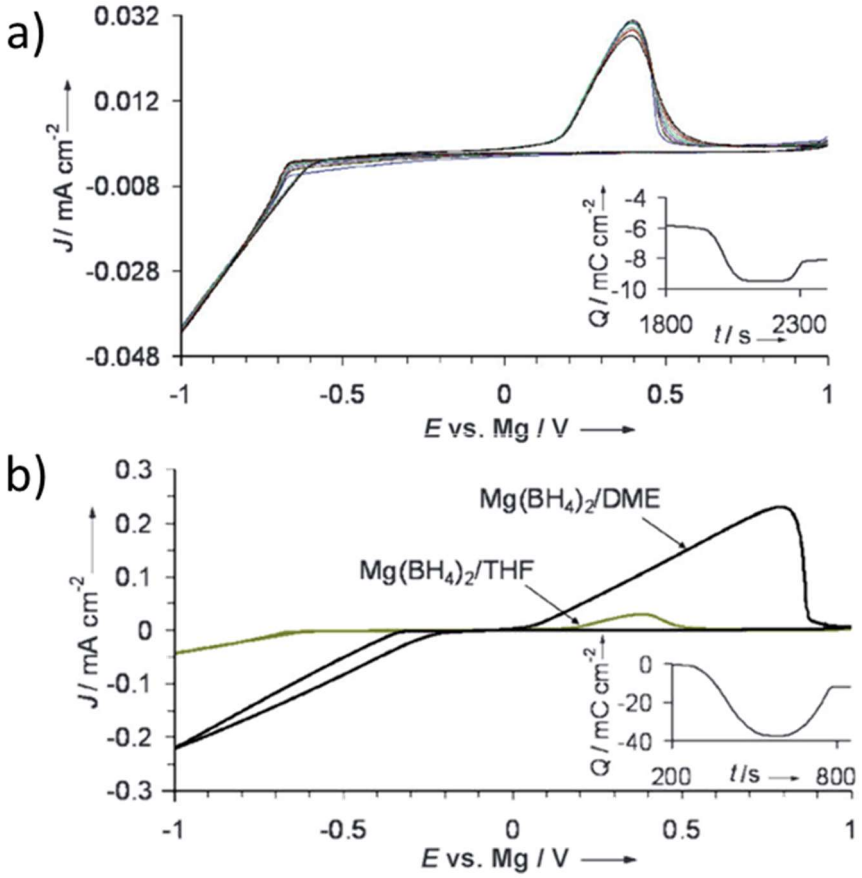

Figure 1.4, (a) Cyclic voltammogram of 0.5 M $Mg(BH_4)_2$/THF with the insert showing plating/stripping charge, and (b) Cyclic voltammogram of 0.1 M $Mg(BH_4)_2$/DME compared to 0.5 M $Mg(BH_4)_2$/THF with the insert showing the plating and stripping charge. All done at a Pt working electrode and Mg counter and reference. Reproduced from Mohtadi et al .[49]

However, making a simple change, such as replacing THF with DME, decreased the overpotential from 0.8 V to 0.37 V vs Mg^{2+}/Mg, respectively, along with an improvement in coulombic efficiency.[49] This is in contrast to organomagnesium electrolytes which perform better in THF.[50] This showed that testing different solvents for new electrolyte salts is crucial for finding the ideal system. This was

continued by Shao et al. in 2013, who investigated the effect that different solvents have on the coordination of magnesium and its plating and stripping.[51] This work supported the idea of testing different ethereal solvents to get the ideal electrolyte system.

In 2014, two other electrolyte salts started gaining research interest: magnesium aluminium chloride complexes (MACC) and magnesium bis(trifluoromethanesulfonyl)imide ($Mg(TFSI)_2$).[52,53] MACC electrolytes typically consist of $MgCl_2$ and $AlCl_3$ salts in ether solvents and show highly reversible electrodeposition of Mg and an electrochemical window limit of 3.1 V vs Mg^{2+}/Mg along with a high CE of 98.8 %.[52] Later work on MACC electrolytes showed that aluminium is deposited on the magnesium electrode surface during the early cycles, which does impact the CE. However, it stabilises the formation of charged species through a pre-treatment process called "conditioning," which subsequently leads to better plating and stripping of Mg in later cycles.[35,54] Conditioning is a process through which the electrochemical reversibility of Mg plating and stripping increases, the current density and CE increase, and the overpotential decreases over repeated cycling.[55] This occurs through the removal of impurities in the electrolyte during those initial cycles. Although the MACC electrolytes move away from the Grignard reagents, which are highly corrosive and have a lower electrochemical window limit, they still contain chloride species, which limits the electrolyte stability, the choice of current collector and cathode material.[56]

$Mg(TFSI)_2$ ether-based electrolytes also started gaining interest in 2014, following work initially done by Choi et al.[53] These electrolytes showed a much higher electrochemical window of 4.0 V vs Mg^{2+}/Mg and allowed Al to be used as a current collector, which isn't the case with organohaloaluminate-based electrolytes that do not contain any chloride salts.[53] However, the CE is below that of chloride-containing systems. To improve these electrolytes, the following year, Aurbach et al. added $MgCl_2$ to the $Mg(TFSI)_2$ electrolyte and recorded CEs of >99% when there was 0.25 M $Mg(TFSI)_2$ and 0.5 M $MgCl_2$ in DME (Figure 1.5).[57]

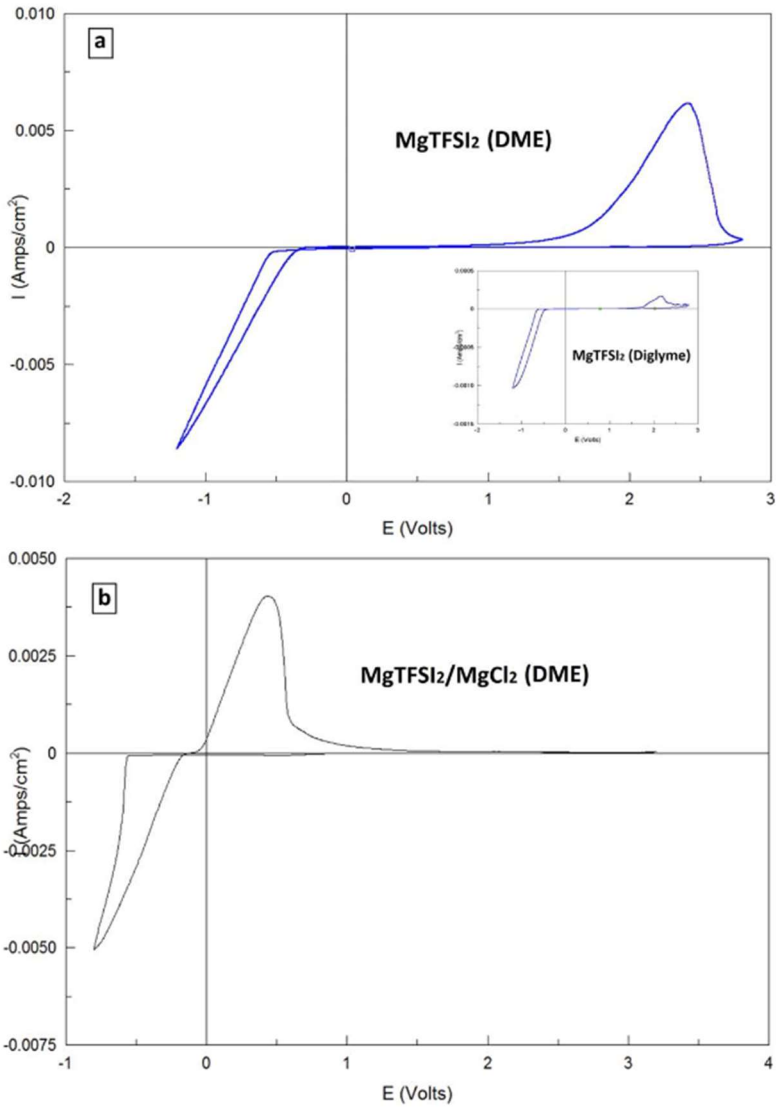

Figure 1.5 (a) CV of 0.5 M $Mg(TFSI)_2$ in DME with the insert being in diglyme (b) 0.25 M $Mg(TFSI)_2$ and 0.5 M $MgCl_2$ in DME. These were recorded at a Pt working electrode with a Mg reference and counter at a scan rate of 25 mV s^{-1}, reproduced from Aurbach et al.[57]

The CV shown in Figure 1.5a shows that without chloride, high overpotentials are required to strip and plate Mg in both DME and diglyme (2G), about -0.7 V vs Mg^{2+}/Mg for plating Mg and 1.5 V vs Mg^{2+}/Mg for stripping Mg. This led to an overall CE of these TFSI glyme electrolytes of about 60 %, which is far below the efficiency needed.[57] This can be attributed to a passivating layer forming on freshly deposited Mg metal.[58]

It was also shown that the addition of $MgCl_2$ gave solutions which allow for improved reversibility of Mg plating and stripping, with significantly reduced overpotentials for both, Figure 1.5b. Although an increase in performance was seen following the addition of $MgCl_2$ the reversibility couldn't exceed 80 -90 %. This was attributed to the impurities from $Mg(TFSI)_2$. Boro-hydride and organo-metallic-based electrolytes in ethers are quite reductive, so they are able to remove most of the impurities, including water, oxygen and carbon dioxide.

In order to improve the electrochemical performance of these electrolytes, they carried out a procedure referred to as conditioning, which is believed to remove the impurities.[59] These conditioned electrolytes allow for a CE of 98 % and when electrochemical quartz crystal microbalance (EQCM) measurements showed that all the deposited Mg was stripped, Figure 1.6. From their measurements, a mass per electron (m.p.e) was calculated as being 9.39, where the ideal value for Mg plating and stripping is 12. This discrepancy is due to the fact that the Sauerbrey equation doesn't take into account that each solution will have different viscoelasticity and the viscosity-density product of the solution.[60]

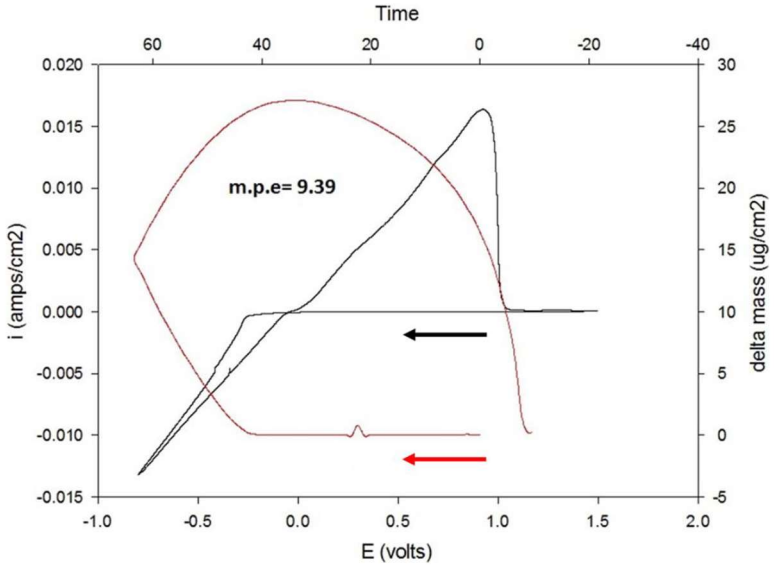

Figure 1.6 EQCM response for both CV (black) and electrode mass change (red) of Mg plating and stripping in 0.25 M $Mg(TFSI)_2$ and 0.5 M $MgCl_2$ in DME at a Pt working electrode with a Mg counter and reference electrode. Reproduced from Aurbach et al.[57]

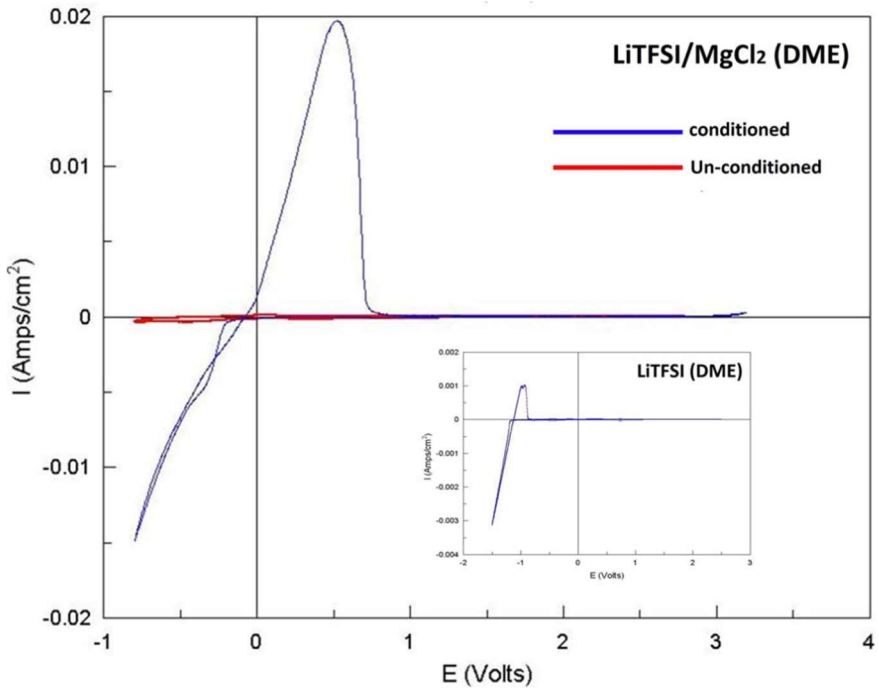

Figure 1.7 Comparison between conditioned (blue) and unconditioned (red) LiTFSI 0.5 M and $MgCl_2$ 0.125 M in DME at a Pt working electrode and a Mg counter and reference electrode. Insert shows Li plating and stripping of 0.5 M LiTFSI DME solution. Reproduced from Aurbach et al.[57]

As well as adding $MgCl_2$ to $Mg(TFSI)_2$ ether electrolytes this work also replaced $Mg(TFSI)_2$ with lithium bis(trifluoromethanesulfonyl)imide (LiTFSI). This was done because LiTFSI is available highly pure and dry, reducing the chances for impurities to affect performance. Although the electrolyte purity was higher by using LiTFSI and $MgCl_2$ in DME, the initial electrochemical response for Mg plating and stripping was poor, but once the electrolyte had undergone a conditioning stage, there was a vastly improved electrochemical response, Figure 1.7. Overall, this work showed that the addition of $MgCl_2$ to $Mg(TFSI)_2$/DME solutions can significantly improve the performance and that conditioning the electrolyte beforehand can lead to improved cycle life and efficiency, most likely by the removal of impurities in the electrolyte.

The most recent electrolytes to have caught the interest of researchers are fluorinated alkoxy aluminate and fluorinated alkoxy borate electrolytes.[61,62] Magnesium tetrakis(hexafluoroisopropyloxy)aluminate ($Mg[Al(hfip)_4]_2$) was first tested in 2016, by Herb et al, and this salt could be synthesised in a one-

pot synthesis from dibutyl magnesium, trimethyl aluminium and hexafluoroisopropanol (HFIP), HFIP indicates the protonated alcohol species where hfip represents where the alcohol proton has been replaced by another bonding species.[63] Being chloride-free means these electrolytes won't be corrosive to standard cell components. The CE of these electrolytes can reach 99.3 % and although an initial overpotential of -0.8 V vs Mg^{2+}/Mg is seen for Mg plating, the value significantly reduced in two cycles to -0.35 V vs Mg^{2+}/Mg in DME. Additionally, depending on the electrode material used the electrolyte system is stable up to an oxidative potential of 4 V vs Mg^{2+}/Mg.

Magnesium tetrakis(hexafluoroisopropyloxy)borate ($Mg[B(hfip)_4]_2$) was first reported in 2017 by Fichtner et al. These salts can be easily synthesised in a simple reaction between $Mg(BH_4)_2$ and HFIP.[61] These electrolytes also benefit from being chloride-free, removing the corrosive and oxidative window limits and having a higher oxidation window, depending on electrode material (Figure 1.8b). Although this salt in DME has a higher positive potential window, a large overpotential can be required to start plating and stripping Mg onto the electrode surface, -0.72 V and 0.43 V vs Mg^{2+}/Mg, respectively. [61] These decrease to -0.4 V and 0.15 V vs. Mg^{2+}/Mg by cycle 3 and reach their maximum current density after 8 cycles (Figure 1.8a). The CE for this system was tested with galvanostatic cycling, and it had a coulombic efficiency of >98%, which is better than any other chloride-free electrolytes reported at that point.

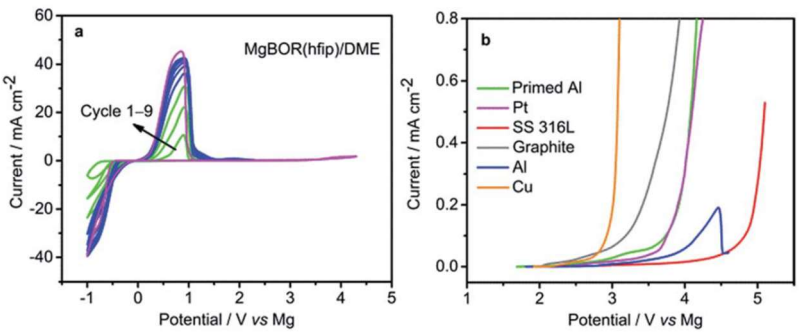

Figure 1.8 (a) CV of 0.6 M $Mg[B(hfip)_4]_2$ in DME with a Pt working electrode and Mg counter and reference electrode at a scan rate of 25 mV s^{-1}, (b) linear sweep voltammograms of different electrode materials at a scan rate of 25 mV s^{-1}, reproduced from Fichtner et al.[61]

Further work on these electrolyte systems by Aurbach showed that conditioning these electrolytes is similar to that used for the $Mg(TFSI)_2$ + $MgCl_2$/DME electrolyte.[64] This work showed that through conditioning the CE could be improved for CVs from 84 % to 95 %. They analysed the electrode surface deposits with inductively coupled plasma mass spectrometry (ICPMS) to try and detect any changes in composition pre and post-conditioning, and they saw that the amount of Mg on the surface after conditioning was closer to the expected value. Other than this change in ppm of Mg before and after conditioning, no other report has managed to determine definitively what happens during the conditioning process.

Since the development of these fluorinated alkoxy salts, groups have investigated which ether solvents allow for the best ion transport and conductivity. Mandai et al. investigated the effect of different glyme electrolytes on conductivity, cycling, viscosity, and many other parameters, which all affect the cell's viability.[65] This work looked at the impact of ether choice on both $Mg[B(hfip)_4]_2$ and $Mg[Al(hfip)_4]_2$ it found that the optimum concentration for each salt was 0.3 M, as concentration affects ionic conductivity, and the aluminate salt had a higher ionic conductivity than the borate salt at the same concentration, regardless of glyme length. Then, leading from this, the best salt glyme combination was $Mg[Al(hfip)_4]_2$/2G, as it allowed for efficient plating and striping of Mg over hundreds of cycles and a CE of 99.4 %.

Research has also looked into the solvents used, including adding cosolvents for selective solvation or additives that form artificial solid electrolyte interphases (SEI).[66–69] The idea of selective solvation for Mg is based on the fact that the main limit now on electrolyte solutions is the oxidative stability of the solvent and selective solvation can expand this. A recent example of this is from Hahn et al, who used hydrofluoroethers as the main solvent but also added either three equivalents or two equivalents of DME or 2G respectively per Mg.[66] This, in turn, allowed for higher solubilities up to 0.9 M and oxidative stability up to 4.4 V vs Mg^{2+}/Mg.

Artificial SEIs have been made from a range of different materials such as inorganic salts, alloys and polymers.[55,70–72] This artificial SEI, in addition to allowing for reversible plating and stripping, can allow the use of otherwise incompatible solvents such as propylene carbonate and ethylene carbonate.[73] The system that allowed for cycling in carbonates coated the Mg anode beforehand by adding polyethylene oxide and $Mg(TFSI)_2$ to a mix of Mg powder and super P carbon. This work showed that Mg could diffuse through the polymer coating allowing for reversible Mg plating and stripping as the coating contained channels for Mg^{2+} migration. [73] Although this methodology allows for the use of different solvents, it suffers from poor capacity retention over multiple cycles, starting at 75 mAh g^{-1} on cycle 1 and ending at 30 mAh g^{-1} at 40 cycles.

Another artificial SEI which has been reported was based on an ionic liquid additive.[67] In work by Yang et al., 10 mM 1-butyl-1-methylpyrrolidinium bis(trifluoromethane sulfonyl)imide ($Pyr_{14}TFSI$) was added to a standard electrolyte solution of 0.1 M $Mg(TFSI)_2$/DME and this additive solution is referred to as IL- $Mg(TFSI)_2$/DME. This work focused on the even distribution of Mg during plating, as Mg typically forms hemispherical structures due to inhomogeneity of the metal electrode surface, Figure 1.9a.[53,74,75] The work showed that the addition of this additive caused the ever-distribution of Mg across the surface (Figure 1.9b) and reduced electrolyte degradation at the Mg electrode, which is shown via Energy Dispersive X-ray Spectroscopy (EDX) (Figure 1.9c).[67] This work shows artificial SEIs can also be formed during cell cycling instead of being a pre-treatment.

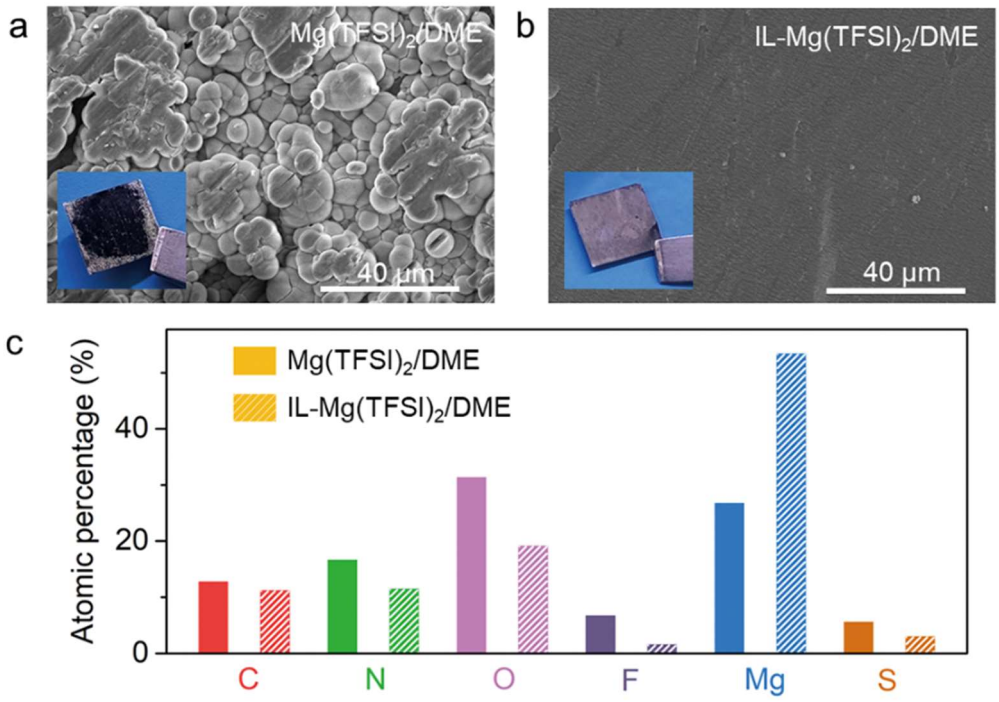

Figure 1.9 (a) SEM image of $Mg(TFSI)_2$/DME with an optical image as an insert, (b) SEM image of IL-$Mg(TFSI)_2$/DME with an optical image as an insert, (c) Elemental distribution in atomic percentage from EDX. All after 140 charge/discharge cycles at 0.1 mA cm^{-2}. Reproduced from Yang et al.[67]

Along with developing artificial SEIs, research has also looked into alloying Mg with different metals, such as zinc, indium, gallium, and bismuth, to help with the electrode's malleability, as Mg is difficult to manipulate.[76,77] Bismuth was one of the first elements to be alloyed with Mg due to its similar theoretical volumetric capacity (3783 mAh cm^{-2}) compared to Mg (3833 mAh cm^{-2}) and has good Mg cation diffusivity.[78] Bismuth was initially proposed by Arthur et al as an electrodeposited electrode for RMBs.[80] Bi could be used for Mg plating and stripping in conventional Mg electrolytes.[79–81] Unfortunately, using bismuth as an alloy with Mg has its own drawbacks. One of those is that during cycling, the alloy undergoes a volume expansion. This volume expansion can cause cracks, revealing fresh electrode material and leading to further electrolyte degradation.

Ideally instead of alloying two metals, there would be a surface layer of Bi which protects the Mg underneath whilst still allowing for reversible Mg plating

and stripping. This was done by Fichtner et al, when they added Bi triflate ($Bi(OTf)_3$) as an additive.[82] The addition of Bi triflate allowed for Mg plating and stripping with a high CE of 92.4 % in $Mg[B(hfip)_4]_2$ electrolytes, Figure 1.10a, compared to an electrolyte without the bismuth additive, which had a CE of 83.4 %. For galvanostatic cycling it also reduced a large over potential typically seen for the initial plating of Mg onto the electrode surface. This work also showed that this electrolyte system can tolerate a small quantity of water, 32 ppm H_2O, which is good considering typically the water content needs to be less than 10 ppm for chloride-free electrolytes to work. A schematic of the role of the Mg-Bi interphase is shown in Figure 1.10b and c. [82]

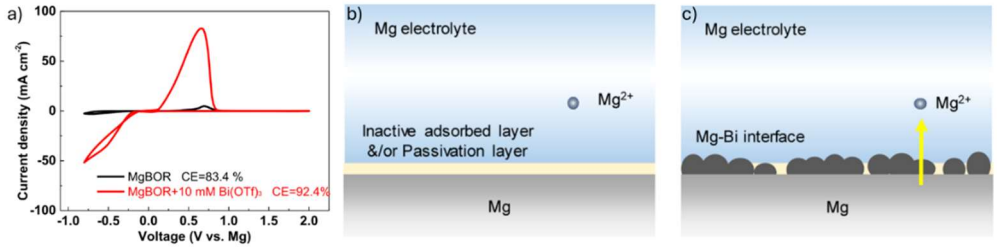

Figure 1.10 (a) CV of 0.3 M $Mg[B(hfip)_4]_2$/DME with and without 10 mM $Bi(OTf)_3$ (b) and (c) schematic of the role of the in situ interphase formed without and with $Bi(OTf)_3$ respectively. Reproduced from Fichtner et al. [82]

1.4 Interphase formation in battery systems

During operation of battery systems a SEI layer forms on the surface of the negative electrode and the layer which forms on the positive electrode is typically referred to as the cathode electrolyte interphase (CEI).[83] These interfacial layers initially form upon contact between the metal and the solution and grow through the first few cycles. These consists layers of insoluble and partially soluble products of electrolyte reactions.[84] In LIB systems the formation of the SEI is essential to the batteries performance and normally form during the first few cycles which impacts their performance during these initial cycles.

In lithium-ion systems the reduction of the salt ions forms inorganic compounds such as LiF, LiCl and Li_2O which all crash out of the electrolyte and precipitate on to the electrode surface. The main compound formed through the reaction of the electrolyte is Li_2CO_3 and partially soluble polymers.[84] Impurities in the electrolyte, such as water, can form other compounds such as LiOH and Li_2O_2. The combination of all these electrolyte degradation products means that the SEI has a complex chemical structure, Figure 1.11.

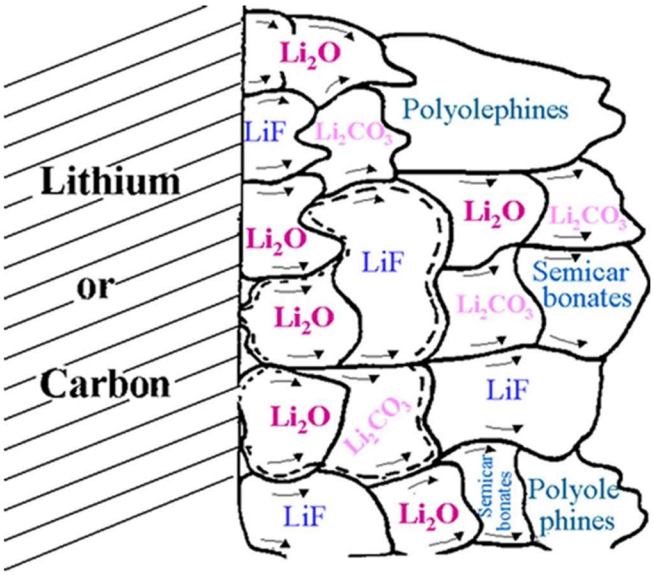

Figure 1.11, Schematic representation on the SEI formed on a lithium or carbon electrode.[84]

In an ideal LIB system, the SEI would form during the initial few cycles and prevent degradation of the electrolyte in further cycles, but this is far from reality. When lithium plates on to the anode surface it causes a volume expansion which can cause the SEI to crack, revealing 'fresh' lithium for the electrolyte to react with. The SEI can also be damage by the dendrites which form needle like structures which grow and pierce through the SEI, revealing a new channel for electrolyte to flow through and react with the electrode surface. These cause the SEI layer to grow progressively thicker over cycling and along with it reducing the amount of electrolyte present, impacting the cycling efficiency, and leading to eventually battery failure.

For RMBs an SEI also forms when the reduction potential is higher than that of Mg plating, the decomposition of the electrolyte on the Mg electrode can lead to the formation of an SEI.[85] Similar to that seen in LIBs it composes of inorganic Mg species such as MgO, MgF_2 and $Mg(OH)_2$, the latter being present when there are water impurities present. Then the ether solvents used also decompose into soluble organic species or thin films on the electrode surface. This interface layer is different to that seen in LIBs as the SEI in LIBs can effectively conduct ions through its structure. Whereas the layer formed in RMBs has poor Mg^{2+} conductivity, leading to sluggish transport, high impedance and large overpotentials.[86] The Mg anode also undergoes volume expansion which also causes the SEI to crack and break leading to further degradation.

1.5 Microscopy of battery materials

1.5.1 Overview of battery microscopy

The main microscopy methods used to investigate the surface of electrodes are scanning electron microscopy (SEM) and transmission electron microscopy (TEM) for microscale and nanoscale, respectively. With in situ techniques such as energy dispersive X-ray spectrometry (EDX) and electron energy loss spectroscopy (EELS), chemical information is gained alongside morphological information. Along with these non-destructive techniques, the internal structures can be imaged through the addition of a focused ion beam (FIB), which uses an ion beam to mill parts of the sample to reveal cross sections.

The development of FIB techniques, such as Focused ion beam scanning electron microscopy (FIB-SEM), was driven by the needs of a growing semiconductor industry in the 1970s.[87] It has since spread to all regions of research, including materials science, geological science, medicine, and biology. The development of cryo-FIB has allowed it to expand into the biomaterial characterisation of cells in a frozen state.[88–90] FIB can also be used to produce lamella or lift-outs of material. These are slices of a sample which are thinned to <100 nm and attached to a Cu support grid for TEM imaging and analysis.[91] In the area of battery research, microscopy is key as important processes occur on the electrode surface, be it the deposition of active material or the formation of an SEI, and these processes change the electrode's surface chemistry and structure.[83,92,93] The vast majority of imaging of battery materials is done ex-situ, as it doesn’t require specialist equipment. There have been some publications of in situ microscopy but these have been with specific conditions, such as ionic liquids (IL) used as the electrolyte. [94–96]

Electrode materials can vary in morphology, ranging from needle-like structures to some that resemble flowers and other impressive structures, Figure 1.12 a-d.[97,98] The shape, size, and distribution of these materials can greatly affect the cells' performance, as larger particles can lead to a lower utilization of active material.[99] Additionally, during cycling, these particle

structures can change through the formation of cracks, agglomeration of nano-particles or the formation of an SEI.

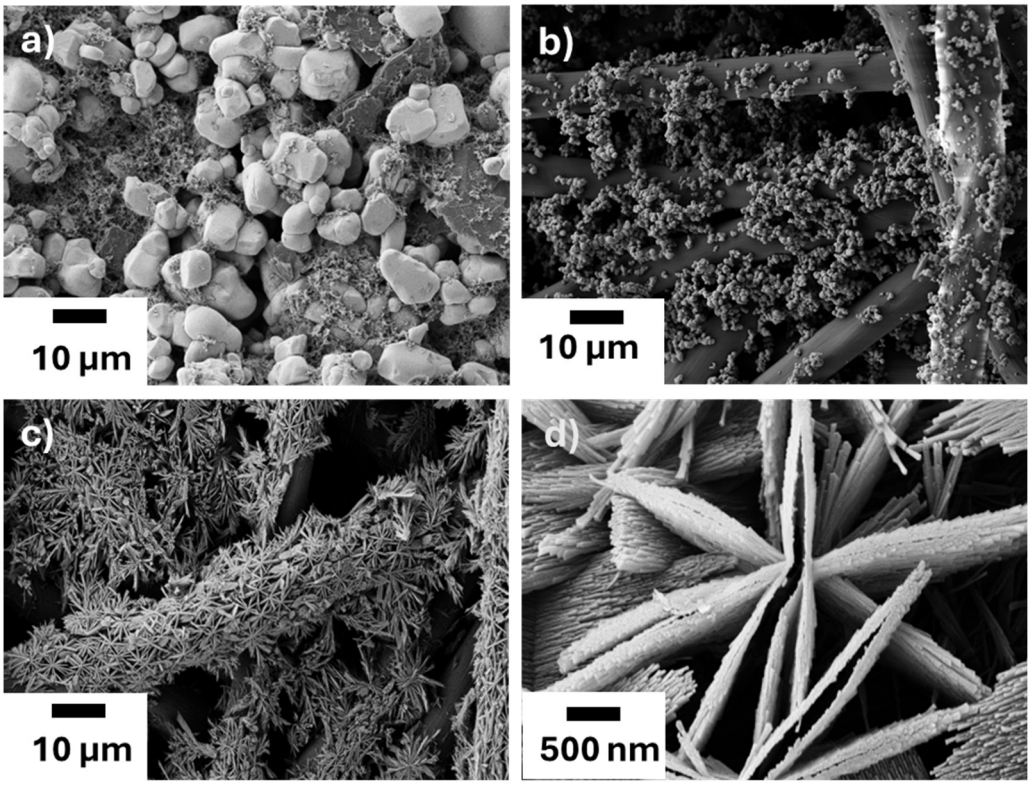

Figure 1.12 SEM images of (a) lithium ion NMC 811 cathode, (b) deposited lithium sulfide particles for a lithium-sulfur cathode and (c-d) lithium oxide deposits on a carbon lithium-air cathode. These images were acquired by the author.

1.5.2 Microscopy of Magnesium-ion batteries

In the magnesium battery literature publications typically include SEM images showing bulk deposition structures on the electrode surface but don't utilise all the complementary methods such as focused ion beam (FIB) and correlative techniques. Along with not fully utilising the full capabilities of microscopy there is no consistency in cycling conditions or electrode materials between different publications, to allow for direct comparisons between different systems and cycling conditions to see how they change the surface morphology. The differences between a selection of different literature publications are shown in Table 1.2.

The majority of electrodes imaged in literature are Mg metal electrodes which would show how the electrode morphology in a full RMB would develop through cycling. [70,100] However some literature also use electrode materials which would be impractical to use in a RMB, such as Pt.[64,101] In addition to this the majority of microscopy shown in literature which shows the surface morphology of the electrode lacks detail of the nanostructures on the surface, Figure 1.13 a-d.

The micrographs shown in Figure 1.13 show deposited Mg on an Pt electrode surface. These images show uniform deposition of Mg over the electrode surface with sharp, crystalline structures covering the electrode at 1 mA cm^{-2}, Figure 1.13a, at higher current densities, 5 mA cm^{-2}, the surface deposits are much smaller and rough but still equally distributed, Figure 1.13b. At these much higher current densities no dendritic structures were observed in the micrographs.[57] The main microscopy technique used for the analysis of the electrode surface structures is SEM which shows the microscale detail. The nanoscale interphase information and analysis of sample crystallinity can only truly be revealed with TEM, which in the field of Mg battery research has been heavily underutilised with only a few of papers including TEM analysis.[74,89,102] Along with mainly focussing on the surface morphology, there has been a scarce amount of research done on understanding the cycling mechanism of Mg deposition and deposit growth.[48,74,103]

Table 1.2, comparison between different microscopy conditions used in literature for Mg batteries, comparing electrode material, cycling conditions and microscopy techniques used.

Electrode material	*Cycling procedure*	*Current density/ scan rate/ specific capacity*	*Microscopy*	*Ref.*
Pt	1 deposition cycle	0.5, 1 and 5 mA cm^{-2}	SEM	64
Carbon fibre	3 hr deposition	1 mA hcm^{-2}	SEM	65
Mg	100 cycles	1 mA cm^{-2}	SEM	70
Ti	22 hr deposition	0.01 mA cm^{-2}	SEM	73
Mg	1 deposition cycle	1 mA cm^{-2}	SEM and TEM	74
Mg	400 cycles	1 mA cm^{-2}	SEM	100
Pt	1 deposition	1, 2.5 and 5 mA cm^{-2}	SEM	101
Mo_6S_8	20 cycles	50 mAh g^{-1}	TEM	102
Mg	10 cycles	0.5 mA cm^{-2}	SEM	104
Mg-Si	10 cycles	0.1 mA cm^{-2}	SEM	105
V_2O_5	6 cycles	0.2 mV s^{-1}	SEM	106

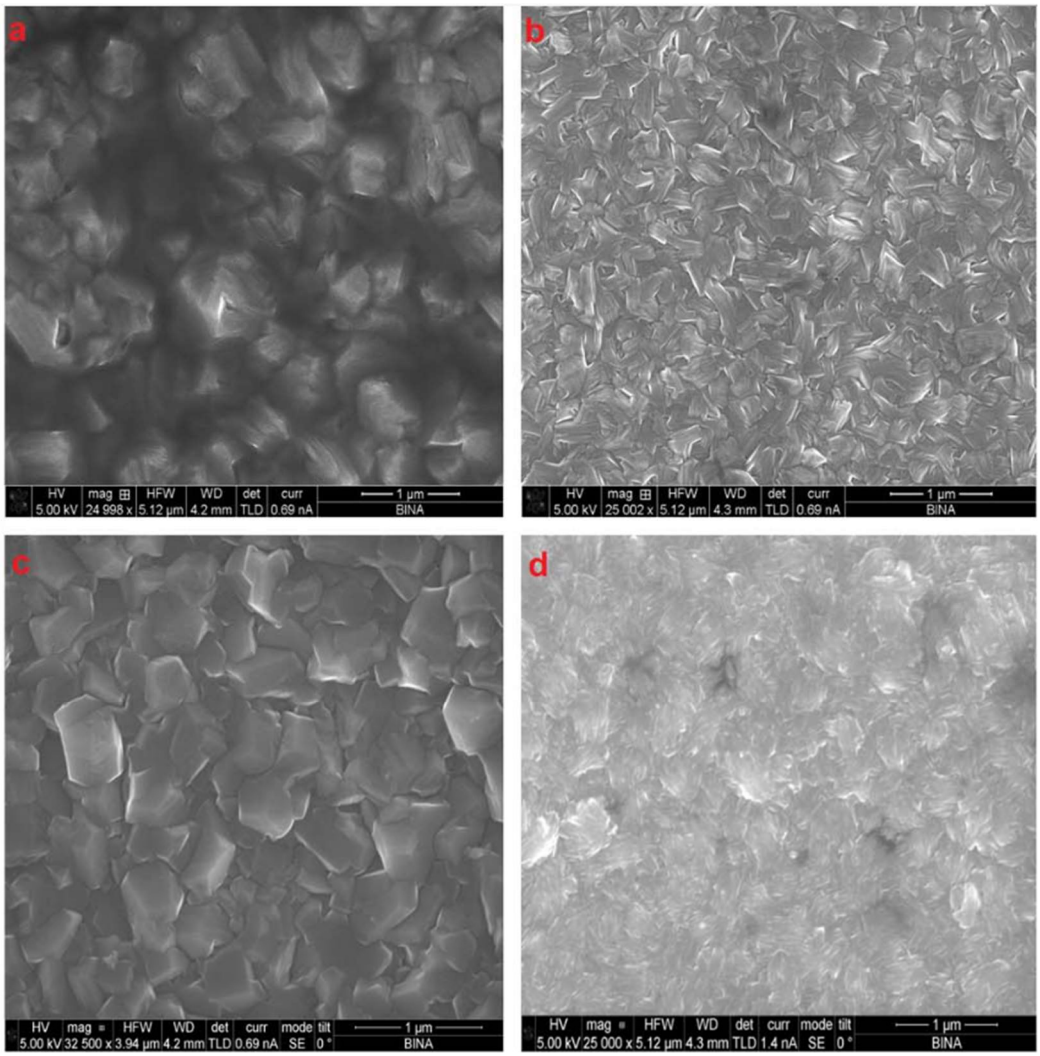

Figure 1.13, SEM images showing deposited Mg deposits on Pt in a 0.25 M $Mg(TFSI)_2$ + 0.5 M $MgCl_2$ in DME at 1 mA cm^{-2} (a) and 5 mA cm^{-2} (b) and 0.5 M Li(TFSI) + 0.125 M $MgCl_2$ in DME at 1 mA cm^{-2} (c) and 4 mA cm^{-2} in DME (d), adapted from Aurbach et al.[57]

Publications in more recent years have started to use more of the capabilities of microscopy techniques to better understand the surface structures that form in RMBS. Work by Banerjee et al used a combination of microscopy, diffraction and spectroscopy techniques to understand the structure and composition of fractal Mg dendrites.[74] A photograph of these fractal dendrites, Figure 1.14a, shows the intricate branch like structure of the dendrites which formed and show that they are similar to the dendritic structures seen in LIBs. The SEM and TEM micrographs, Figure 1.14 b and d, show the highly crystalline structure of the fractal deposits. This is supported by the x-ray diffraction pattern and select

area electron diffraction pattern obtained which also show the well-well developed crystalline structure.[74] The EDX maps show that the structures mainly consist of Mg in the core structure, whilst the maps for Cl, O and C show that they are mainly present on the dendrite surface, likely from electrolyte degradation on the Mg surface.

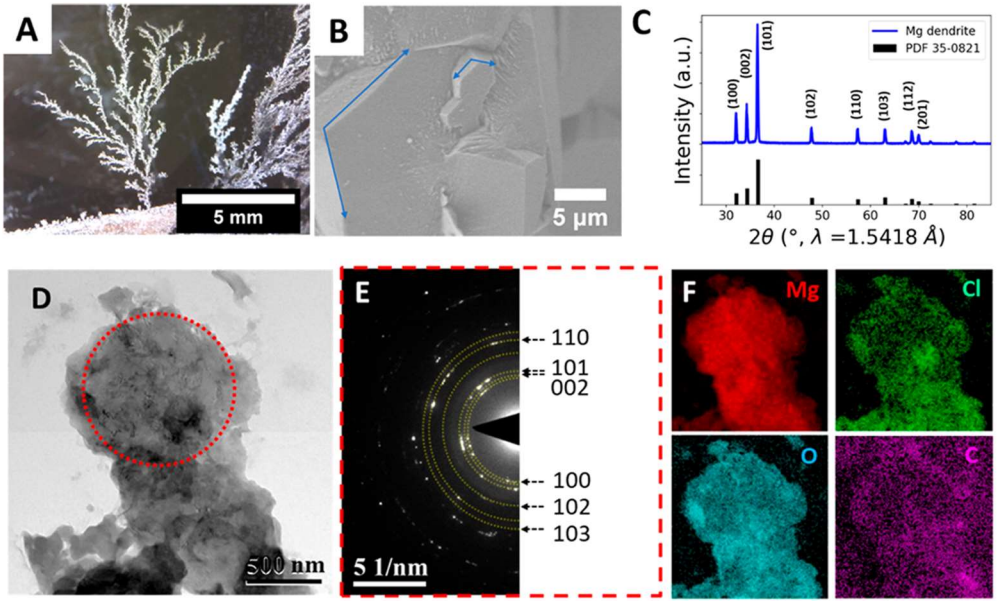

Figure 1.14, A photograph of a fractal Mg deposit (a), SEM image of a section of the structure (b), powder x-ray diffraction of a detached fractal structure (c), TEM image of a poly crystalline region of the Mg dendrite (d), SAED pattern of the region circled in d (e), EDX maps of the region imaged in d (f). Adapted from Banerjee et al.[74]

1.5.3 Microscopy of Lithium-ion batteries

For LIBs, microscopy has helped to understand important interfacial processes and structural changes. During the cycling of LIBs, the positive electrode undergoes structural and chemical changes. The intercalation and de-intercalation of lithium ions change the oxidation state of the metal oxide structure; for lithium cobalt oxide (LCO) cathodes, the Cobalt goes from 3+ to 4+ oxidation state and then back to $^{3+}$, which lithium intercalates back into the metal oxide lattice.[107] For lithium nickel manganese cobalt oxide (NMC) positive electrodes the changes in oxidation states are more complex, with having a mixture of different transition metals. In both LCO and NMC electrodes, during the intercalation and de-intercalation of lithium, the metal oxide clusters, like in Figure 1.15a, expand and contract respectively, and this volume fluctuation causes cracking in the metal oxide particles. This cracking leads to capacity decay and eventual failure of the battery, through further electrolyte degradation with the exposed transition metal oxide surface.[108–110] These cracks through the metal oxide particles can be imaged with FIB-SEM by cross-sectioning, Figure 1.15. Ruess et al showed that even after a single charge cycle, cracking occurs inside the metal oxide particles, Figure 1.15b. These cracks appear along the grain boundaries present in the particles and through extended cycling cause the particles to break up further.[111]

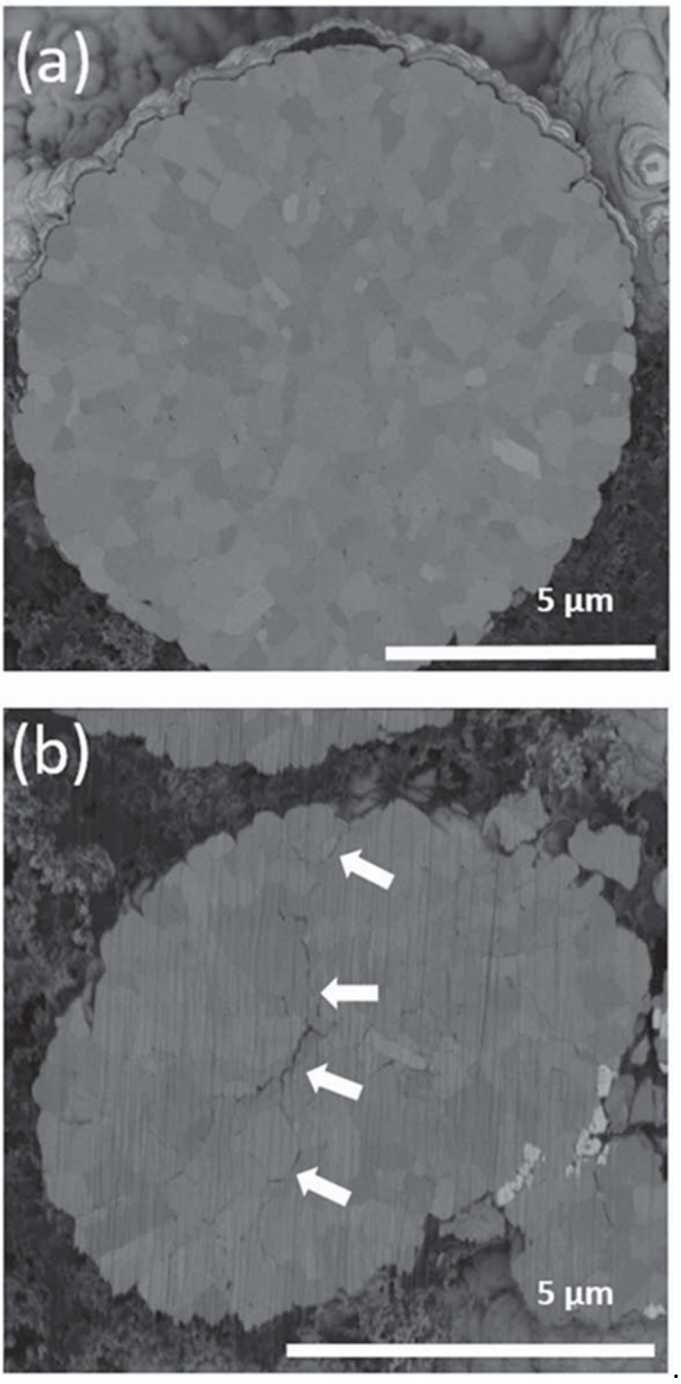

Figure 1.15, cross sectional SEM images of (a) pristine NMC particle and (b) a NMC particle after the 1st charging step. Adapted from Ruess et al.[111]

Microscopy techniques have also allowed for the analysis of the 3D chemical structures of dendrites that form on Li metal, which has aided in future solvent selection. Research by Zachman et al. investigated the 3D structure of the dendrites that formed during cycling using cryo-scanning transmission electron

microscopy (STEM).[112] Cryo-TEM and STEM were possible through vitrification, which is the process where samples are rapidly frozen to preserve any structures and keep them in their native state. By cycling a coin cell (Figure 1.16a) and then vitrifying the lithium-negative electrode, the dendrite structure was able to be maintained for the image (Figure 1.16b-d). In order to generate 3D structures of the dendrites, serial slice and imaging were used. This process involves capturing an image, milling, and a distance ~ 50 nm, and then capturing an image.

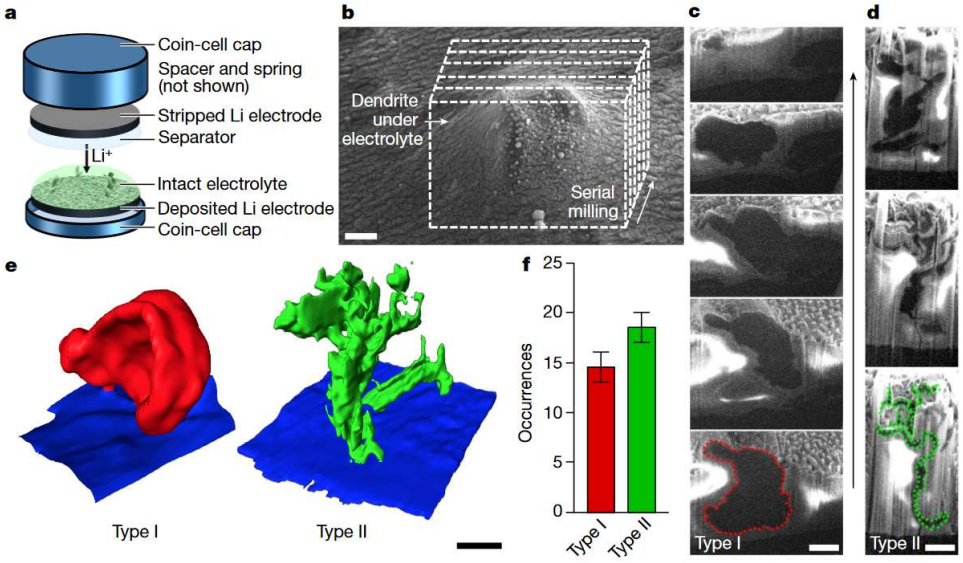

Figure 1.16 (a) coin cell diagram of cell, (b) SEM image of the area imaged through serial imaging, (c and d) cross-sectional images of two different dendrite morphologies present, (e) 3D structures of the two types of dendrite structure, scale bar 5 µm, and (f) the number of occurrences of each dendrite type. Adapted from Zachman et al.[112]

These images were then accumulated and processed to develop 3D structures, Figure 1.16e. The distribution of these structures was also investigated during imagining, Figure 1.16f, and the two types of dendrites were found to be similar. From the 3D structures, the contact area with the electrode could also be measured, and it was found that type 1 dendrites had a contact area a magnitude greater than type 2. Meaning type 2 dendrites may become disconnected more easily, leading to the loss of active material and capacity fade.

To obtain high-resolution structural and chemical data, a cryo-FIB lift-out was prepared through the method in Figure 1.17. The structure and composition of the lift-outs for both dendrites were analysed with electron energy loss spectroscopy (EELS) to determine elemental composition and distribution. From this analysis of the two structures present, it was seen that type 1 dendrites contain a relatively high amount of O, likely from electrolyte degradation, whilst type 2 dendrites formed from water impurities with there being a high presence of lithium hydride present in the EELS spectra.

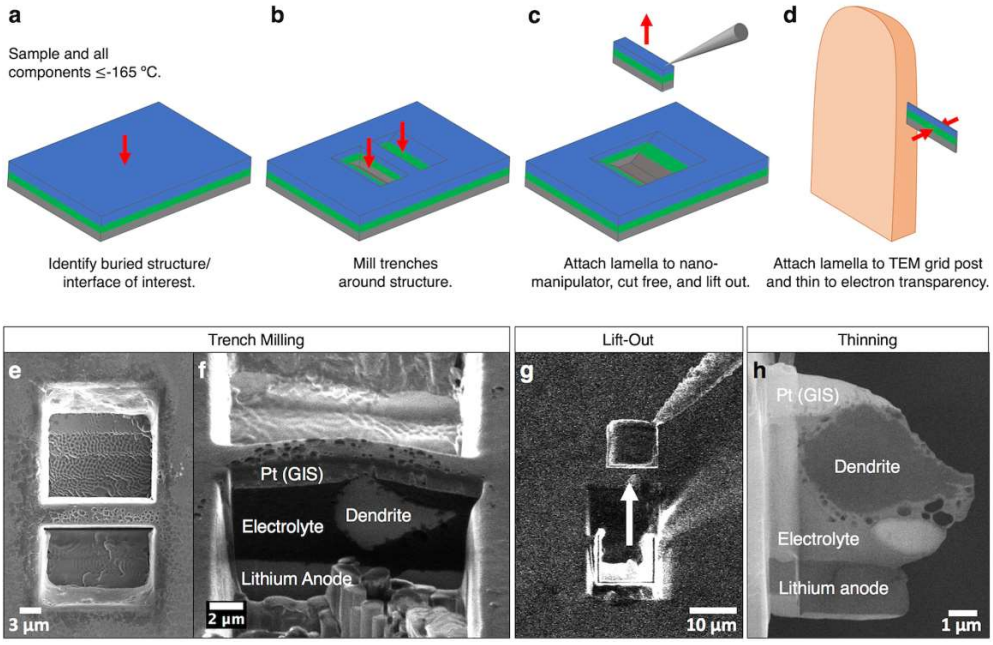

Figure 1.17 (a) a buried structure or interface is identified, (b, e and f) trenches formed either side of the sire of interest, (c and g) a cooled micromanipulator used to extract the lift-out, (d,h) lamella attached to the support grid. Adapted from Zachman et al.[112]

The electrolyte used was then substituted for a highly fluorinated electrolyte to minimise degradation. This change in electrolyte formulation suppressed the formation of type 2 dendrites and altered the deposition of the lithium. The effect of type 1 dendrites was that instead, they formed larger structures with sections separated by the SEI layer. The performance response also yielded higher coulombic efficiencies and a greatly reduced capacity fade. This work by Zachman et al. showed how a combination of correlative techniques can contribute to the development of better electrochemical systems, in this case, for lithium-ion.

The work published by Zachman et al shown in Figure 1.16 and 1.17 is an ideal workflow for thoroughly analysing surface structures and if similar workflow were to be developed for RMBs the understanding of the structures which form would be vastly improved. Thus, this workflow inspired most of the work presented in this thesis.

1.6 Motivation and Aims

Key processes of battery technology occur at the electrode interphase and for LIBs this has been thoroughly investigated and led to developments in the technology. For Mg batteries these processes haven't been investigated, leaving a gap in understanding for future development. The motivation for the work in Chapter 3 is to develop new workflows to better understand the interphase of the negative electrode in Mg batteries at both the nano and microscale. The knowledge gained from these workflows is crucial for understanding the chemical and structural changes that occur during cycling. This will be done through a combination of correlative microscopy techniques with complementary spectroscopy techniques.

Another challenge when going through literature of Mg batteries is being able to compare between different electrolyte systems. Different current densities and cycling times are used making comparisons difficult. The work in Chapter 4 aims to directly compare different prominent electrolytes from literature and apply the same cycling conditions to all of them to allow for direct comparison. The addition of microscopy techniques to this work links the surface structures observed to the cycling efficiency to develop a cycling mechanism for each system. Then Chapter 5 takes forward the best performing electrolyte system from Chapter 4 and applies the methodology developed in Chapter 3. In order to understand the cycling mechanism and surface and how the chemical and structural compositions change.

1.7 References

1 M. A. Hannan, S. B. Wali, P. J. Ker, M. S. A. Rahman, M. Mansor, V. K. Ramachandaramurthy, K. M. Muttaqi, T. M. I. Mahlia and Z. Y. Dong, *J. Energy Storage*, 2021, **42**, 103023.

2 Global temperature, https://climate.nasa.gov/vital-signs/global-temperature/, (accessed 2 January 2024).

3 Connor O'Sullivan, *2022 UK greenhouse gas emmissions: provisional figures*, 2023.

4 J. Gurney, *J. Policy Anal. Manag.*, 2019, **4**, 283.

5 COP26 goals, https://ukcop26.org/cop26-goals/, (accessed 27 May 2022).

6 D. Gielen, F. Boshell, D. Saygin, M. D. Bazilian, N. Wagner and R. Gorini, *Energy Strategy Rev.*, 2019, **24**, 38–50.

7 G. J. May, A. Davidson and B. Monahov, *J. Energy Storage*, 2018, **15**, 145–157.

8 G. N. Newton, L. R. Johnson, D. A. Walsh, B. J. Hwang and H. Han, *ACS Sustain. Chem. Eng.*, 2021, **9**, 6507–6509.

9 R. A. Easterlin, *J. Econ. Perspect.*, 2000, **14**, 7–26.

10 K. Mizushima, P. Jones, P. Wiseman and J. Goodenough, *Mater. Res. Bull.*, 1980, **15**, 783–789.

11 Y.-S. Hu and Y. Lu, *ACS Energy Lett.*, 2019, **4**, 2689–2690.

12 C. Vaalma, D. Buchholz, M. Weil and S. Passerini, *Nat. Perspect.*, DOI:10.1038/natrevmats.2018.13.

13 G. E. Blomgren, *J. Electrochem. Soc.*, 2017, **164**, A5019–A5025.

14 J. Alvarado, M. A. Schroeder, T. P. Pollard, X. Wang, J. Z. Lee, M. Zhang, T. Wynn, M. Ding, O. Borodin, Y. S. Meng and K. Xu, *Energy Environ. Sci.*, 2019, **12**, 780–794.

15 D. W. Abarbanel, K. J. Nelson and J. R. Dahn, *J. Electrochem. Soc.*, 2016, **163**, A522–A529.

16 D. Aurbach, E. Zinigrad, H. Teller and P. Dan, *J. Electrochem. Soc.*, 2000, **147**, 1274.

17 Y. Liang, C. Zhao, H. Yuan, Y. Chen, W. Zhang, J. Huang, D. Yu, Y. Liu, M. Titirici, Y. Chueh, H. Yu and Q. Zhang, *InfoMat*, 2019, **1**, 6–32.

18 Z. Zhao-Karger and M. Fichtner, *Front. Chem.*, 2019, **7**, 1–12.

19 J.-H. Kang, J. Lee, J.-W. Jung, J. Park, T. Jang, H.-S. Kim, J.-S. Nam, H. Lim, K. R. Yoon, W.-H. Ryu, I.-D. Kim and H. R. Byon, *ACS Nano*, 2020, **14**, 14549–14578.

20 M. Zhao, B. Q. Li, X. Q. Zhang, J. Q. Huang and Q. Zhang, *ACS Cent. Sci.*, 2020, **6**, 1095–1104.

21 R. Deivanayagam, B. J. Ingram and R. Shahbazian-Yassar, *Energy Storage Mater.*, 2019, **21**, 136–153.

22 M. Fichtner, *Magnesium Batteries: Research and Applications*, Royal Society of Chemistry, 2019, vol. 2020.

23 R. Attias, M. Salama, B. Hirsch, Y. Goffer and D. Aurbach, *Joule*, 2019, **3**, 27–52.

24 J. Pandeeswari, G. Jenisha, K. Z. Walle and M. Kotobuki, *Batteries*, 2023, **9**, 570.

25 H. Dou, X. Zhao, Y. Zhang, W. Zhao, Y. Yan, Z.-F. Ma, X. Wang and X. Yang, *Nano Energy*, 2021, **86**, 106087.

26 T. D. Gregory, R. J. Hoffman and R. C. Winterton, *J. Electrochem. Soc.*, 1990, **137**, 775–780.

27 D. Aurbach, M. Moshkovich, A. Schechter and R. Turgeman, *Electrochem. Solid-State Lett.*, 2000, **3**, 31–34.

28 M. Rastgoo-Deylami, M. S. Chae and S.-T. Hong, *Chem Mater*, 2018, 9.

29 Y. Cheng, T. Liu, Y. Shao, M. H. Engelhard, J. Liu and G. Li, *J. Mater. Chem. A*, 2014, **2**, 2473–2477.

30 H. Yang, C. Guo, A. Naveed, J. Lei, J. Yang, Y. Nuli and J. Wang, *Energy Storage Mater.*, 2018, **14**, 199–221.

31 O. Tutusaus and R. Mohtadi, *Chemelectrochem*, 2015, **2**, 51–57.

32 O. Tutusaus, R. Mohtadi, N. Singh, T. S. Arthur and F. Mizuno, *Acs Energy Lett.*, 2017, **2**, 224–229.

33 O. Tutusaus, R. Mohtadi, T. S. Arthur, F. Mizuno, E. G. Nelson and Y. V. Sevryugina, *Angew. Chem. Int. Ed.*, 2015, **54**, 7900–7904.

34 T. Mandai, *ACS Appl. Mater. Interfaces*, 2020, **12**, 39135–39144.

35 J. A. Blázquez, R. R. Maça, O. Leonet, E. Azaceta, A. Mukherjee, Z. Zhao-Karger, Z. Li, A. Kovalevsky, A. Fernández-Barquín, A. R. Mainar, P. Jankowski, L. Rademacher, S. Dey, S. E. Dutton, C. P. Grey, J. Drews, J. Häcker, T. Danner, A. Latz, D. Sotta, M. R. Palacin, J.-F. Martin, J. M. G. Lastra, M. Fichtner, S. Kundu, A. Kraytsberg, Y. Ein-Eli, M. Noked and D. Aurbach, *Energy Environ. Sci.*, 2023, **16**, 1964–1981.

36 S. Chen, S. Fan, H. Li, Y. Shi and H. Y. Yang, *Coord. Chem. Rev.*, 2022, **466**, 214597.

37 L. P. Wang, Z. Zhao-Karger, F. Klein, J. Chable, T. Braun, A. R. Schür, C. R. Wang, Y. G. Guo and M. Fichtner, *ChemSusChem*, 2019, **12**, 2286–2293.

38 K. A. See, K. W. Chapman, L. Zhu, K. M. Wiaderek, O. J. Borkiewicz, C. J. Barile, P. J. Chupas and A. A. Gewirth, *J Am Chem Soc*, 2016, **138**, 328–337.

39 Z. Wang, A. Bandyopadhyay, H. Kumar, M. Li, A. Venkatakrishnan, V. B. Shenoy and E. Detsi, *J. Energy Storage*, 2019, **23**, 195–201.

40 Y. Man, P. Jaumaux, Y. Xu, Y. Fei, X. Mo, G. Wang and X. Zhou, *Sci. Bull.*, 2023, **68**, 1819–1842.

41 S. B. Son, T. Gao, S. P. Harvey, K. X. Steirer, A. Stokes, A. Norman, C. Wang, A. Cresce, K. Xu and C. Ban, *Nat. Chem.*, 2018, **10**, 532–539.

42 Q. Guo, W. Zeng, S. L. Liu, Y. Q. Li, J. Y. Xu, J. X. Wang and Y. Wang, *Rare Met.*, 2021, **40**, 290–308.

43 D. Aurbach, H. Gizbar, A. Schechter, O. Chusid, H. E. Gottlieb, Y. Gofer and I. Goldberg, *J. Electrochem. Soc.*, 2002, **149**, A115.

44 C. Liebenow, Z. Yang and P. Lobitz, *Electrochem. Commun.*, 2000, **2**, 641–645.

45 D. Aurbach, I. Weissman, Y. Gofer and E. Levi, *Chem Rec*, 2003, **3**, 61–73.

46 Y. Viestfrid, M. D. Levi, Y. Gofer and D. Aurbach, *J. Electroanal. Chem.*, 2005, **576**, 183–195.

47 O. Mizrahi, N. Amir, E. Pollak, O. Chusid, V. Marks, H. Gottlieb, L. Larush, E. Zinigrad and D. Aurbach, *J. Electrochem. Soc.*, 2008, **155**, A103.

48 M. Matsui, *J. Power Sources*, 2011, **196**, 7048–7055.

49 R. Mohtadi, M. Matsui, T. S. Arthur and S. J. Hwang, *Angew. Chem. Int. Ed.*, 2012, **51**, 9780–9783.

50 D. Aurbach, B. Markovsky, G. Salitra, E. Markevich, Y. Talyossef, M. Koltypin, L. Nazar, B. Ellis and D. Kovacheva, *J. Power Sources*, 2007, **165**, 491–499.

51 Y. Shao, T. Liu, G. Li, M. Gu, Z. Nie, M. Engelhard, J. Xiao, D. Lv, C. Wang, J. G. Zhang and J. Liu, *Sci. Rep.*, 2013, **3**, 4–10.

52 R. E. Doe, R. Han, J. Hwang, A. J. Gmitter, I. Shterenberg, H. D. Yoo, N. Pour and D. Aurbach, *Chem Commun*, 2014, **50**, 243–245.

53 S. Y. Ha, Y. W. Lee, S. W. Woo, B. Koo, J. S. Kim, J. Cho, K. T. Lee and N. S. Choi, *ACS Appl. Mater. Interfaces*, 2014, **6**, 4063–4073.

54 P. Canepa, S. Jayaraman, L. Cheng, N. N. Rajput, W. D. Richards, G. S. Gautam, L. A. Curtiss, K. A. Persson and G. Ceder, *Energy Env. Sci*, 2015, **8**, 3718–3730.

55 S. J. Kang, H. Kim, S. Hwang, M. Jo, M. Jang, C. Park, S. T. Hong and H. Lee, *ACS Appl. Mater. Interfaces*, 2019, **11**, 517–524.

56 J. Muldoon, C. B. Bucur, A. G. Oliver, J. Zajicek, G. D. Allred and W. C. Boggess, *Energy Env. Sci*, 2013, **6**, 482–487.

57 I. Shterenberg, M. Salama, H. D. Yoo, Y. Gofer, J.-B. Park, Y.-K. Sun and D. Aurbach, *J. Electrochem. Soc.*, 2015, **162**, A7118–A7128.

58 J. G. Connell, B. Genorio, P. P. Lopes, D. Strmcnik, V. R. Stamenkovic and N. M. Markovic, *Chem. Mater.*, 2016, **28**, 8268–8277.

59 C. J. Barile, R. Spatney, K. R. Zavadil and A. A. Gewirth, *J. Phys. Chem. C*, 2014, **118**, 10694–10699.

60 J. Kankare, *Langmuir*, 2002, **18**, 7092–7094.

61 Z. Zhao-Karger, M. E. Gil Bardaji, O. Fuhr and M. Fichtner, *J. Mater. Chem. A*, 2017, **5**, 10815–10820.

62 J. T. Herb, C. A. Nist-Lund and C. B. Arnold, *ACS Energy Lett.*, 2016, **1**, 1227–1232.

63 Z. Hu, L. Huang, X. Gan, Y. Han, J. Chu and Z. Song, *ACS Appl. Mater. Interfaces*, 2024, acsami.4c02399.

64 B. Dlugatch, M. Mohankumar, R. Attias, B. M. Krishna, Y. Elias, Y. Gofer, D. Zitoun and D. Aurbach, *ACS Appl. Mater. Interfaces*, DOI:10.1021/acsami.1c13419.

65 T. Mandai, Y. Youn and Y. Tateyama, *Mater. Adv.*, 2021, **2**, 6283–6296.

66 N. T. Hahn, E. P. Kamphaus, Y. Chen, V. Murugesan, K. T. Mueller, L. Cheng and K. R. Zavadil, *ACS Appl. Energy Mater.*, 2023, **6**, 3264–3277.

67 J. Wang, W. Zhao, H. Dou, B. Wan, Y. Zhang, W. Li, X. Zhao and X. Yang, *ACS Appl. Mater. Interfaces*, 2020, **12**, 19601–19606.

68 Y. Wang, E. Sahadeo and S. B. Lee, *ACS Appl. Energy Mater.*, 2022, **5**, 2613–2620.

69 E. Sahadeo, G. Rubloff, S. B. Lee and C.-F. Lin, *Front. Energy Res.*

70 K. Tang, A. Du, S. Dong, Z. Cui, X. Liu, C. Lu, J. Zhao, X. Zhou and G. Cui, *Adv. Mater.*, 2020, **32**, 1904987.

71 B. Li, R. Masse, C. Liu, Y. Hu, W. Li, G. Zhang and G. Cao, *Energy Storage Mater.*, 2019, **22**, 96–104.

72 R. Lv, X. Guan, J. Zhang, Y. Xia and J. Luo, *Natl. Sci. Rev.*, 2020, **7**, 333–341.

73 C. Wang, Y. Huang, Y. Lu, H. Pan, B. B. Xu, W. Sun, M. Yan and Y. Jiang, *Nano-Micro Lett.*, 2021, **13**, 195.

74 R. Davidson, A. Verma, D. Santos, F. Hao, C. Fincher, S. Xiang, J. Van Buskirk, K. Xie, M. Pharr, P. P. Mukherjee and S. Banerjee, *ACS Energy Lett.*, 2019, **4**, 375–376.

75 Z. Zhang, Z. Cui, L. Qiao, J. Guan, H. Xu, X. Wang, P. Hu, H. Du, S. Li, X. Zhou, S. Dong, Z. Liu, G. Cui and L. Chen, *Adv. Energy Mater.*, 2017, **7**, 1602055.

76 A. Maddegalla, A. Mukherjee, J. A. Blázquez, E. Azaceta, O. Leonet, A. R. Mainar, A. Kovalevsky, D. Sharon, J.-F. Martin, D. Sotta, Y. Ein-Eli, D. Aurbach and M. Noked, *ChemSusChem*, 2021, **14**, 4690–4696.

77 T. Mandai, U. Tanaka and M. Watanabe, *Energy Storage Mater.*, 2024, **67**, 103302.

78 Y. Shao, M. Gu, X. Li, Z. Nie, P. Zuo, G. Li, T. Liu, J. Xiao, Y. Cheng, C. Wang, J. G. Zhang and J. Liu, *Nano Lett.*, 2014, **14**, 255–260.

79 T. S. Arthur, N. Singh and M. Matsui, *Electrochem. Commun.*, 2012, **16**, 103–106.

80 F. Murgia, L. Stievano, L. Monconduit and R. Berthelot, *J. Mater. Chem. A*, 2015, **3**, 16478–16485.

81 Z. Liu, J. Lee, G. Xiang, H. F. Glass, E. N. Keyzer, S. E. Dutton and C. P. Grey, *Chem Commun Camb*, 2017, **53**, 743–746.

82 Z. Meng, Z. Li, L. Wang, T. Diemant, D. Bosubabu, Y. Tang, R. Berthelot, Z. Zhao-Karger and M. Fichtner, *ACS Appl. Mater. Interfaces*, 2021, **13**, 37044–37051.

83 S. J. An, J. Li, C. Daniel, D. Mohanty, S. Nagpure and D. L. Wood, *Carbon*, 2016, **105**, 52–76.

84 E. Peled and S. Menkin, *J. Electrochem. Soc.*, 2017, **164**, A1703–A1719.

85 S. Tan, J. Xu, R. Deng, Q. Zhao, C. Xu, G. Huang, J. Wang and F. Pan, *J. Energy Chem.*, 2024, **94**, 656–676.

86 C. Wei, L. Tan, Y. Zhang, Z. Wang, J. Feng and Y. Qian, *Energy Storage Mater.*, 2022, **52**, 299–319.

87 W. H. Escovitz, T. R. Fox and R. Levi-Setti, *Proc. Natl. Acad. Sci.*, 1975, **72**, 1826–1828.

88 M. f. Hayles and D. a. m. De Winter, *J. Microsc.*, 2021, **281**, 138–156.

89 K. Dimogiannis, A. Sankowski, C. Holc, C. D. J. Parmenter, G. N. Newton, D. A. Walsh, J. O'Shea, A. N. Khlobystov and L. R. Johnson, *Energy Storage Mater.*, 2024, **67**, 103280.

90 Y. Liu, H. King, M. Van Huis, M. Drury and O. Plümper, *Minerals*, 2016, **6**, 104.

91 C. D. Parmenter and Z. A. Nizamudeen, *J. Microsc.*, 2021, **281**, 157–174.

92 M. Asadi, B. Kumar, C. Liu, P. Phillips, P. Yasaei, A. Behranginia, P. Zapol, R. F. Klie, L. A. Curtiss and A. Salehi-Khojin, *ACS Nano*, 2016, **10**, 2167–2175.

93 S. Choudhury, T. Ebert, T. Windberg, A. Seifert, M. Goebel, F. Simon, P. Formanek, M. Stamm, S. Spange and L. Ionov, *Part. Part. Syst. Charact.*, DOI:10.1002/ppsc.201800364.

94 S. Arimoto, D. Oyamatsu, T. Torimoto and S. Kuwabata, *ChemPhysChem*, 2008, **9**, 763–767.

95 E. Strelcov, J. Cothren, D. Leonard, A. Y. Borisevich and A. Kolmakov, *Nanoscale*, 2015, **7**, 3022–3027.

96 C.-Y. Chen, T. Sano, T. Tsuda, K. Ui, Y. Oshima, M. Yamagata, M. Ishikawa, M. Haruta, T. Doi, M. Inaba and S. Kuwabata, *Sci. Rep.*, 2016, **6**, 36153.

97 G. Longoni, M. Fiore, J.-H. Kim, Y. H. Jung, D. K. Kim, C. M. Mari and R. Ruffo, *J. Power Sources*, 2016, **332**, 42–50.

98 J. Wu, M. Fenech, R. F. Webster, R. D. Tilley and N. Sharma, *Sustain. Energy Fuels*, 2019, **3**, 1623–1646.

99 N. Anansuksawat, T. Sangsanit, S. Prempluem, K. Homlamai, W. Tejangkura and M. Sawangphruk, *Chem. Sci.*, 2024, **15**, 2026–2036.

100 H. D. Yoo, S.-D. Han, I. L. Bolotin, G. M. Nolis, R. D. Bayliss, A. K. Burrell, J. T. Vaughey and J. Cabana, *Langmuir*, 2017, **33**, 9398–9406.

101 R. Attias, B. Dlugatch, O. Blumen, K. Shwartsman, M. Salama, N. Shpigel and D. Sharon, *ACS Appl. Mater. Interfaces*, 2022, acsami.2c08008.

102 D. Wang, X. Du, G. Chen, F. Song, J. Du, J. Zhao, Y. Ma, W. Jai, A. Du, Z. Cui, X. Zhou and G. Cui, *Angew. Chem.-Int. Ed.*, 2023, **62**, 1–7.

103 S. DeWitt, N. Hahn, K. Zavadil and K. Thornton, *J. Electrochem. Soc.*, 2015, **163**, A513–A521.

104 C. Wei, L. Tan, Y. Zhang, B. Xi, S. Xiong, J. Feng and Y. Qian, *Energy Storage Mater.*, 2022, **48**, 447–457.

105 Y. Li, X. Zhou, J. Hu, Y. Zheng, M. Huang, K. Guo and C. Li, *Energy Storage Mater.*, 2022, **46**, 1–9.

106 R. Attias, M. Salama, B. Hirsch, R. Pant, Y. Gofer and D. Aurbach, *ACS Energy Lett.*, 2019, **4**, 209–214.

107 M. M. Kabir and D. E. Demirocak, *Int. J. Energy Res.*, 2017, **41**, 1963–1986.

108 K. Wang, P. Yan and M. Sui, *Nano Energy*, 2018, **54**, 148–155.

109 H. C. W. Parks, A. M. Boyce, A. Wade, T. M. M. Heenan, C. Tan, E. Martínez-Pañeda, P. R. Shearing, D. J. L. Brett and R. Jervis, *J. Mater. Chem. A*, 2023, **11**, 21322–21332.

110 A. Wade, A. V. Llewellyn, T. M. M. Heenan, C. Tan, D. J. L. Brett, R. Jervis and P. R. Shearing, *J. Electrochem. Soc.*, 2023, **170**, 070513.

111 R. Ruess, S. Schweidler, H. Hemmelmann, G. Conforto, A. Bielefeld, D. A. Weber, J. Sann, M. T. Elm and J. Janek, *J. Electrochem. Soc.*, 2020, **167**, 100532.

112 M. J. Zachman, Z. Tu, S. Choudhury, L. A. Archer and L. F. Kourkoutis, *Nature*, 2018, **560**, 345–349.

Chapter 2: Experimental

2.1 Electrochemical measurements

Cyclic Voltammetry (CV) is typically used to probe the reversibility of the oxidation and reduction of different species. Typically, a three-electrode set up is used when performing CVs, Figure 2.1a. The three electrodes used are a working electrode (WE), a reference electrode (RE) and a counter electrode. The WE is where the electrochemical reaction of interest occurs by transferring electrons to or from species in solution.[1] WE are typically carbon, platinum or gold, but can also be other materials like copper. The reference electrode is the electrode that the voltage of the WE is measured against. The RE has no current flowing through it, as allowing current to flow through the reference electrode disrupts its stable potential by causing unwanted electrochemical reaction, which alter its redox state and thus its potential. The counter electrode is there to complete the electrical circuit by allowing current to flow through the cell during and electrochemical experiment. The counter electrode also has an equal and opposite current to that of the working electrode to maintain a charge balance in the cell. The counter electrode is also typically larger than the working electrode to ensure that the kinetics of the reactions occurring at the counter electrode don't inhibit the reactions at the WE.[1] During a CV the potential of the working electrode (WE) is changed at a scan rate (mV s^{-1}) and the potential is measured relative to that of a reference electrode (RE) and the current at the working electrode is recorded.[1] A typical electrochemical cell set up for this thesis is shown in Figure 2.1b.

Galvanostatic cycling is another electrochemical technique where an constant current is applied to a cell. This method is commonly used for testing cells to evaluate their performance and efficiency. This is done by applying a constant current to the cell which results charging or discharging of the cell, depending on a positive or negative current respectively. The application of a constant current causes the potential to change during cycling as well as plateauing at certain potentials. These potentials are linked to different electrochemical

processes occurring in the cell. To set the end point of either the charge or discharge a potential limit or a time limit is set, typically both are used in case one is reached first. The cycling done in this thesis was used to measure the plating and stripping overpotentials and the coulombic efficiency of the system over multiple cycles. This technique can either be performed with a three or two electrode cell, in this thesis all galvanostatic cycling is done in a three-electrode cell, with a Mg counter and reference electrode and a Cu working electrode.

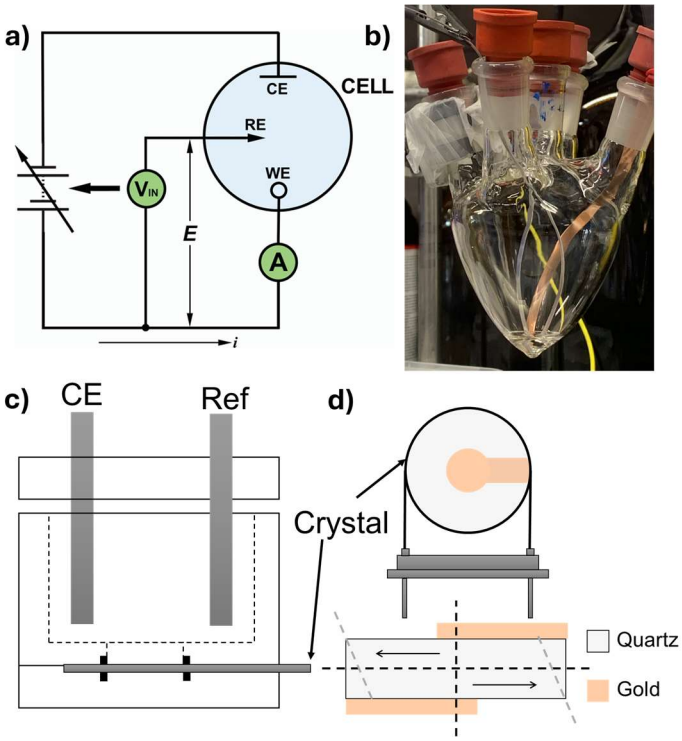

Figure 2.1, (a) schematic illustration of a three-electrode circuit set up (b) photo of the three-electrode glass cell set up used for CVs and galvanostatic measurements, (c) schematic representation of a EQCM cell, (d) a gold disk deposited EQCM crystal and an edge view showing shear deformation. Figure 2.1a was adapted from Colburn et al.[2]

Another technique used to investigate the plating and stripping efficiency of Mg during cycling was EQCM. EQCM uses a metal deposited on a quartz crystal instead of a standard stick electrode or piece of metal ribbon, cell shown in Figure 2.1c. This technique allows for standard electrochemical measurements to be carried out whilst the mass change at the electrode surface is measured,

which is ideal for systems where material is plated and stripped from the electrode surface.[3] EQCM uses the piezoelectric effect. This is where a crystal produces a potential in response to mechanical strain and the converse can also be true, where mechanical strain is induced by a potential. This is done by having an alternating potential across the crystal faces, which causes the crystal to oscillate at a resonate frequency, Figure 2.1d. The deposition of material onto the electrode surface causes a decrease in frequency, a negative change, and stripping causes an increase in frequency, a positive change. This frequency can then be converted to mass through a calibration factor by the Sauerbrey equation, Equation 2.1;

$$\Delta f = \frac{-2f_o^2 m}{A(\mu\rho)^{1/2}} = -C_f m \qquad (2.1)$$

where Δf is the change in frequency, f_o is the resonant frequency of the crystal, m is the mass of the electrode, A is the area of the electrode, μ is the shear modulus of quartz, ρ is the crystal density and C_f is the calibration factor.[4]

2.2 Focused Ion Beam Scanning Electron Microscopy (FIB-SEM) and Energy Dispersive X-ray Spectroscopy (EDX)

In Scanning Electron Microscopy (SEM), electrons are accelerated to high voltages (2 to 30 kV) towards a sample where they interact, producing either secondary electrons or backscattered electrons, which are caused by inelastic and elastic interactions, respectively. Typically, the higher the accelerating voltage used for microscopy, the larger the interaction volume. The interaction volume is how much of the sample the electrons interact with as at higher accelerating voltages the electrons penetrate deeper meaning they have a larger interaction volume. This is useful for techniques such as Energy Dispersive X-ray Spectroscopy (EDX), but for surface details lower voltages are ideal. Secondary electrons are produced when primary electrons from the SEM collide and knock out an electron from an orbital in an atom on the materials surface. These removed electron are then detected by either an Everhart-Thornley or an InLens detector which give topographic and morphological information respectively.[5] Backscattered electrons are produced through elastic scattering of the primary electrons, which undergo deflections (Rutherford scattering) and leave the sample with the same energy they had when interacting with the nuclei of atoms on the surface. This interaction allows for contrast with respect to the Z number of the nuclei.[6] This is due to heavier elements being able to deflect incident electrons more strongly, leading to these areas appearing brighter as more are deflected. During operation the SEM chamber and beam columns are under high vacuum in order to prevent collisions of electrons with gas molecules.

The Focused Ion Beam Scanning Electron Microscope (FIB-SEM) uses an ion beam source to mill samples for cross-sections and depositing material with a gas injector system. FIB columns typically use a liquid metal ion source (LMIS) with gallium being the most common.[7,8] Other FIB sources include gas field emission sources, such as helium and neon, and inductively coupled plasma ion source, like xenon. Gallium sources are commonly used due to its low melting point (29.8 °C), allowing it to be easily liquified and emitted from the LMIS. It is

also easily ionised to generate a stable, high-intensity ion beam. Gallium ions can also be focused into a nanometre-scale beam allowing for accurate cutting and it is also chemically inert with many materials and its ions remain stable under high-vacuum conditions. Along with cutting samples to reveal cross sections, FIB-SEM also allows for 3D reconstruction of materials by producing stacks of images which can be reconstructed into 3D models.

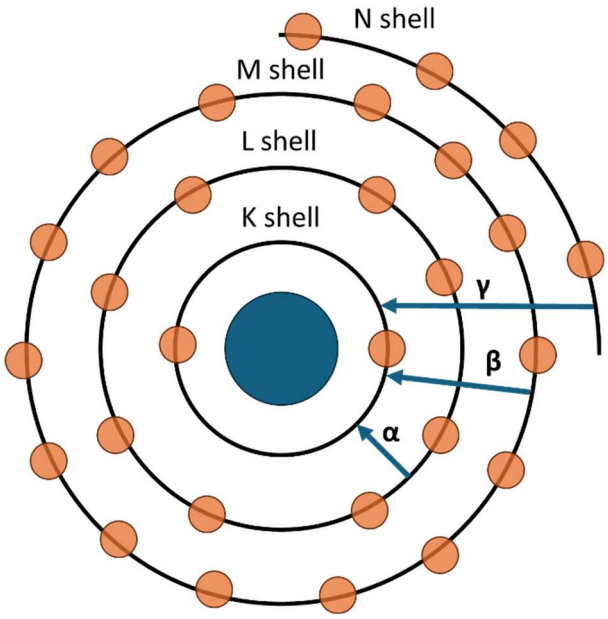

Figure 2.2, The Bohr shell electronic structure and the transitions between shells.

In combination with SEM, EDX is commonly used to provide elemental analysis and mapping of a sample surface. X-rays are produced through the ejection of a secondary electron in a core shell which then leaves an electron hole. This hole is then filled by an electron from a higher energy shell and the energy difference between the shells is emitted as an X-ray. Different elements have different X-ray energies, which depend on the shell it's relaxing to and how many shells it's changing by; X-ray generation shells and transitions are shown in Figure 2.2. For example, a MgKα would mean the electron is relaxing one shell from L to K.

2.3 Transmission Electron Microscopy (TEM) and Electron Energy Loss Spectroscopy (EELS)

Transmission Electron Microscopy (TEM) gives a 2D projection of a 3D structure. TEM is a technique where electrons are accelerated at much higher voltages than SEM (~80 to 200 KV) and cause the electrons to be scattered which causes contrast on the image, with the more scattering areas being darker.[9] Darker areas in bright field TEM images are caused by either, thicker material or higher Z-number. TEM allows for resolution down to sub-angstrom distances and along with seeing d-spacing of crystalline species and the structure at the nanoscale, TEM also allows for electron diffraction patterns to be obtained, these help to identify the crystalline species present.[10] During operation the TEM column is under high vacuum in order to prevent collisions of electrons with gas molecules. With TEM, EDX can also be acquired in-situ for elemental analysis.

Along with acquiring EDX, TEMs can also have detectors for Electron Energy Loss Spectroscopy (EELS). EELS is based on the inelastic scattering of the high accelerating voltage electrons and the sample. When the incident electrons interact with a sample it can cause the electrons within the atoms to shift to higher energy levels or become removed entirely. The scattered electron beam is then analysed spectroscopically to give the energy of the electrons after their interaction with atoms of the sample.[11] EELS can also give information about the valence and oxidation states of the elements present, as different oxidation states will have different binding energies for their valence electrons.

A side affect of using a high energy electron beam is that they can cause beam damage. Beam damage is structural deterioration of the sample due to irradiation of an electron beam. The main damage includes knock-on damage and ionization damage. Knock on damage is caused by the transfer of energy from an electron to an atom in the structure, causing it to be knock out of its lattice position. Elements likely to undergo knock on damage or typically lighter elements such as Li, this is why special conditions such as cryo-TEM and lower accelerating voltages are needed when imaging Li. An example of knock-on damage is shown in Figure 2.3, where after imaging the same sample area for

a while or at higher resolution where the electron beam is more concentrated, the Li sample becomes highly damaged and altered.[12]

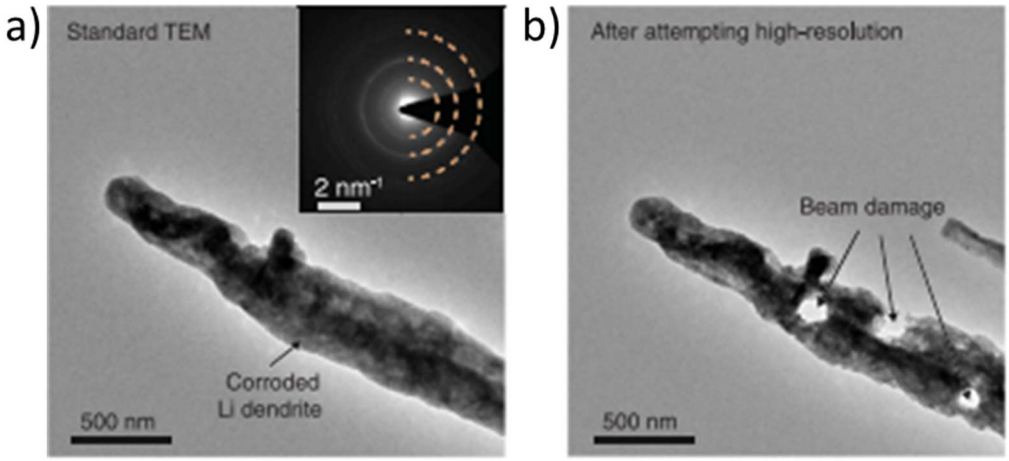

Figure 2.3, a) Standard TEM image of Li dendrite at room temperature and b) TEM image of the damaged Li dendrite after exposure to the electron beam. Adapted from Tao et al.[12]

2.4 X-ray Photoelectron Spectroscopy (XPS)

X-ray Photoelectron Spectroscopy (XPS) is based on the photoelectric effect, where an incident photon of sufficient energy on a material causes the ejection of a photoelectron.[13,14] XPS is a surface-sensitive technique where X-rays are fired at a material, and the kinetic energy of the emitted electrons is measured. The incident X-ray, energy (hν) is equal to the binding energy of the electron (E_B), the kinetic energy of the emitted electron (E_K) and the spectrometer work function ϕ, equation 2.2.[12] The work function is the minimum energy required to remove an electron from the surface of the material. It accounts for the energy loss as the electron escapes the material and enters the vacuum. For the XPS in this thesis the electrons were detected with a hemispherical analyser. A hemispherical analyser measures the kinetic energy of emitted electrons through the application of a electric field. Only electrons with specific energies can pass through along the correct path to the detector, allowing precise energy selection. The electric field is then adjusted to detect a range of different kinetic energy electrons to produce a spectrum.

$$h\nu = E_K + E_B + \phi \quad (2.2)$$

$$E_B = h\nu - E_K - \phi \quad (2.3)$$

Equation 2.2 can be rearranged to give the binding energy of an electron, Equation 2.3 where hν and ϕ are known and E_K is measured. The two main emissions following the bombardment of the sample with X-rays are photoelectrons and auger electrons. Photo electrons are emitted through the emission of an electron from an orbital having been excited by the X-rays, and auger electrons are emitted when an electron from a higher orbital fills the hole of the emitted photoelectron. during this, an electron is emitted, Figure 2.4. The binding energy and Auger electron energies are characteristic of each element and can be used to also determine the oxidation state and bonding state of elements. XPS only give surface information ~1 – 10 nm, which is due to the low escape depth of the elastically scattered electrons.[14] In order to minimise additional peaks on the XPS spectra, like satellite peaks, a

monochromatic X-ray source is used. Satellite peaks typically arise from energy loss processes during the emission of an electron through processes such as, excitation of other electrons.

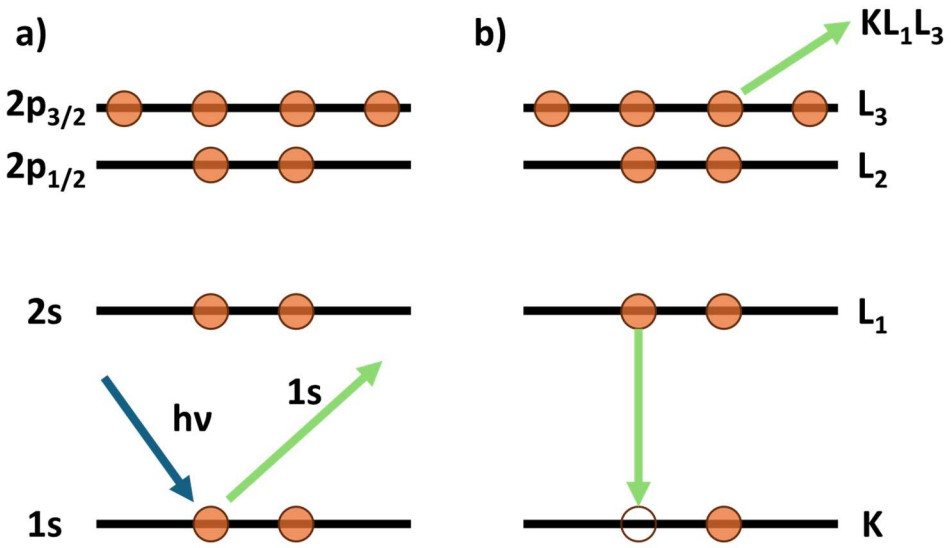

Figure 2.4, emissions that occur following X-ray bombardment (a) photoelectron emission, where the blue arrow is the incident X-ray and the green arrow is the ejection of the core electron and (b) auger electron emission where the green arrow is the relaxation between L_1 and K and the other arrow is the ejection of an auger electron from an outer shell. Adapted from Stevie et al.[14]

2.5 Nuclear Magnetic Resonance (NMR) Spectroscopy

The nucleus consists of both protons and neutrons, which possess a fundamental property called spin. This spin can be described using quantum numbers (I) for the spin and (m) for the spin in a magnetic field. Nuclei with an even number of protons and neutrons have zero spin, and atoms with an odd number of either protons or neutrons has a spin of x/2 (where x is a positive integer which varies between elements) and nuclei with an odd number of protons and neutrons have a spin of a whole number. NMR spectroscopy is based on the relaxation between spin states in a magnetic field. A nucleus with spin I will have 2I+1 possible orientations, which in the presence of no magnetic field are equal.[15] When a magnetic field is applied, the spin states split, with the spin states having the same or opposite direction to the applied field being lower and higher energy, respectively, Figure 2.5. Excitation from the low energy state to the higher energy state is possible with radiofrequency radiation. The nucleus then relaxes down to the lower energy state and emits energy equal to the difference between the spin states. The difference between the two spin states energies depends on the environments and how shielded the nucleus is. Different environments lead to different resonant frequencies; these different environments will give a chemical shift (δ), which allows for the identification of different nuclei.[15]

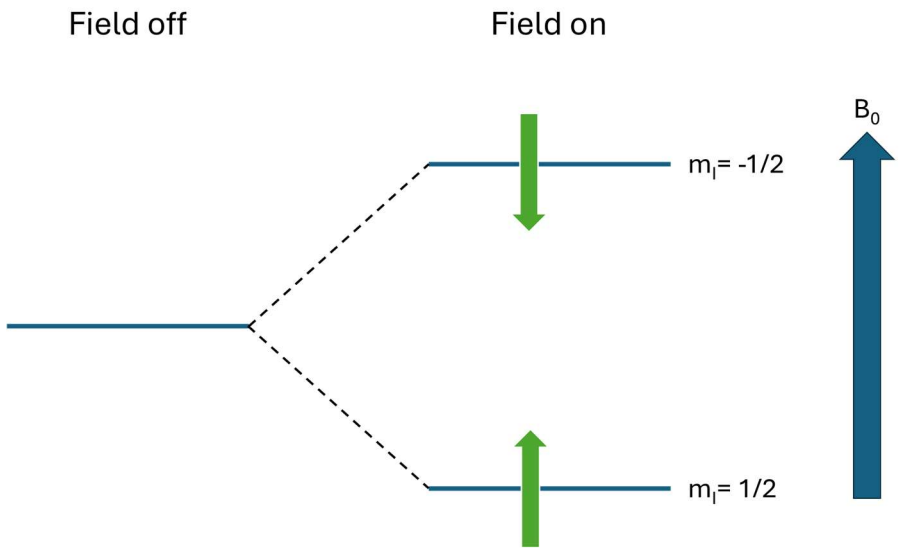

Figure 2.5, Nuclear spin energy levels of a spin ½ nucleus in a magnetic field B_0.

2.6 References

1 N. Elgrishi, K. J. Rountree, B. D. McCarthy, E. S. Rountree, T. T. Eisenhart and J. L. Dempsey, *Journal of Chemical Education*, 2018, **95**, 197–206.

2 A. W. Colburn, K. J. Levey, D. O'Hare and J. V. Macpherson, *Phys. Chem. Chem. Phys.*, 2021, **23**, 8100–8117.

3 M. Biermann, C. Leppin, A. Langhoff, T. Ziemer, C. Rembe and D. Johannsmann, *Analyst*, 2024, **149**, 2138–2146.

4 X. Du, J. Fang and D.-M. Zhu, *Analyst*, 2018, **143**, 3209–3216.

5 B. Griffin, *Scanning*, 2011, **33**, 162–173.

6 L. Reimer and M. Riepenhausen, *Scanning*, 1985, **7**, 221–238.

7 C. A. Volkert and A. M. Minor, *MRS Bulletin*, 2007, **32**, 389–399.

8 L. Almar, J. Joos, A. Weber and E. Ivers-Tiffée, *Journal of Power Sources*, 2019, **427**, 1–14.

9 L. Franken, K. Grunewald, E. Boekema and M. Stuart, *Small*, 2020, **16**, 1906198.

10 D. B. Williams and C. B. Carter, *Transmission electron microscopy: a textbook for materials science*, Springer, New York, 2. ed., 2009.

11 R. Brydson, *Electron Energy Loss Spectroscopy*, 2001.

12 Z. Ju, H. Yuan, T. Liu, J. Nai, Y. Wang, Y. Liu and X. Tao, *Small Science*, **1**, 2100055.

13 D. N. G. Krishna and J. Philip, *Applied Surface Science Advances*, 2022, **12**, 100332.

14 F. A. Stevie and C. L. Donley, *Journal of Vacuum Science & Technology A: Vacuum, Surfaces, and Films*, 2020, **38**, 063204.

15 I. P. Gerothanassis, A. Troganis, V. Exarchou and K. Barbarossou, *Chem. Educ. Res. Pract.*, 2002, **3**, 229–252.

Chapter 3: Correlative FIB-SEM and TEM investigation of the magnesium electrode cycling mechanism

3.1 Background

The poor CE for Mg electrodes is typically ascribed to degradation of the electrolyte, which subsequently reacts with Mg on the electrode surface, forming a passivating layer and reacting with freshly deposited Mg, forming surface structures.[1] Understanding the chemistry and structure of the Mg surface is also important when it comes to compatibility with different electrolyte formulations, as ideally, a uniform layer would be formed on the electrode surface.[2,3] The surface of the Mg electrode and the structures that form during cycling in $Mg(TFSI)_2$-glyme electrolytes have been investigated.[4–6] Although progress has been made in understanding the surface chemistry of the Mg electrode, very little is understood about how these deposits grow over continuous plating and stripping or their internal structures, and these investigations are normally limited to the composition of the deposit or the bulk electrode.[6–11] This understanding is key for understanding the chemical and structural changes which occur during cycling and the stresses it causes on the electrode surface.

When looking at Li metal electrodes, many studies have shown through microscopy how the surface structure volumes change during repeated plating and stripping of Li, which leads to mechanical instability, causing further electrolyte degradation and an accumulation of inactive Li, which in turn leads to an increase in resistance.[12–14] FIB-SEM has been shown to be a promising method for imaging and analysing these surface structures, allowing for cross-sectioning and 3D reconstruction of dendrite structures.[12,15] Without a similar understanding of Mg metal electrodes, the pace of development needed to deliver Mg batteries will be hindered.

In this chapter, a new methodology is developed for analysing the structures that form on the surface of the Mg electrode through a combination of electrochemical, microscopy and spectroscopic techniques. This workflow

allows for the understanding of the 3D structures along with analysis of the structure at both the micro and nanoscale. Whilst developing this methodology, insights will be gained into the surface structures of a simple electrolyte system of $Mg(TFSI)_2$/4G as 4G has a large electrochemical window, good stability with respect to Mg metal and moderately good CE for a system not containing Cl ions. Analysis of the structures formed will also give an insight into the overpotentials observed during cycling and the cause of irreversible capacity fade. By combining the range of different techniques above, a complete understanding of the structural and chemical composition of the electrode surface is uncovered for the first time.

3.2 Results and Discussion

3.2.1 Structural development of the electrode surface through prolonged cycling

Through this chapter and subsequent chapters Mg plating will be defined as charging, as Mg is collected on the surface, and the stripping of Mg will be referred to as discharging. The Mg deposits were formed by cycling a Cu electrode in a 0.5 M $Mg(TFSI)_2$/4G electrolyte for 30 cycles between the potentials of -0.7 and 0.8 V vs Mg^{2+}/Mg. A typical Mg cyclic voltammogram is shown in Figure 3.1a. The CVs start at 0.8 V vs Mg^{2+}/Mg and the potential sweeps negative towards -0.7 V vs Mg^{2+}/Mg, the current starts to go negative at -0.4 V vs Mg^{2+}/Mg and the magnitude of the negative current increases. This negative current is the reduction of Mg^{2+} to Mg metal which is plated on to the electrode surface. Once the CV reaches -0.7 V vs Mg^{2+}/Mg the potential starts to sweep positive, and the current stays negative until the current crosses over at -0.2 V vs Mg^{2+}/Mg. This cross-over is typical of systems involving forming a solid on the electrode surface, and is referred to as a nucleation loop.[16,17] The nucleation loop is caused by differences between the kinetics of nucleation of Mg during plating and the dissolution of Mg during stripping. Then once the current reaches 0.1 V vs Mg^{2+}/Mg a positive current is measured and increases. This positive oxidative current is the oxidation of Mg metal on the surface to Mg^{2+} and this current increases in current density until all available Mg is stripped from the surface, at which point the current drops. As cycling continues the peak heights increase in intensity, for both the oxidation and reduction process of stripping and plating respectively, until it reaches a peak after 5 cycles at which point it stabilises. This is due to a process called conditioning which is due to the purification of the electrolyte and formation of a stable interphase.[18] The onset potential for the plating of Mg onto the electrode surface is stable at -0.36 V vs Mg^{2+}/Mg after the first cycle, and the onset potential for the stripping does decrease from cycle 1 to 3 from 0.13 V to 0.09 V vs Mg^{2+}/Mg but then stays at that potential for the remaining cycles. For these CVs the CE is 62.4 % on average over the 30 cycles which is near the limit

systems can reach when not containing chloride, Figure 3.1b.[19,20] Although after 20 cycles the CE does start to slowly decrease, suggesting that the interphase is not stable enough and starts to react and degrade over time or that it becomes too thick due to continuous electrolyte degredation.[21]

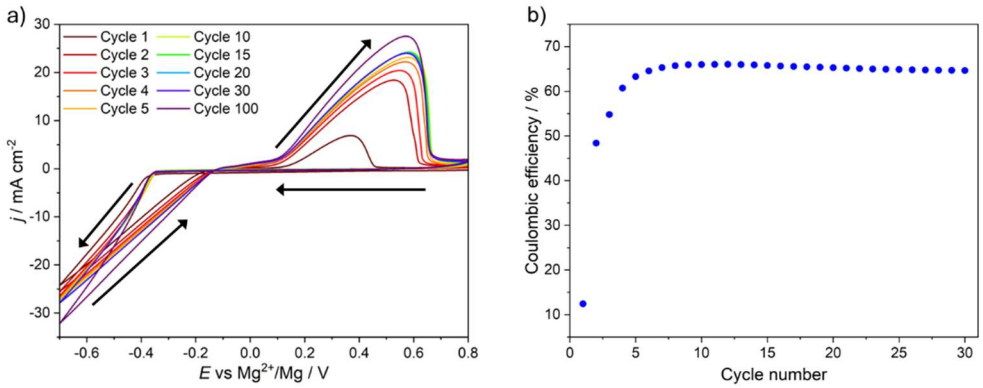

Figure 3.1, (a) Cyclic voltammetry and (b) coulombic efficiency of a 3 mm Cu stick electrode in 0.5 M $Mg(TFSI)_2$/4G for 100 cycles. CV was recorded with a Mg counter and reference electrodes at a scan rate of 100 mV s^{-1}.

After 1, 30 and 100 cycles, the surface of the electrodes was imaged with SEM, ending at 0.8 V vs Mg^{2+}/Mg at discharge, Figure 3.2a-f; all SEM images were acquired using a controlled atmosphere and air-free transfer to avoid exposure to water and air. The SEM images show that hemispherical structures are formed on the electrode surface and show that Mg is not completely stripped during the oxidation process. The size of the deposits increases through progressive cycling from ~ 1.5 µm after 1 cycle to ~ 13 µm after 30 cycles and to ~ 50 µm after 100 cycles. Through progressive cycling and forming these deposits, the peak current density for both the plating and stripping stays consistent, which is intriguing as the surface area of the electrode is increasing as these deposits form, but there isn't a correlative increase in current. The high magnification SEM images of the deposit surface, Figure 3.2b, d and f, show they possess rough surfaces of shard-like crystallite structures about 300 – 800 nm long and 50 to 100 nm wide. In Figure 3.2d, even smaller surface crystallites can be seen on the surface of these plates, and these crystallites are 10 – 20 nm in size. Low magnification images of the electrode surface after cycling

suggest that Mg preferentially deposits along defect sites and scratches from polishing, Figure 3.2g and h.

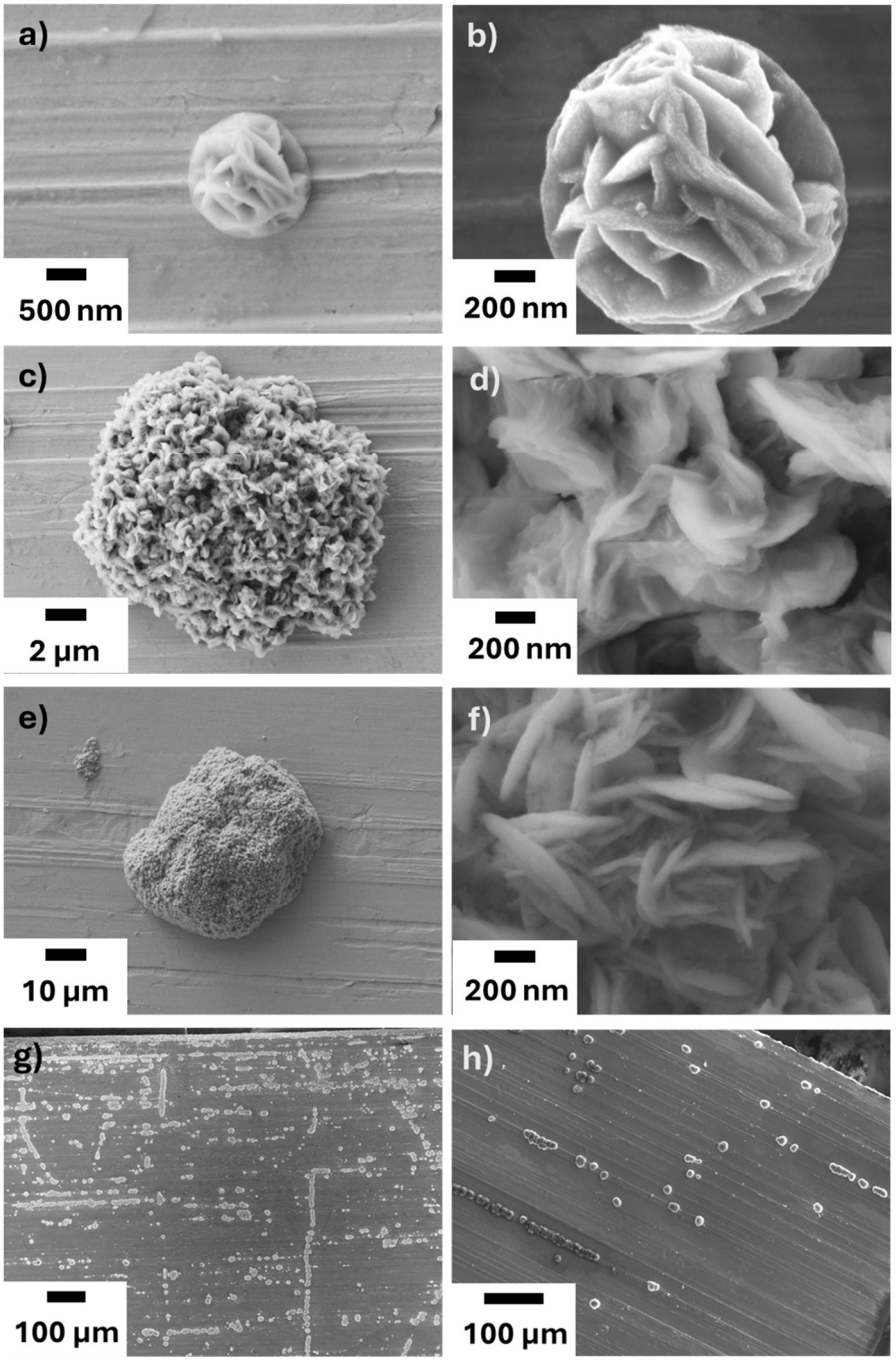

Figure 3.2, SEM images of a cycled Cu electrode after (a-b) 1 cycle, (c-d) 30 cycles and (e-f) 100 cycles (g) and (h) low magnification SEM images of a cycled Cu electrode surface after 30 cycles between -0.7 and 0.8 V vs Mg^{2+}/Mg for 30 cycles, at a scan rate of 100 mV s^{-1} in a 0.5 M $Mg(TFSI)_2$/4G electrolyte

EDX mapping of the surface deposits shows that the Cu electrode surface between deposits is free of Mg and the Mg is concentrated in these deposits, Figure 3.3a-h and Figure 3.3i-o. The deposits have a high amount of Mg, O, F and C concentrated in them in their EDX maps, indicating that they mainly compose of MgO and MgF_2 and likely some C-F_x from electrolyte degradation.[22]

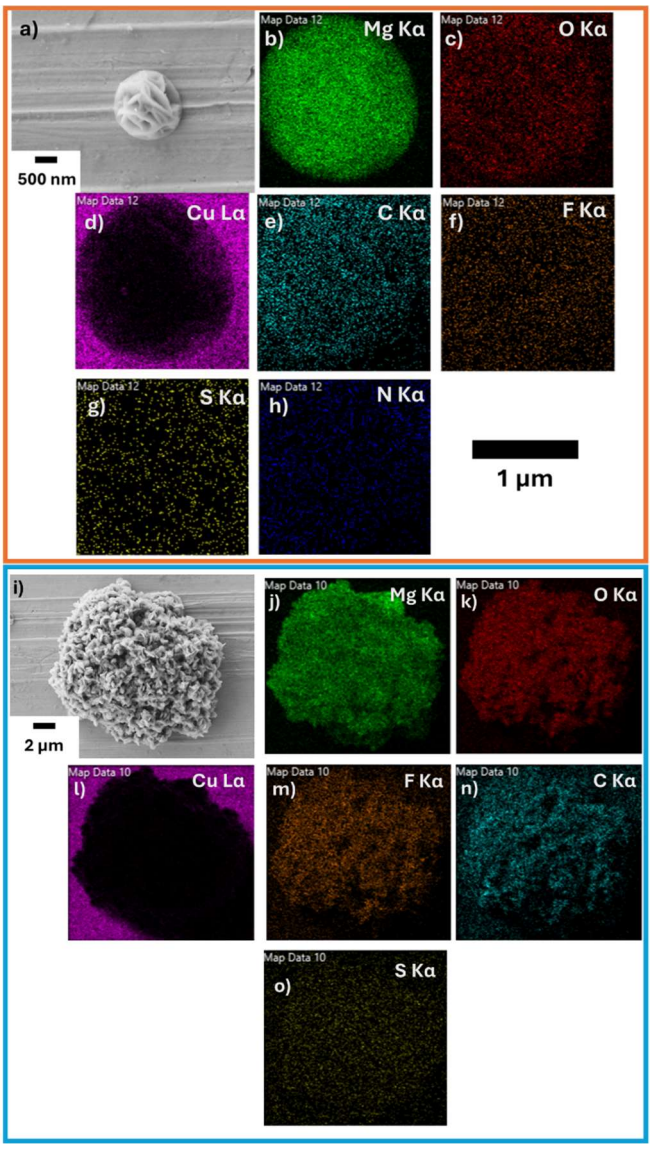

Figure 3.3 (a) SEM of a cycled Cu electrode after 1 cycle between -0.7 and 0.8 V vs Mg^{2+}/Mg, at a scan rate of 100 mV s^{-1} in a 0.5 M $Mg(TFSI)_2$/4G electrolyte (b-H) corresponding EDX maps for (b) Mg, (c) O, (d) Cu, (e) C, (f) F, (g) S and (h) N. The 1 µm scale bar being for the EDX maps. (i) SEM of a cycled Cu electrode after 30 cycles between -0.7 and 0.8 V vs Mg^{2+}/Mg, at a scan rate of 100 mV s^{-1} in a 0.5 M $Mg(TFSI)_2$/4G electrolyte (j-o) corresponding EDX maps for (j) Mg, (k) O, (l) Cu, (m) F,(n) C and (o) S all to the same scale as the SEM image.

3.2.2 Structural analysis of the Mg electrode surface at the micro-scale

In order to fully understand what happens during cycling, the internal structure of these surface deposits might help to explain the electrochemical performance during cycling, specifically, the surface area increasing but there being little change in the electrochemistry. Tilting the sample and milling with the focused ion beam (FIB) will allow for the internal composition of these surface structures to be elucidated, the sample must be tilted so that it is perpendicular to the FIB beam, Figure 3.4a. This tilting also shows more information about the 3D structures which form on the electrode surface. The hemispherical structure has an extremely rough, plate covered surface, Figure 3.4b. The ions used to mill the sample with FIB are gallium ions, these are used due to its low melting point, is easily ionised and can produce a fine, stable beam for high-precision work. It is also inert in nature and can form nanometre-scale beams, making it idea for imaging and sample milling.[23,24]

From the FIB milled cross-section, information is gained about the structure of these deposits from the contrast in the SEM images. These show different areas of contrast, suggesting layers inside the deposit. Going from the core outwards there is lighter contrast to darker, then a lighter ring and back to darker, indicating different chemical composition throughout the structure of these deposits. Analysis of the cross-sectioned deposits shows that they possess an intricate internal structure.

The 3D structure and porosity can be mapped and modelled by performing Serial Slice and Imaging (SSI). SSI is an imaging method where an image is taken, then the sample is milled at a small distance of ~50 nm and then imaged again; this process then repeats through the whole deposit, Figure A1, which allows for 3D mapping of the deposit; Figure 3.4d shows the deposit after the SSI process. Through the Dragonfly software, images were stacked and, with the image dimensions, created voxels (3D pixels), and going through slice by slice, selecting the deposit cross-section from each slice generates the 3D models. The 3D reconstruction was done by manually going through each slice on the dragonfly software and selecting the regions of the deposits which are the

pores and main structures. The 3D reconstruction for the deposit in Figure 3.4b had a porosity of 14 % of the total deposit volume in the discharged state, and these pores permeate through the entire structure, from the surface to the core, 3D models of deposit and pores are shown in Figure 3.4e and f.

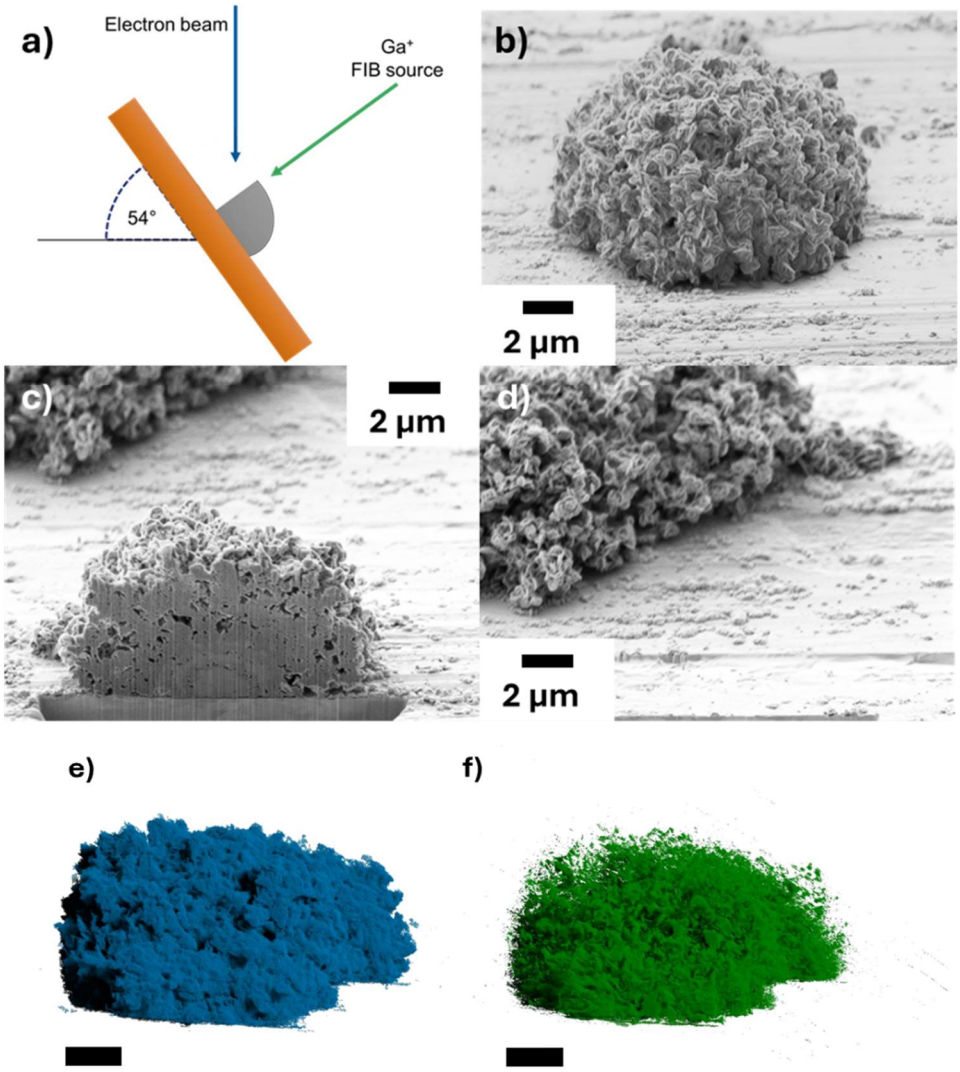

Figure 3.4, (a) schematic representation of the coincidence point between the electron beam and FIB Ga^+ source for milling a deposit (b) SEM image of a Mg deposit imaged at 54 °, (c) cross-sectioned Mg deposit and (d) fully milled deposit from b and c following SSI process. 3D model of (e) the deposit and (f) its internal pore structure, scale bars are 1 µm.

Having the milled cross-section EDX can give insight into the chemical distribution throughout the structure, as shown in Figure 3.5. The EDX map of

the cross-section shows that these deposits possess a complex internal structure. This structure revealed by EDX consists of a core, approximately 2 µm thick, which is rich in Mg metal and depleted of other elements which appear in the EDX. This core can consist of rings of Mg metal and MgO, as shown in the line scan in Figure 3.5g. Going outwards from the core, there is an outer shell; In this area of the deposit, there is more O present and a decrease in Mg intensity, indicating an increase in the amount of MgO present and a decrease in Mg metal. In this region, there is an increase in the intensity of F, which would correspond to the presence of MgF_2. Moving outwards through the inner core, the presence of O increases throughout, and Mg steadily decreases. Then the final part of the structure is the outer core, this area sees an increase in the amount of Mg present and an increase in the amount of C too, the increase in Mg is most likely due to that being the most recently deposited area for Mg leaving some Mg metal potentially trapped in the structure, and the C presence is from the degradation of both the DME and $TFSI^-$.[25] The EDX maps for both N and S, Figure 3.5h and i respectively, show very low counts of each with no correlation with the deposit structure. The low amount measured in the EDX maps is likely due the low atomic ratios of N and S present in the $TFSI^-$ anion compared to other elements such as O and F, the former of which also comes from electrolyte degradation.

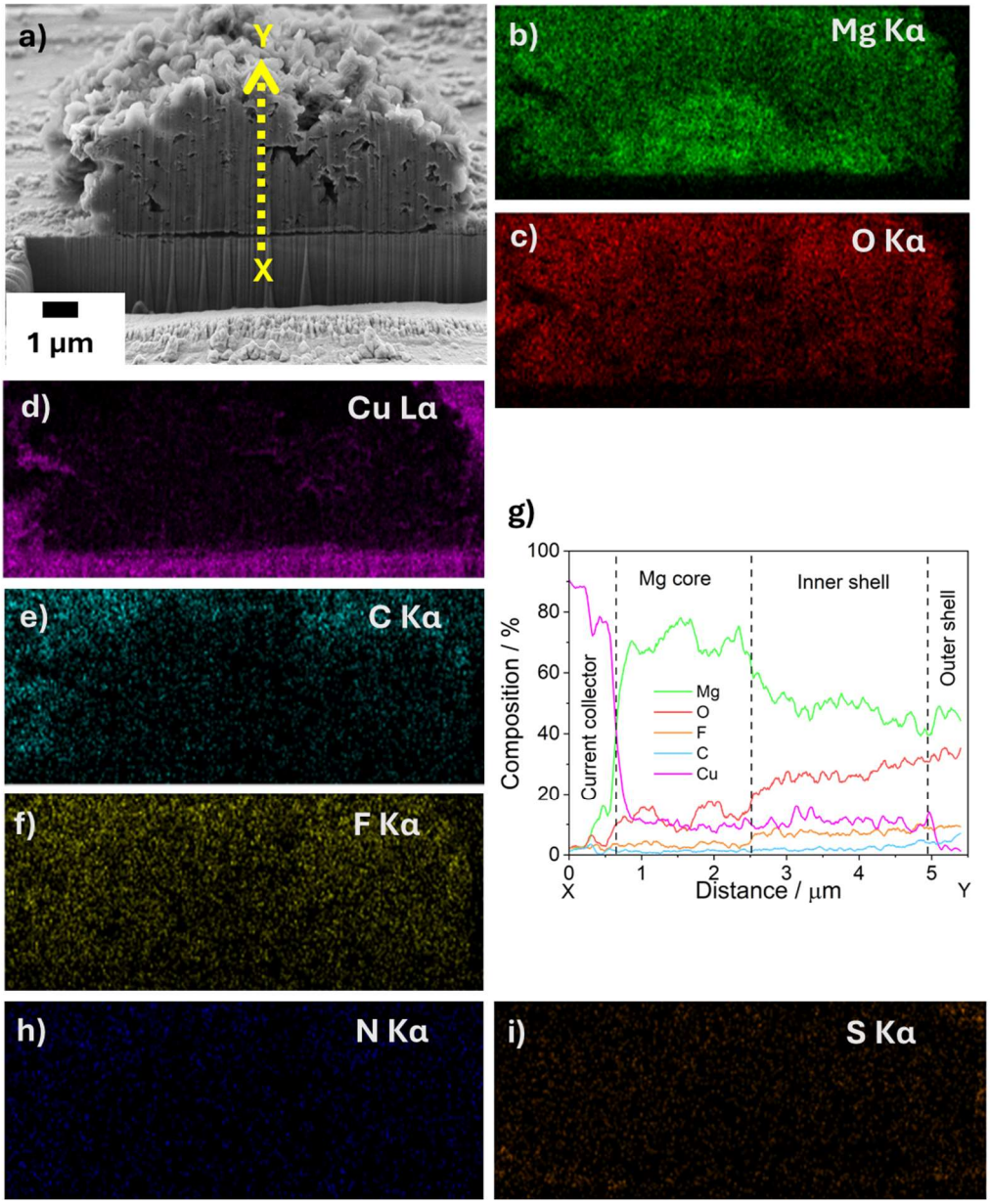

Figure 3.5, (a) SEM image of deposit cross-section formed after 30 cycles (b-f, h and i) EDX maps for Mg, O, C, Cu, F, N and S for the deposit respectively in (a) and (g) line scan from point X to Y in (a). CVs were done between -0.7 and 0.8 V vs Mg^{2+}/Mg with a Cu working electrode and a Mg counter and reference at a scan rate of 100 mV s^{-1} and finished at 0.8 V vs Mg^{2+}/Mg.

3.2.3 Analysis of the Mg electrode surface at charge and discharge

So far, the surface of the electrode and the deposits that form have only been examined in their discharged state, where Mg metal has been stripped from the structure. To better understand how these deposits grow over time, the electrode surface needs to be imaged in the charged state as well.

For the electrode sample to be comparable to those of the discharged samples, the electrodes were cycled 30 times between -0.7 and 0.8 V vs Mg^{2+}/Mg as before but ending at -0.7 V instead of 0.8 V. Figure 3.6 a and b show deposits after 30 cycles but finished in their charged state. Comparing these deposits to those finished at discharge, there are differences. Figure A2 shows the size distributions for charged and discharged deposits after 30 cycles. The mean diameters are 11 µm and 15 µm for the discharged and charged deposits. If you were to take the average radius of both the charged and discharged deposits from above the expected size increase would be ~250 %, on the assumption that they are hemispherical. But 3D models of the average deposit size for both the discharged and charge deposits give a volume increase of 400 %. This discrepancy is seen in the SEM cross-sectional images, Figure 3.4a and Figure 3.6d, where the charged deposits are almost completely hemispherical, whereas the discharged deposits appear to have collapsed, causing the volume increase from discharge to charge to be greater than expected. This is likely because during discharge, Mg has been stripped from the structure, causing it to contract, whereas, for the charged deposits, Mg has been put into the structure, making it expand and fill. Also, looking at the cross-section and 3D models of these charged deposits, Figure 3.6c shows that the internal porosity increases from 62 μm^3 to 456 μm^3 from discharged to charged, respectively, and pore volumes were determined through SSI processing and 3D reconstruction of the deposits.

The line scan through the cross-section, Figure 3.6d, of the deposit, also doesn't show the presence of an internal structure compared to the line scan across the cross-section of the discharged deposit. Although there are two increases in the composition of Mg, there aren't any clear differences in the

EDX maps of the cross-section, Figure 3.6 e-j. The minimal change in the Mg composition through the deposit is because, during charge, Mg will fill the deposit, giving an even distribution throughout. There are no maps of N present due to giving no detectable peak in the EDX spectra.

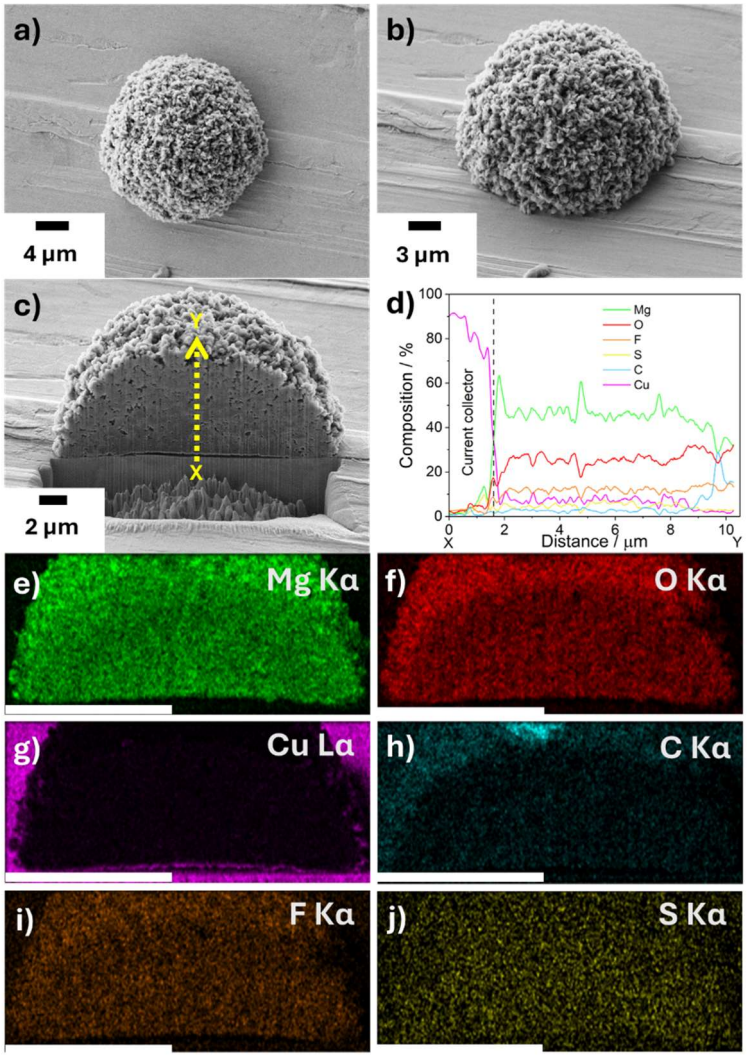

Figure 3.6, (a) SEM images after 30 cycles for a charged deposit (a-b), (c) cross-section of deposit from (a-b). (d) Line scan from point x to y on (c) giving elemental composition between those points. (e-j) EDX maps of Mg, O, Cu, C, F and S of the cross section in (c), the white scale bar being 10 µm. Samples were made through CVs done between -0.7 and 0.8 V vs Mg^{2+}/Mg with a Cu working electrode and a Mg counter and reference at a scan rate of 100 mV s^{-1} and finished at -0.7 V vs Mg^{2+}/Mg.

3.2.4 Magnesium deposit analysis at the nanoscale

So far, this work has just investigated the electrode surface on the microscale. Although this has allowed us to probe the internal chemical structure of the deposits that form, most interphases that form are a couple of hundred nanometres thick, which would be difficult to detect using SEM due to the interaction volume of the incident electron.[25,26] Deposits need to be imaged with TEM to probe the interphase in their pores at the nanoscale.

In order to image these structures at the nanoscale with TEM a lamella needs to be prepared so the sample is thin enough to be analysed. Figure 3.7 shows the whole process of preparing a lamella for TEM from FIB-SEM. An average-sized deposit on the surface is found and focused on at the coincidence point of both the electron and Ga beam so that milling can be monitored in situ (Figure 3.7a).[27] Once the sample has been tilted to be perpendicular to the Ga beam, the gas injector system is inserted, as shown in Figure 3.7b, and then a strip of Pt is deposited over the deposit, Figure 3.7c. This strip of Pt is placed to protect the structure below it from the Ga beam in future thinning. The deposit is then milled on both sides up to the Pt strip, Figure 3.7d, and then undercut and cut down the side to remove it from the substrate with only a small contact point on one side. A micromanipulator is then moved in and attached to the slice through either Pt deposition or redeposition of Cu, if a block of Cu has been attached to the end of the micromanipulator. The slice/lamella is then cut away from the electrode and then moved away, Figure 3.7f, whilst a Cu support grid is transferred into the SEM chamber whilst still remaining air-free. The lamella is attached to the support grid, again with either Pt deposition or Cu redeposition, and the micromanipulator is cut away from the sample, leaving it just attached to the grid, Figure 3.7g. The final stage involves thinning the lamella to approximately 100 nm, Figure 3.7h. The lamella on the support grid was then transferred back to the glovebox before being loaded into an air-free transfer unit for TEM, to avoid contact with the atmosphere.

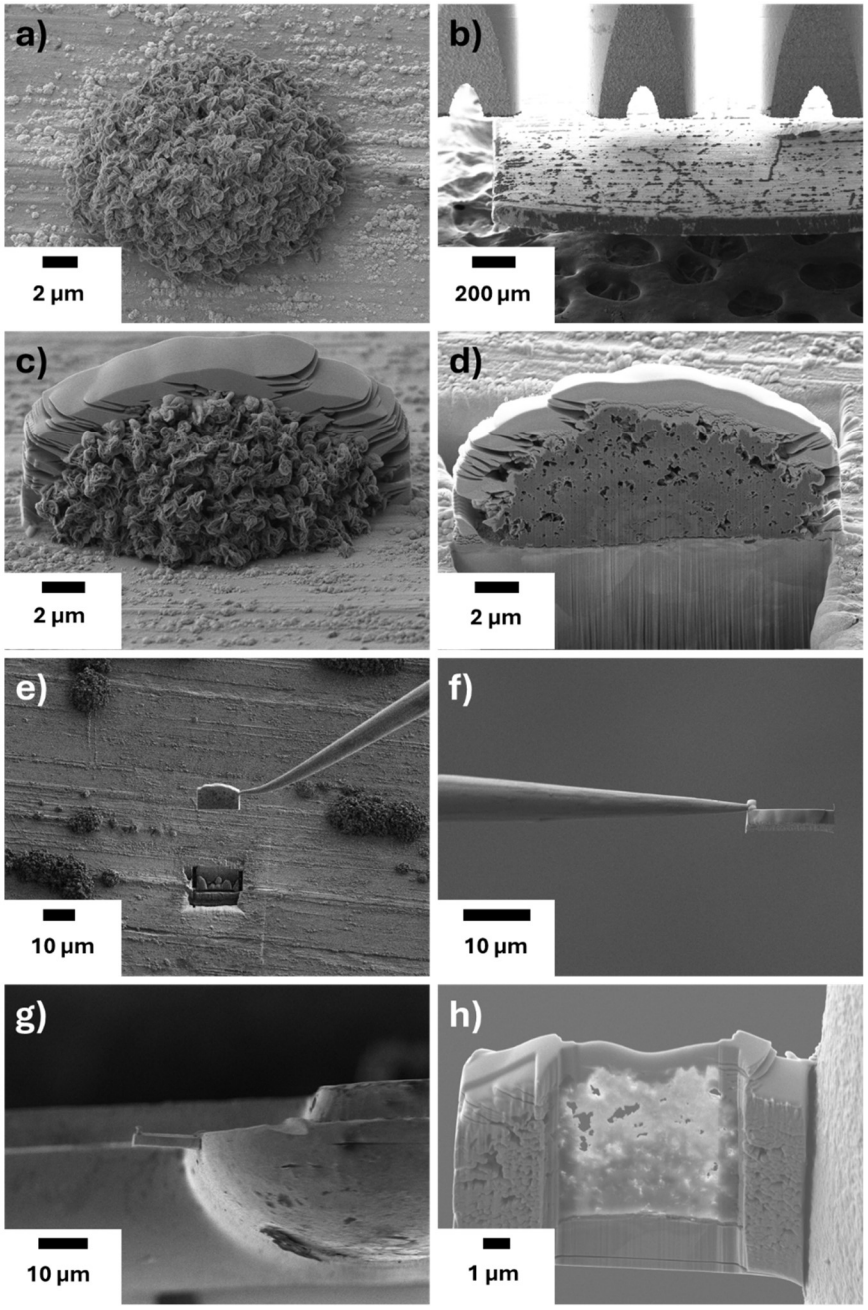

Figure 3.7, (a-h) SEM images of the lift-out process and lamella thinning.

Unfortunately, even though the lamella is thinned enough for TEM, it might not be suitable for TEM through breakage or bending, Figure 3.7a-c. The thinned lamella can bend due to thinning the centre of the slice and leaving a thicker region on either side. The thicker side that isn't attached can cause the lamella to bend, Figure 3.7a and b. Even if the lamella doesn't bend, in some situations, pores can align and cause the lamella to fracture across them, losing most of the sample. These issues have now been mitigated when thinning the

lamella. Only the Mg deposit is thinned, and the Cu substrate is maintained, making a frame structure to support the lamellas integrity, Figure 3.7d, making it more consistent for TEM analysis.

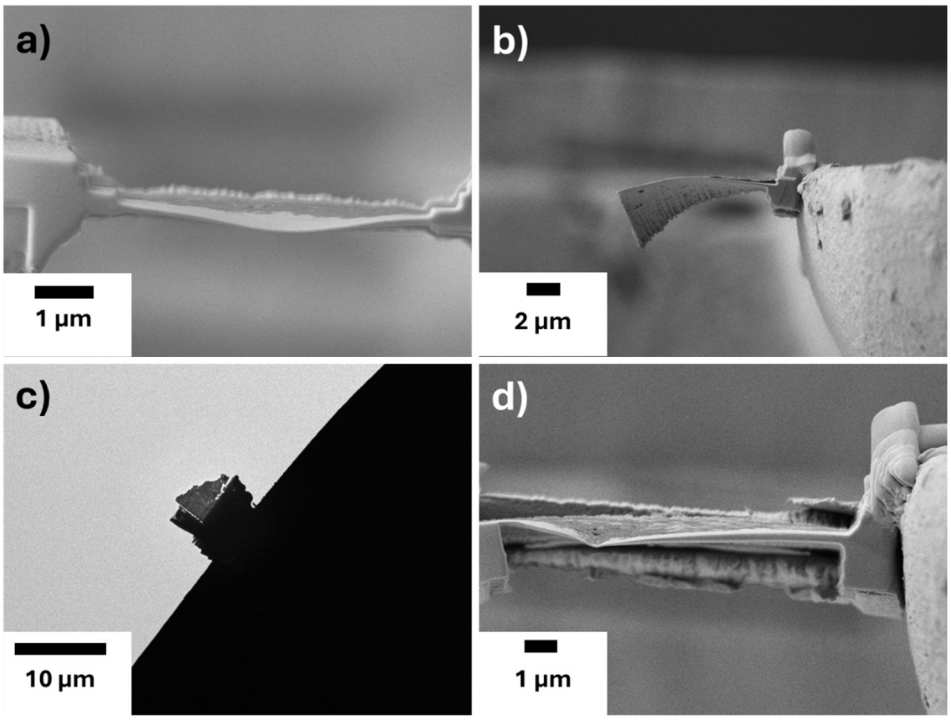

Figure 3.7, (a and b) SEM images of the unsuccessful lamella, (c) TEM image of a lamella that broke, and (d) a successful lamella thinned.

Once the lamellas were successfully thinned, they were transferred to a TEM, again under air-free conditions, to avoid contact with the atmosphere. From the TEM data, it is possible to obtain nanoscale information about the interphase of these deposits and what their structure and composition are.

A benefit of imaging Mg under TEM compared to Li is that for the discharged deposits which mainly consists of MgO no beam damage is observed, even after multiple imaging sessions in the same location. This difference in stability under the electron beam is most likely due to the high ionic bonding strength of MgO, meaning a much higher electron beam energy would be needed to overcome the lattice energy and break the structure.[28]

Increasing magnification with TEM showed the tortuous pore structure throughout the deposits, Figure 3.9a and b. High-magnification images of the

pores remaining in the lamella can also give electron beam diffraction patterns, as shown in Figures 3.9, c and d. These images and corresponding diffraction patterns help to determine if the image area is crystalline. The selected area e-beam diffraction pattern, Figure 3.9d, shows a combination of diffraction spots and concentric rings; both indicate the sample is polycrystalline, meaning there are many small crystals in different orientations, separated by grain boundaries. The rings present in the diffraction pattern correspond to the presence of both MgO and Mg metal, with the most intense rings being from MgO.

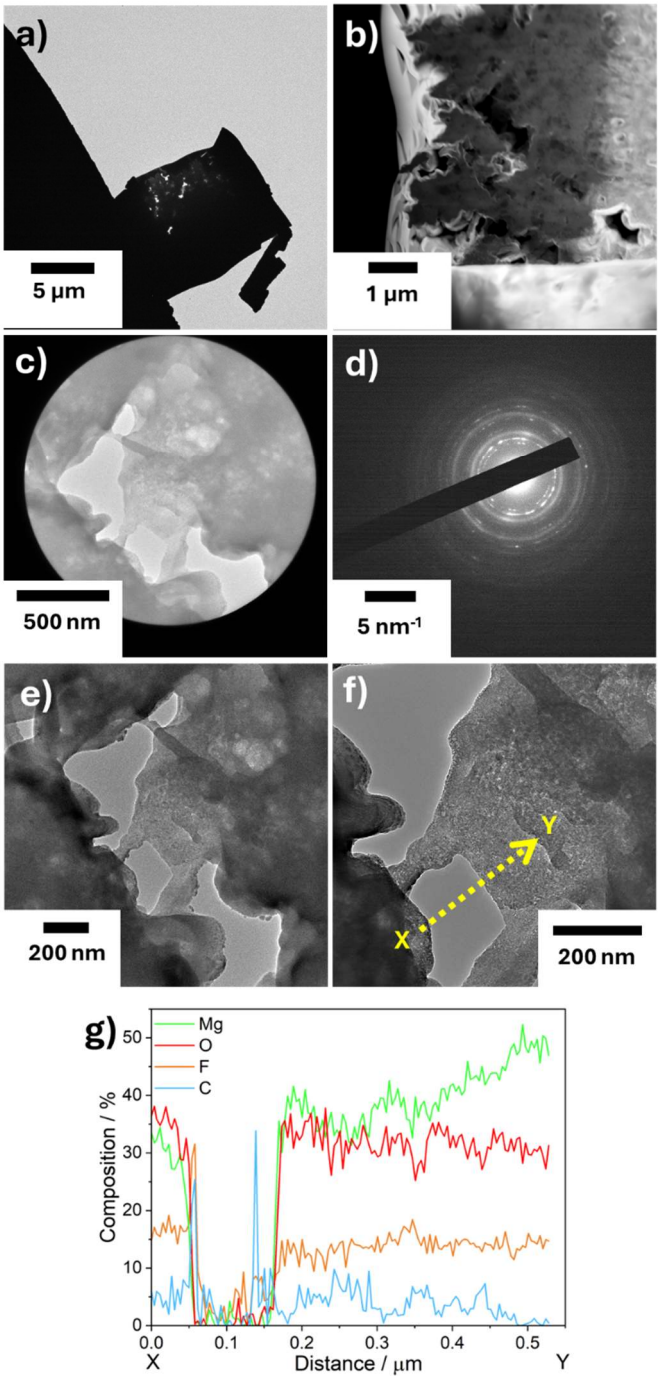

Figure 3.9, (a) Low magnification TEM image of the lamella attached to the support grid, (b) dark-field STEM image of the lamella, and (c) magnified area of the lamella with corresponding electron beam diffraction pattern (d). (e and f) higher magnification images of the lift out and (g) Line scan showing elemental composition from point X to Y in image (f).All a deposit finished cycling at discharge after 30 cycles between -0.7 V and 0.8 V vs Mg^{2+}/Mg with a Cu working electrode and a Mg counter and reference at a scan rate of 100 $mV s^{-1}$.

The area shown in Figure 3.9c and Figure 3.9e is the internal surface of one of the pores which permeate through the deposit. Gaining further elemental analysis of the pore surface and how the chemical composition changes at the nanoscale through that interphase will gain information about the nanoscale interphase, which can't be done with SEM. For this, a line scan was done from point X to Y in Figure 3.9f, covering the surface of the pore as well as some of the bulk structures of the deposit. The line scan, Figure 3.9g, shows the percentage composition of the main elements present in the line scan, those being Mg, O, F and C. At the edge of the pore, where the distance is 0.15 µm the composition is mostly Mg and O, and these are present in similar quantities, meaning that the interphase of the pores is mainly composed of MgO the slight deviation in the amount of Mg and O most likely arises from the presence of MgF_2, which appeared in the electron beam diffraction image, and any electrolyte degradation products consisting of C and O. The presence of F is constant throughout the line scan when over the deposit. A portion of the F signal may be from the presence of MgF_2 if all the Mg is not in the form of MgO, and the F signal could also be from C-F groups which would be from electrolyte degradation of $TFSI^-$.About 200 nm into the pore from the interphase the compositions start to change, from this point there is an increase in the composition of Mg, indicating that Mg is plated from the pore surface and that this deviation is likely trapped Mg metal in the structure, as Mg metal is also seen in the electron beam diffraction pattern, Figure 3.9d

Going to higher magnifications allows for the d-spacing of the nanocrystals to be imaged and measured, Figure 3.10a, and get the corresponding fast fourier transform (FFT). These images show that the structure contains crystals of both MgO and MgF_2. These are shown by the d-spacings of 2.1 to 2.5 Å for MgO and 3.1 Å for MgF_2. The EELS spectra can help to indicate the oxidation states of elements present in the sample, which will help confirm the compositions from the line scans. The C K edge, Figure 3.10b, is consistent with that of amorphous carbon which is likely to have formed from electrolyte degradation during cycling. The F K edge, Figure 3.10c, shows the presence of fluoride in the

sample, consistent with the d-spacing of MgF_2.[29] The Mg K edge, Figure 3.10d, is consistent with that of Mg^{2+} showing the presence of MgO and MgF_2, interestingly the K edge spectra for Mg metal is not reported so the presence of Mg metal can't be confirmed through EELS spectra. Finally, the O K edge, Figure 3.10e, shows the presence of O^{2-} which would be present in MgO.[30]

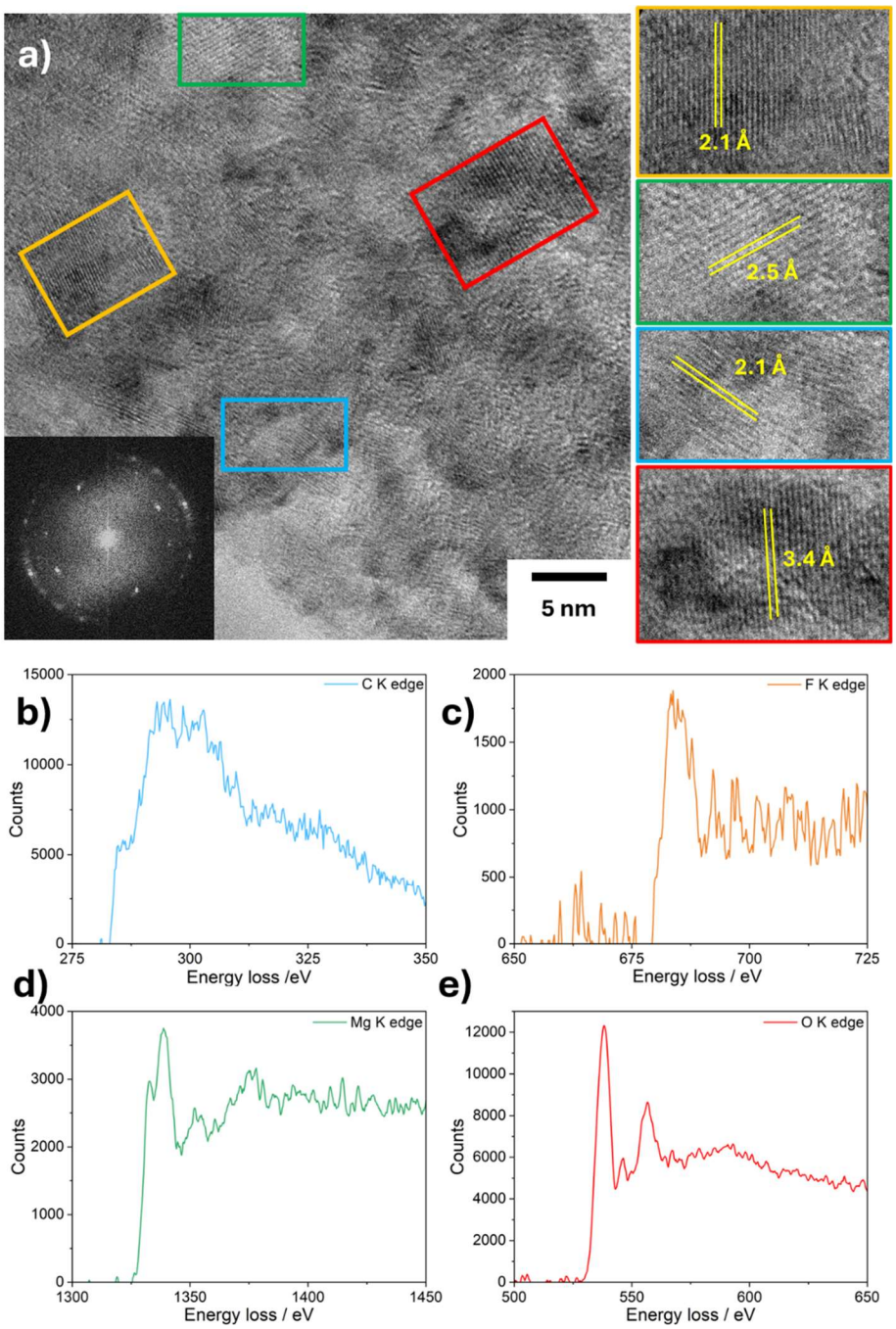

Figure 3.10, (a) high magnification TEM images of a discharged deposit after 30 cycles including d-spacings of areas in boxes including its corresponding FFT, (b)-(e) EELS spectra of C K edge, F K edge, Mg K edge and O K edge.

To further compare the compositional difference between the discharged and charged deposits, a lamella was made for a charged deposit. The lamellas were prepared in the same method as described earlier. Compared to the lift out of the discharged deposit, Figure 3.9 a and b, the charged deposit lamella is much less porous, Figure 3.11a. Along with this the electron beam diffraction pattern, Figure 3.11b and c, for charged deposit has more prominent rings for Mg metal instead of MgO, which were more prominent in that of the discharged deposit. The line scan across the pore of the charged deposit, Figure 3.11d to f, shows a similar relationship between Mg and O to that of the line scan across the discharged deposit pore. This line scan shows a similar composition of Mg and O on the edges of the pore, and this composition, likely from MgO, continues for a couple of hundred nanometres into the deposit. A difference in the line scan is seen in the composition of F and C. Both are present in much higher compositions compared to the discharged deposit. These degradation products would come from the electrolyte reacting with freshly plated Mg, thus causing a higher composition. After measuring the EDX line scan the structure of the sample changed. Where the line scan had been measured the pore had bridged across, Figure 3.11g. This is likely due to Mg metal being a softer material under the electron beam than MgO, much like Li metal is softer than Li_2O under the high accelerating voltage electron beam.[31]

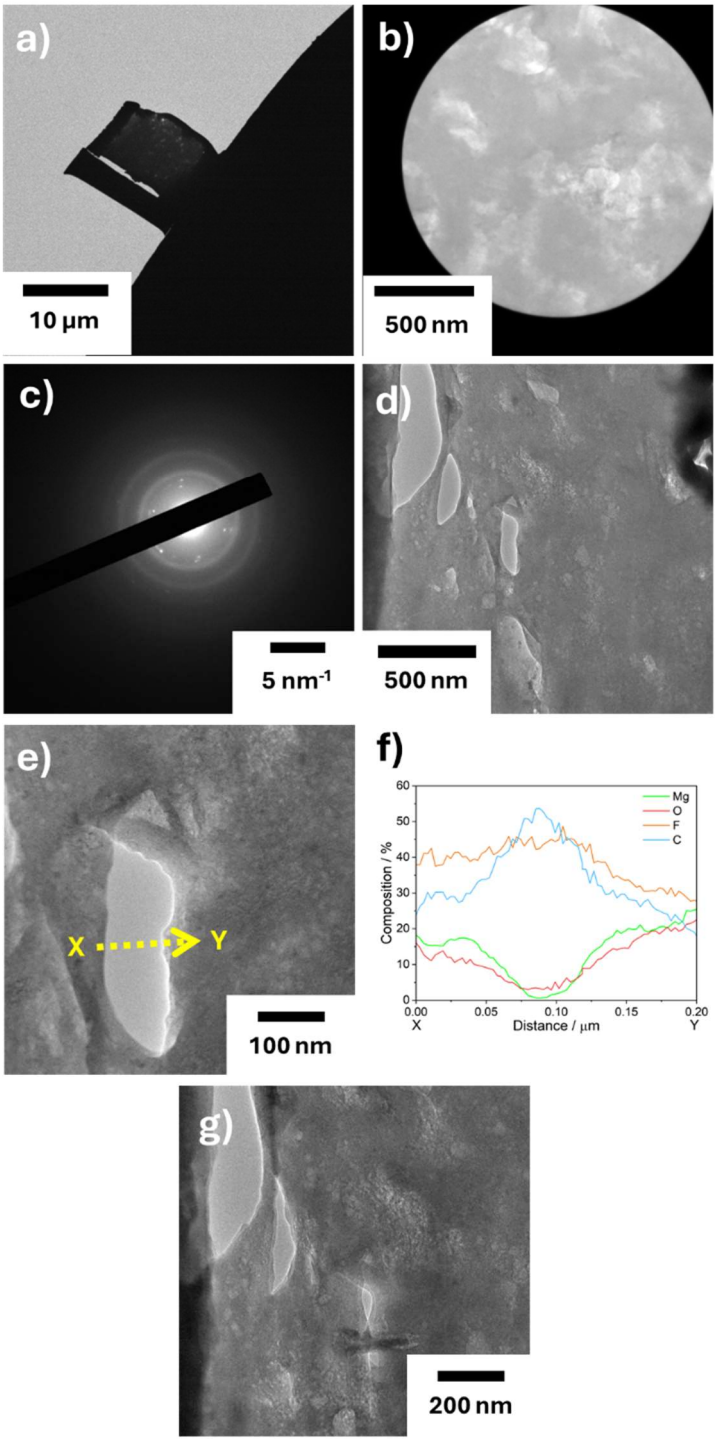

Figure 3.11 (a) Shows a low-magnification TEM image of the lamella attached to the support grid, (b) a magnified area of the lamella with a corresponding electron beam diffraction pattern (c), and (d) and (e) higher-magnification TEM images of the lamella, with X to Y on (e) being the EDX line scan (f) and (g) a TEM image showing the beam damage cause by the line scan acquisition. All deposits have finished cycling at charge after 30 cycles between -0.7 V and 0.8 V vs Mg^{2+}/Mg with a Cu working electrode and a Mg counter and reference at a scan rate of 100 mV s^{-1}.

3.2.5 Mechanism of deposit growth through cycling

The schematic in Scheme 3.1a outlines the main features of the deposits which form during cycling. The previous measurements and images showed that these deposits consist of an inner core which is rich in Mg metal, Mg which is likely too deep within the structure to be stripped out. Moving outwards from this rich Mg core through an intricate network of pores there is an outer core. This outer core is mainly MgO which has formed through degradation of the electrolyte along with some MgF_2 seen in the EELS data. The interphase covering these pores is approximately 100 nm thick and comprises MgO, MgF_2 and organic degradation products. Then the exterior of the deposit structure consists of a MgO, MgF_2 and also organic degradation products. The changes during charge and discharge are shown in Scheme 3.1b. On charging Mg^{2+} ions permeate through the structure using the 3D network of pores and plate Mg onto the inner core and then fill out into the outer core, which deforms the deposit due to the increase in Mg volume, causing it to expand. Then, upon discharge, Mg metal is oxidised to Mg^{2+} and removed from the deposit until all available Mg is removed; this is always less than 100 % than that which is deposited. This then leads to these deposits gradually growing over continued cycling, Scheme 3.1c, as through the deposits imaged at 1, 30 and 100 the size increases throughout indicating the deposits grow through continuous cycling. The reactions in Scheme 3.1d show the likely reactions through which the Mg and organic species form.

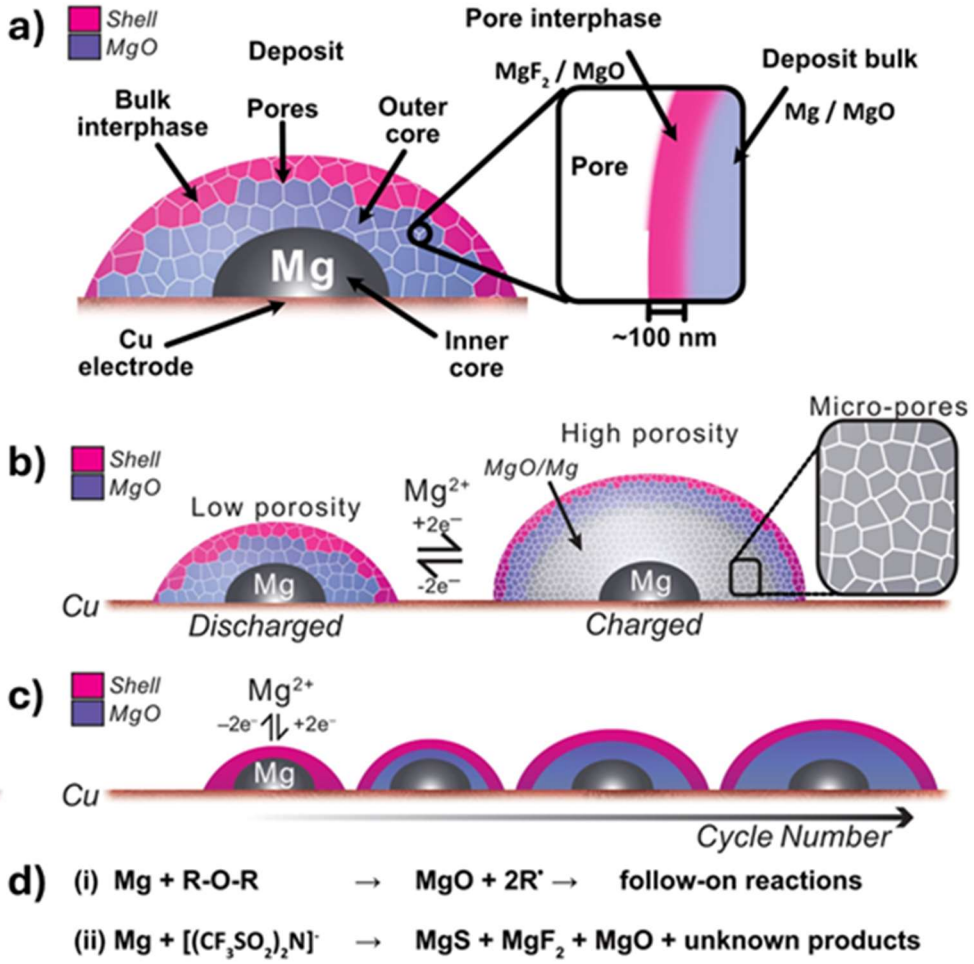

Scheme 3.1, (a) the structure of deposits which form during cycling (b) the transformational changes which occur during charge and discharge, (c) the growth of the deposit over progressive cycles and accumulation of inactive Mg and (d) degradation reactions occurring during cycling of the electrolyte components with Mg.

3.3 Conclusions

Developing a workflow for imaging the electrode surface at both the micro and nanoscale has allowed the structural and chemical changes on the Mg electrode surface to be analysed for the first time. It has been shown that during cycling, hemispherical deposits form on the electrode with a nanocrystalline surface and a deep 3D pore network. The cross-sectioning revealed an intricate layered structure consisting of a Mg metal inner core, MgO, and Mg outer core and an inorganic interphase layer on the surface made up of MgS, MgF_2, and other electrolyte components.

The volumetric analysis of the deposits showed a 400 % increase in volume going from discharge to charge. Volume changes during cycling greatly hinder performance due to further electrolyte degradation and surface passivation, as seen with silicon. Future Mg electrolyte systems must develop strategies to accommodate these fluctuations and avoid the problems they cause.

The lift-out process allowed for the analysis of the interphase at the internal pore walls. This allowed for an even better understanding of the interphase that forms on the wall of the pore, ~100 nm thick and made up of MgO, MgF_2, and other degradation products, before getting to the bulk of the deposit of MgO and Mg.

Although the development of electrolytes which don't form an interphase or these surface structures is ideal to help mitigate the problems they cause, they are unlikely to provide a practical system where impurities and degradation products won't build up and react with Mg electrodes. Thus, future design of electrolytes should focus on the development of artificial interphases, which can reduce electrolyte degradation and still allow for Mg to be reversibly plated and stripped onto the electrode surface. For example, some additives can form an artificial interphase which allows Mg^{2+} to permeate through but not other electrolyte components.[32]

3.4 Experimental

3.4.1 Electrolyte preparation

4G (~300 – 400 mL) (Sigma Aldrich, ≥99 %) was distilled under vacuum over sodium (0.7 g) (Sigma Aldrich, 99 %) and benzophenone (4 g) (Sigma Aldrich, 99 %). The distilled 4G was stored in a N_2 glovebox (MBraun, H_2O <0.1 ppm, O_2 <0.1 ppm) and was dried using 4 Å molecular sieves (Sigma Aldrich) for 3 days. $Mg(TFSI)_2$ (Solvionic, 99.5 %) was dried under vacuum at 120 °C for 3 days and then also stored in an N_2 glovebox. The electrolytes were made by dissolving 0.5 M $Mg(TFSI)_2$ in 4G and leaving it to stir over night until colourless. The water content was then measured using Karl Fischer titration and found to be <15 ppm.

3.4.2 Electrochemical experiments

All electrochemical experiments were performed inside an N_2 glovebox. Prior to use all glassware was cleaned and dried beforehand overnight at 70 °C under vacuum. Cyclic voltammetry measurements were recorded on a Biologic SP-300 potentiostat using three electrodes, a Cu ribbon (Sigma-Aldrich) working electrode and a Mg ribbon (Sigma-Aldrich) counter and reference. The Mg ribbons were scratched beforehand to remove the oxidised layer and reveal the fresh Mg surface. Copper foil was cut into ribbons and dried at 120 °C under vacuum before being stored in the glovebox.

3.4.3 Surface characterisation

Before surface characterisation, the cycled Cu electrodes were washed with DME (Sigma-Aldrich, purity 99.5%) (dried using 4 Å molecular sieves) and allowed to dry under vacuum for 30 minutes in a glovebox mini-antechamber. For transferring samples into the Zeiss Crossbeam 550 FIB-SEM (Carl Zeiss, Germany) the samples were loaded air-free from the glovebox using a Quorum PP3006 CoolLok Transfer port mounted directly onto the glovebox. The sample was transferred to a Quorum PP3010 FIB/SEM Preparation system before being loaded into the SEM chamber. SEM images were taken at an accelerating voltage of 2 kV. A Ga ion FIB source was used for milling the sample at an accelerating voltage of 30 kV with FIB currents between 50 and 700 pA. EDX

analysis was performed with an Oxford Instruments Ultimax 170 X-ray microanalysis detector (Oxford Instruments, UK) and analysed using Aztec software (v 4.3) at an accelerating voltage of 5 kV. The 3D structures, cross sections and deposit volumes were generated using Dragonfly software (v 2021.3 for Windows). Lift-outs of the deposits were prepared for TEM using an in-situ micromanipulator (Omniprobe 200, Oxford Instruments) and transferred to a Cu support grid (EM Resolutions) before final thinning to electron transparency.

TEM, EELS, STEM and electron beam diffraction were performed using a JEOL 2100+ transmission electron microscope at an accelerating voltage of 200 kV. TE samples were loaded in a glovebox and transferred to the TEM using a Gatan HHST4004-010 Environmental cell heating holder. Image analysis and electron diffraction data were analysed using Gatan Digital Micrograph software and CysTBox Server.

3.5 References

1 H. D. Yoo, S.-D. Han, I. L. Bolotin, G. M. Nolis, R. D. Bayliss, A. K. Burrell, J. T. Vaughey and J. Cabana, *Langmuir*, 2017, **33**, 9398–9406.

2 R. Deivanayagam, B. J. Ingram and R. Shahbazian-Yassar, *Energy Storage Materials*, 2019, **21**, 136–153.

3 Z. Wang, A. Bandyopadhyay, H. Kumar, M. Li, A. Venkatakrishnan, V. B. Shenoy and E. Detsi, *Journal of Energy Storage*, 2019, **23**, 195–201.

4 M. S. Ding, T. Diemant, R. J. Behm, S. Passerini and G. A. Giffin, *Journal of The Electrochemical Society*, 2018, **165**, A1983–A1990.

5 N. Sa, N. N. Rajput, H. Wang, B. Key, M. Ferrandon, V. Srinivasan, K. A. Persson, A. K. Burrell and J. T. Vaughey, *RSC Advances*, 2016, **6**, 113663–113670.

6 C. Holc, K. Dimogiannis, E. Hopkinson and L. R. Johnson, *ACS Appl. Mater. Interfaces*, 2021, **13**, 29708–29713.

7 Y.-J. Chang, Y.-S. Huang and P.-W. Chu, *J. Electrochem. Soc.*, 2024, **171**, 020553.

8 B. Dlugatch, J. Drews, R. Attias, B. Gavriel, A. Ambar, T. Danner, A. Latz and D. Aurbach, *J. Electrochem. Soc.*, 2023, **170**, 090542.

9 Z. Hu, L. Huang, X. Gan, Y. Han, J. Chu and Z. Song, *ACS Appl. Mater. Interfaces*, 2024, acsami.4c02399.

10 J. Wang, W. Zhao, H. Dou, B. Wan, Y. Zhang, W. Li, X. Zhao and X. Yang, *ACS Applied Materials and Interfaces*, 2020, **12**, 19601–19606.

11 T. Mandai, Y. Youn and Y. Tateyama, *Mater. Adv.*, 2021, **2**, 6283–6296.

12 M. J. Zachman, Z. Tu, S. Choudhury, L. A. Archer and L. F. Kourkoutis, *Nature*, 2018, **560**, 345–349.

13 B. Thirumalraj, T. T. Hagos, C.-J. Huang, M. A. Teshager, J.-H. Cheng, W.-N. Su and B.-J. Hwang, *J. Am. Chem. Soc.*, 2019, **141**, 18612–18623.

14 Z. Yu, H. Wang, X. Kong, W. Huang, Y. Tsao, D. G. Mackanic, K. Wang, X. Wang, W. Huang, S. Choudhury, Y. Zheng, C. V. Amanchukwu, S. T. Hung, Y. Ma and E. G. Lomeli, *Nature Energy*, DOI:10.1038/s41560-020-0634-5.

15 C. Fang, J. Li, M. Zhang, Y. Zhang, F. Yang, J. Z. Lee, M.-H. Lee, J. Alvarado, M. A. Schroeder, Y. Yang, B. Lu, N. Williams, M. Ceja, L. Yang, M. Cai, J. Gu, K. Xu, X. Wang and Y. S. Meng, *Nature*, 2019, **572**, 511–515.

16 A. Mallik and B. C. Ray, *International Journal of Electrochemistry*, 2011, **2011**, 1–16.

17 P. Geysens, J. Fransaer and K. Binnemans, *RSC Adv.*, 2020, **10**, 42021–42029.

18 S. J. Kang, H. Kim, S. Hwang, M. Jo, M. Jang, C. Park, S. T. Hong and H. Lee, *ACS Applied Materials and Interfaces*, 2019, **11**, 517–524.

19 S. Y. Ha, Y. W. Lee, S. W. Woo, B. Koo, J. S. Kim, J. Cho, K. T. Lee and N. S. Choi, *ACS Applied Materials and Interfaces*, 2014, **6**, 4063–4073.

20 R. E. Doe, R. Han, J. Hwang, A. J. Gmitter, I. Shterenberg, H. D. Yoo, N. Pour and D. Aurbach, *Chem. Commun*, 2014, **50**, 243.

21 K. Dimogiannis, A. Sankowski, C. Holc, C. D. J. Parmenter, G. N. Newton, D. A. Walsh, J. O'Shea, A. N. Khlobystov and L. R. Johnson, *Energy Storage Materials*, 2024, **67**, 103280.

22 M. R. Palacin, P. Johansson, R. Dominko, B. Dlugatch, D. Aurbach, Z. Li, M. Fichtner, O. Luanin, J. Bitenc, Z. Wei, C. Glaser, J. Janek, A. Fernández-Barqun, A. R. Mainar, O. Leonet, I. Urdampilleta, J. A. Blázquez, D. S. Tchitchekova, A. Ponrouch, P. Canepa and G. S. Gautam, *J. Phys. Energy*, 2024, **6**, 031501.

23 M. f. Hayles and D. a. m. De Winter, *Journal of Microscopy*, 2021, **281**, 138–156.

24 C. D. Parmenter and Z. A. Nizamudeen, *Journal of Microscopy*, 2021, **281**, 157–174.

25 Y. Sun, F. Ai and Y. Lu, *Small*, 2022, 2200009.

26 R. Bernstein, Y. Kaufman and V. Freger, in *Encyclopedia of Membrane Science and Technology*, Wiley, 1st edn., 2013, pp. 1–41.

27 S. Bals, L. M. Liz-Marzán, W. J. Parak, K. A. Willets and H. L. Xin, *ACS Nano*, 2024, **18**, 13453–13457.

28 H.-R. Zhang, R. Egerton and M. Malac, *Nuclear Instruments and Methods in Physics Research Section B: Beam Interactions with Materials and Atoms*, 2013, **316**, 137–143.

29 L.-P. Zenser, R. Gruehn and B. H. Liebscher, *Journal of Solid State Chemistry*, 2001, **157**, 30–39.

30 F. Frati, M. O. J. Y. Hunault and F. M. F. de Groot, *Chem. Rev.*, 2020, **120**, 4056–4110.

31 W. Huang, H. Wang, D. T. Boyle, Y. Li and Y. Cui, *ACS Energy Lett.*, 2020, **5**, 1128–1135.

32 Y. Zhang, J. Li, W. Zhao, H. Dou, X. Zhao, Y. Liu, B. Zhang and X. Yang, *ADVANCED MATERIALS*, 2022, **34**, e2108114.

Chapter 4: Additive screening for magnesium ion batteries

4.1 Background

Magnesium ion battery research is a rapidly advancing field as groups look for an alternative for LIBs.[1,2] There is a lack of standardisation in the literature when comparing different electrolytes for a magnesium battery system.[3,4] In recent years, standard protocols have started to be published for lithium-ion research to help make systems easier to compare.[4] Some journals have also developed checklists for standardising the reporting of battery data.[5,6] For Mg battery research, there has been an initial use of standardised methods for analysing systems, such as using certain cycling conditions to investigate the coulombic efficiency of Mg on the negative electrode.[7] But there are still areas where this standardisation of methods can be expanded to develop a more complete understanding and comparison between electrolytes.

EQCM is a technique that has been underutilised in the analysis of the Mg negative electrode.[8,9] For Mg batteries, where the reversible plating and stripping of Mg is key, EQCM has been shown to be an ideal technique for investigating the efficiency of plating and stripping for different electrolyte systems. EQCM has been used in several instances since magnesium battery development in 2000.[10–15] EQCM in Mg battery research has previously been used to determine the relative mass per electron to investigate processes that occur during cycling, the ideal value being 12 (the equivalent Mg mass).[15] The values reported were lower than this showing that the system of Mg cycling on the negative electrode is a complex process, which requires more complimentary techniques to develop a full understanding.

Certain electrolyte systems, such as chloride, borate, and aluminate salts, have improved efficiency and stability during cycling throughout magnesium battery research.[16–18] More recent research has investigated the feasibility of artificial SEIs to help prevent degradation and promote reversible plating and stripping of Mg.[19–22] These artificial layers are either made before or during cycling. The layers made before cycling are typically formed chemicals reacting or adhering

to the electrode surface through a pretreatment methods and those formed in situ are formed by a reaction, either chemical or electrochemical, between the additive and electrode forming a stable artificial interphase.[22–24] Over the years, these electrolyte systems have been studied, but no direct comparison has been made using the same experimental conditions.

In this chapter, different electrochemical techniques are used to directly compare a few different electrolyte systems containing some of the aforementioned electrolyte components. Along with comparing the different electrolyte systems electrochemically, the changes on the electrode surface were analysed with EQCM and SEM. This allowed for a thorough investigation of how the surface structures of different systems vary under the same conditions and show how the electrochemical and SEM data correlate to their performance.

4.2 Results and Discussion

4.2.1 Salt synthesis

To compare the current leading electrolytes reported in the literature, $Mg[B(hfip)_4]_2$ and $Mg[Al(hfip)_4]_2$ had to be synthesised using a combination of methods from the literature.[17,25,26] Due to costs and the current global high demand of $Mg[BH_4]_2$, which is affecting supply chains, $MgCl_2$ was used as the starting material for the synthesis of $Mg[B(hfip)_4]_2$. The first step, Scheme 4.1a, involves a salt metathesis between $NaBH_4$ and $MgCl_2$ in a ball mill, followed by a solvent extraction in diethyl ether. The resulting powder was analysed with NMR and EDX to check the purity of the sample.

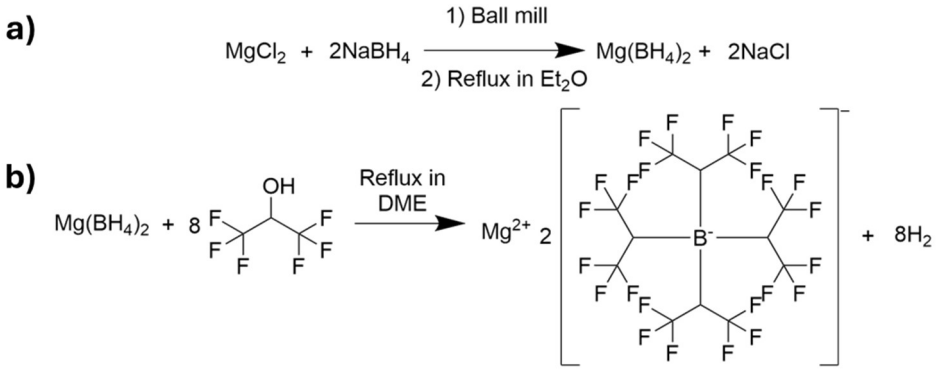

Scheme 4.1, synthesis method for (a) $Mg(BH_4)_2$ and (b) $Mg[B(hfip)_4]_2$.

The EDX spectra, Figure A3, showed that very small amounts of NaCl were present in the resulting powder, with an atomic percentage of approximately 2 %, and the high presence of oxygen in the spectra was due to handling in air before loading into the SEM. The broad multiplet between 0.15 and -0.77 ppm in Figure 4.1a corresponds to the protons of the borohydride anion. Boron has two NMR active isotopes: ^{10}B with a nuclear spin of 3 and an abundance of 19.9 % and ^{11}B with a nuclear spin of 3/2 and an abundance of 80.1 %.[27] The four peaks of higher intensity are due to coupling with the ^{11}B and attached hydrogens. The smaller peaks, which form shoulders on these peaks, are from the hydrogen coupling with ^{10}B. The ^{11}B NMR spectra showed a quintet from coupling with the four bonding hydrogen atoms.

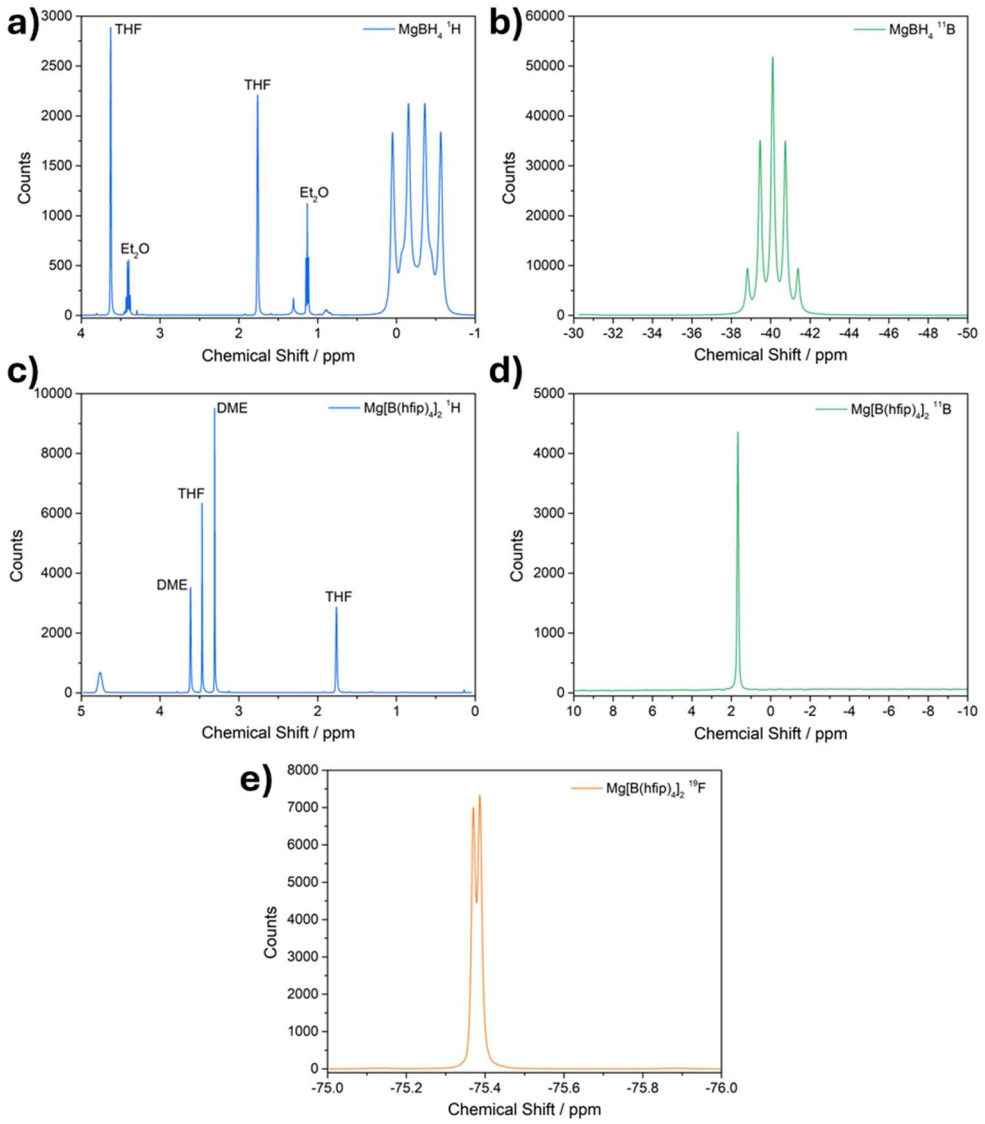

Figure 4.1, (a) ^{1}H NMR spectrum of $Mg(BH_4)_2$, (b) ^{11}B NMR spectrum of $Mg(BH_4)_2$, (c) ^{1}H NMR spectrum of $Mg[B(hfip)_4]_2$, (d) ^{11}B NMR spectrum of $Mg[B(hfip)_4]_2$ and ^{19}F NMR spectrum of $Mg[B(hfip)_4]_2$.

For the synthesis of $Mg[B(hfip)_4]_2$, HFIP was added to the previously synthesised $Mg(BH_4)_2$. For this, $Mg(BH_4)_2$ was dissolved in DME, and HFIP was then slowly added. The addition of HFIP causes the temperature of the reaction vessel to increase and for gas to be produced; this is due to the evolution of hydrogen gas from the reaction between the borohydride and the HFIP. Once added and the solvent removed, a white powder is left, which, when looking at the NMR spectra, is pure, with no remaining starting materials present, Figure 4.1 c-e and Figures A4a and b. The proton NMR spectra for $Mg[B(hfip)_4]_2$ show

a high presence of DME; this is due to the strong coordinating nature of DME to Mg as it acts like a bidentate ligand, meaning for each Mg atom, there are three DME molecules.[28] The broad peak at 4.76 ppm relates to the proton on the central carbon on the HFIP group bonded to the boron. The high ppm of this peak is due to the fluorine atoms on the adjacent carbon atom.

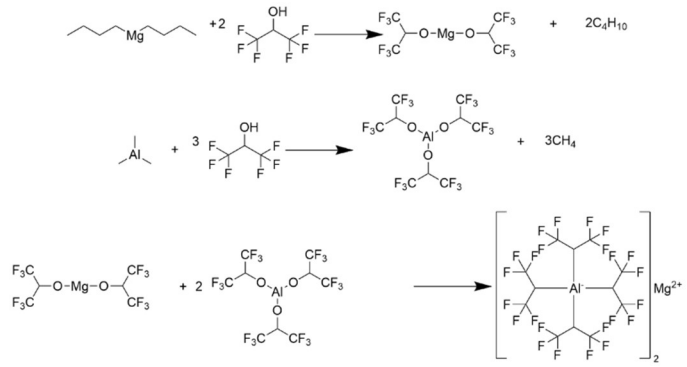

Scheme 4.2, synthesis method for $Mg[Al(hfip)_4]_2$.

Two literature methods were used to synthesize Mg[Al(hfip)4] from dibutyl magnesium and trimethyl aluminium.[29,30] These methods are one-pot reactions, and by adding HFIP to dibutyl magnesium and the tri methyl aluminium $Mg[Al(hfip)_4]_2$ is formed, Scheme 4.2. The NMR spectra for $Mg[Al(hfip)_4]_2$ were taken to check the purity, Figure 4.2. The proton NMR matches those reported in the literature; DME peaks present due to the strong coordination of DME to Mg and a multiplet at 4.62 ppm corresponding to the proton present on the central carbon of the hip. The ^{19}F does have an extra peak present at -76.3 ppm, which, even after repeating the synthesis, is still present, and it doesn't correspond to the ^{19}F peak of HFIP in its NMR spectrum, Figure A9d.

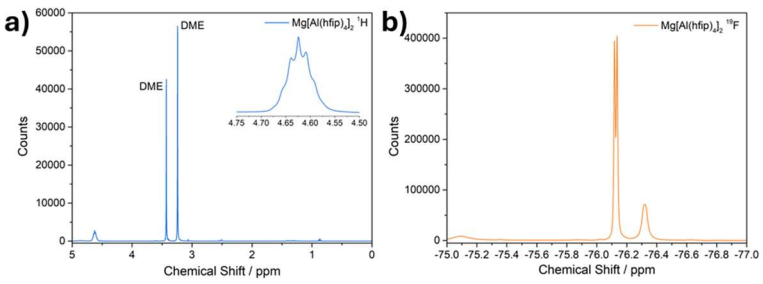

Figure 4.2, (a) (a) ^1H NMR spectrum of $Mg[Al(hfip)_4]_2$ and (b) ^{19}F NMR spectrum of $Mg[Al(hfip)_4]_2$.

4.2.2 Voltammetry of different electrolyte systems

To develop a workflow to test and compare different electrolytes, listed below, for Mg batteries, a range of different glyme-based electrolytes from literature were tested.

- 0.5 M $Mg(TFSI)_2$ in 2G ($MgTFSI_2$/2G)
- 0.5 M $Mg(TFSI)_2$ and 10 mM $Pry_{14}TFSI$ in 2G ($MgTFSI_2$+$Pry_{14}TFSI$/2G)
- 0.25 M $Mg(TFSI)_2$ and 0.125 M $MgCl_2$ in 2G ($MgTFSI_2$+$MgCl_2$/2G)
- 0.125 M $Mg(TFSI)_2$ and 0.25 M $MgCl_2$ in 1G ($MgTFSI_2$+$MgCl_2$/1G)
- 0.3 M $Mg[B(hfip)_4]_2$ in 1G ($Mg[B(hfip)_4]_2$/1G)
- 0.4 M $Mg[Al(hfip)_4]_2$ in 2G ($Mg[Al(hfip)_4]_2$/2G)

Some of the electrolyte systems from the literature were altered, changing the glyme solvent due to poor electrochemical performance, Figure A5. In literature 0.5 M $Mg(TFSI)_2$ is typically dissolved in 1G, but the cycling, Figure A5a, shows that large overpotentials are needed to both plate and strip Mg as well as having poor coulombic efficiency.[15] Also the 0.5 M $Mg(TFSI)_2$ and 10 mM $Pry_{14}TFSI$ electrolytes in literature are used in 1G electrolyte, but when tested Mg plating does not occur within the experimental parameters, Figure A5b.[19] However, both of these electrolyte systems work with 2G instead of 1G, and thus were used with 2G.

For testing all of the electrolytes above, a Cu WE was used to treat the electrochemistry as an anode-less system. This allows for the investigation the coulombic efficiency of each system where there is not an unlimited source of Mg, which would give higher efficeincies.[31,32] To initially compare the different electrolytes, CVs were measured in the same experimental conditions to compare their CE. These conditions were between the potentials of -0.7 and 0.8 V vs Mg^{2+}/Mg at a Cu WE and Mg RE and counter electrode, at a scan rate of 100 mV s^{-1}.

The first system looked at was $Mg(TFSI)_2$/2G, similar to the system from Chapter 3 but with a shorter glyme ether chain, Figure 4.3a. Through progressive cycles, the peak current density stays constant and doesn't increase

over cycling, and the stripping peak reaches its maximum current density after 5 cycles and stabilises, with a slight variation over further cycling. This indicates that the conditioning process and interphase formation occur over those first 5 cycles, and the slight variation in peak current density over further cycling is likely from small changes in the interphase, either cracking or passivation. The potential at which plating occurs remains constant over the 30 cycles, at -0.38 V vs Mg^{2+}/Mg, and the potential at which stripping occurs also remains constant at 0.08 V vs Mg^{2+}/Mg.

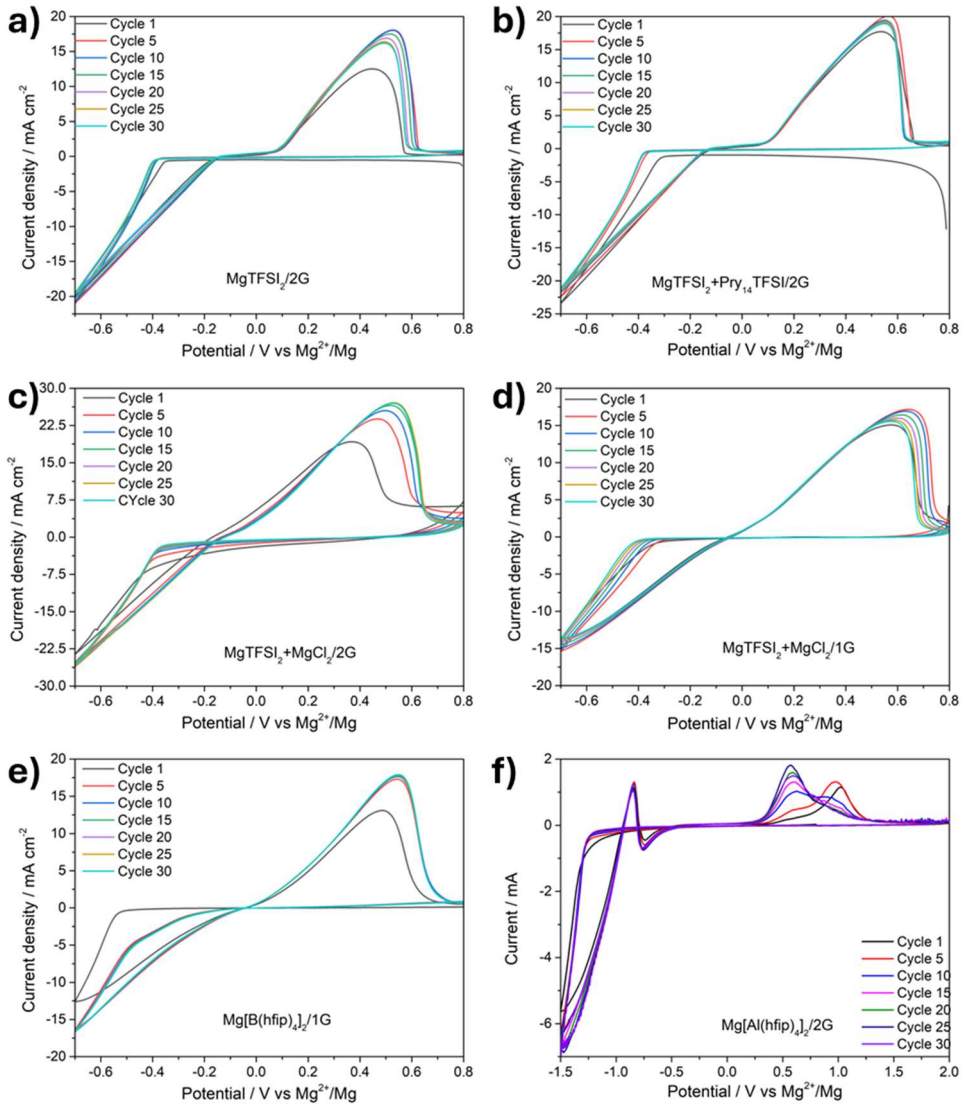

Figure 4.3, Cyclic voltammetry of (a) $Mg(TFSI)_2$/2G, (b) $Mg(TFSI)_2$+$Pry_{14}TFSI$/2G, (c) $Mg(TFSI)_2$+$MgCl_2$/2G, (d) $Mg(TFSI)_2$+$MgCl_2$/1G, (e) $Mg[B(hfip)_4]_2$/1G and (f) $Mg[Al(hfip)_4]_2$/2G. All CVs were recorded at a Cu working electrode with a Mg counter and reference and at a scan rate of 100 mV s^{-1} over 30 cycles.

The next electrolyte system looked at was $MgTFSI_2$+$Pry_{14}TFSI$/2G, Figure 4.3b. In the literature, it was reported that the addition of the Pry14TFSI helps suppress the uneven deposition of Mg through the adsorption of the IL onto the electrode surface, forming an artificial SEI.[19] As with the $MgTFSI_2$/2G system, the peak current density for the plating of Mg stays almost constant, with a slight decrease over 30 cycles. A notable difference between these 2 electrolytes is that for the $Pry_{14}TFSI$ system there is an initial negative current at 0.8 V vs Mg^{2+}/Mg at the start of the CV. This reduction current is likely to be the decomposition of $Pry_{14}TFSI$ to form an artificial interphase. The onset potential for the plating, however, does become more negative, from -0.31 V to -0.38 V vs Mg^{2+}/Mg. For the stripping peak, the onset remains the same, and after 5 cycles, the peak current density remains constant.

The addition of chloride in literature has been extensively shown to improve the performance of Mg batteries.[16,33] Therefore, the next electrolyte system to be looked at was the addition of 0.125 M $MgCl_2$ to the 0.25 M $Mg(TFSI)_2$ 2G, giving a ratio of $MgCl_2$:$Mg(TFSI)_2$ of 1:2. During the CVs of $MgTFSI_2$+$MgCl_2$/2G, there is a slight increase in the plating current density whilst the stripping current density increases up to cycle 20, where it reaches its maximum, Figure 4.3c. The onset for the plating of Mg is -0.4 V vs Mg^{2+}/Mg, whilst the onset potential for stripping is -0.1 V vs Mg^{2+}/Mg. This system has the smallest potential difference between plating and stripping than other electrolytes. Ideally, the potential difference between plating and stripping would be 0 V, as seen in Grignard reagent CVs, where a small change in potential around the central point would drive the process in one direction, Figure A6.[34]

Changing between glyme ether solvents can also affect the performance of the electrolyte due to their different viscosities and salt saturation concentration limits.[35,36] In 2G, the highest ratio of $MgCl_2$ to $Mg(TFSI)_2$ was 1:2, respectively, as any higher concentration of $MgCl_2$ caused it to precipitate from the solution. Whereas in 1G, the highest ratio of $MgCl_2$ to $Mg(TFSI)_2$ was 2:1, respectively, the concentration used was 0.25 M $MgCl_2$ and 0.125 M $Mg(TFSI)_2$ in 1G. For $MgTFSI_2$+$MgCl_2$/1G, there is a slight decrease in the maximum plating

current density, Figure 4.3d, and the potential at which plating starts does increase through cycling from -0.36 V to -0.43 V vs Mg^{2+}/Mg; this is potentially due to surface passivation as the maximum current densities for both plating and stripping decrease through continued cycling.

The final electrolyte systems to compare are the synthesised fluorinated alkoxy borate and aluminate salts. These salts were used in the solvents and concentrations reported in the literature.[36,37] For the $Mg[B(hfip)_4]_2$/1G over the first 5 cycles, the current densities for both plating and stripping reach their peak, Figure 4.3e. The onset potential of plating decreases significantly from -0.6 V to -0.3 V Mg^{2+}/Mg, with the onset for stripping being 0.05 V Mg^{2+}/Mg. For the aluminate electrolyte system $Mg[Al(hfip)_4]_2$/2G the performance is poor as large overpotentials are needed to both plate and strip the Mg on the electrode surface, Figure 4.3f, -1.3 and 0.25 V Mg^{2+}/Mg, respectively. This is likely due to impurities left from the synthesis of the salt, such as the extra peak in the ^{19}F NMR spectrum, but further work is required to improve the performance of this electrolyte system and going forward with comparing the above electrolytes $Mg[Al(hfip)_4]_2$/2G will not be included.

A main way to compare the CVs shown in Figure 4.3 is to compare their CE over successive cycles, Figure 4.4. The CEs for the $Mg(TFSI)_2$/2G and $MgTFSI_2$+$MgCl_2$/2G electrolyte systems follow a similar trend; for the first five cycles the CE increases until it plateaus, this is likely due to the formation of a stable interphase on the electrode surface. Towards the end of the 30 cycles, the CE of $MgTFSI_2$/2G starts to decrease, suggesting that the interphase is not stable and starts to react and degrade over time. This is likely due to the volume expansion that occurs on the electrode surface during cycling causing fractures of the interphase, revealing more reactive Mg which will react, causing further electrolyte degradation. For the $MgTFSI_2$+$Pry_{14}TFIS$/2G electrolyte system the CE remains steady over the 30 cycles after a lower CE on the first cycle. This lower CE on the first cycle is due to the initial reduction observed in the CV cycling, Figure 4.3b. The systems with the highest average CE are $Mg[B(hfip)_4]_2$/1G and $MgTFSI_2$+$MgCl_2$/1G, with an average CE of 95 %. These

two systems also have high CE during their initial cycles and show little variation over the 30 cycles compared to the other systems tested. This implies that the conditioning step in these electrolytes doesn't hinder the initial CE as there is no increase in CE over the initial cycles as seen in previous systems.

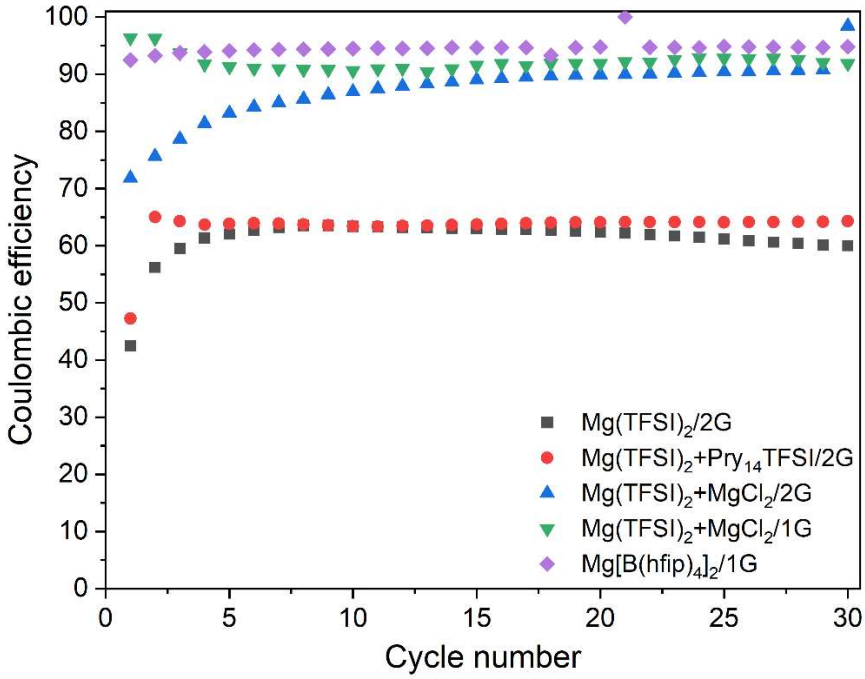

Figure 4.4, Coulombic efficiency comparison of the cyclic voltammograms of the different electrolyte systems in Figure 4.3.

Mg electrolytes require high oxidative stability, as this allows for higher potential positive electrodes to be used. To compare the oxidative stability of each electrolyte LSVs were measured to see when electrolyte degradation occurred. The LSVs for $MgTFSI_2$/2G and $MgTFSI_2$+$Pry_{14}TFSI$/2G are similar as when using a Pt or glassy carbon (GC) working electrode. The current starts to increase exponentially at 4.1 and 4 V, respectively vs Mg^{2+}/Mg, Figure 4.5a and b. There is a slight difference when using a Cu working electrode as the current increase for $MgTFSI_2$+$Pry_{14}TFSI$/2G is steeper than that of $MgTFSI_2$/2G, but the currents increase at 2.5 and 2.6 V, respectively. When $MgCl_2$ is included in the electrolyte, $MgTFSI_2$+$MgCl_2$/2G, there are differences in the LSVs compared to without $MgCl_2$, Figure 4.5c. The LSV with the GC working electrode is the same as that of $MgTFSI_2$/2G, but with the Pt working electrode LSV, there is an

oxidation peak before the exponential increase in current; this increase is likely due to chloride oxidation at the electrode surface.[38] With the Cu working electrode, there are two oxidation processes before the fast increase in current, and these are likely caused by the oxidation of copper to form copper chloride in the electrolyte solution.

When changing from 2G to 1G, there is a surprising difference when comparing the LSVs. Cu has the lowest oxidative stability for the 2G electrolyte containing $MgCl_2$, whereas in 1G, it's the highest, and the copper oxidation peak isn't observed. This difference in electrochemical stability is likely down to the chelation of the solvent 2G and 1G to the Mg ions in solution. Chelation has previously been shown to adjust the electrochemical properties of metal ions, including transfer kinetics and redox potentials.[39] The onset for the GC and Pt electrodes is earlier than that of those in 2G by 0.5 V. When looking at the LSVs for $Mg[B(hfip)_4]_2$/1G, the potential that the current for electrolyte degradation increases at 4 V vs Mg^{2+}/Mg. Comparing the 1G and 2G LSVs indicates that Cu degrades 2G easier than 1G due to the much lower onset potential for electrolyte degradation, about 1.5 V difference.

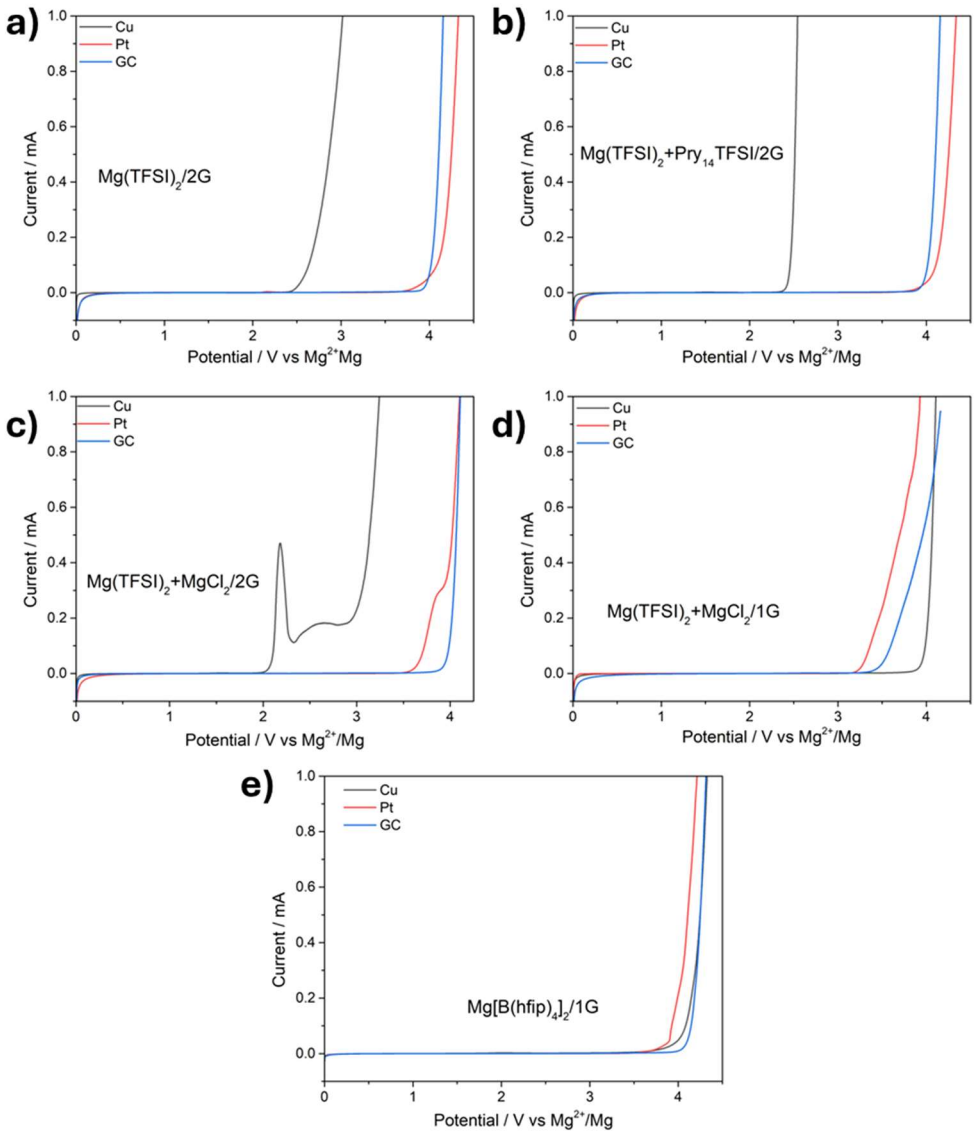

Figure 4.5 Linear sweep voltammograms of (a) $MgTFSI_2$/2G, (b) $MgTFSI_2$+$Pry_{14}TFSI$/2G, (c) $MgTFSI_2$+$MgCl_2$/2G, (d) $MgTFSI_2$+$MgCl_2$/1G and (e) $Mg[B(hfip)_4]_2$/1G. LSVs were recorded with a Cu, Pt and glassy carbon working electrode with a magnesium counter and reference. LSVs were recorded between 0 and 4.5 V vs Mg^{2+}/Mg at a scan rate of 10 mV s^{-1}.

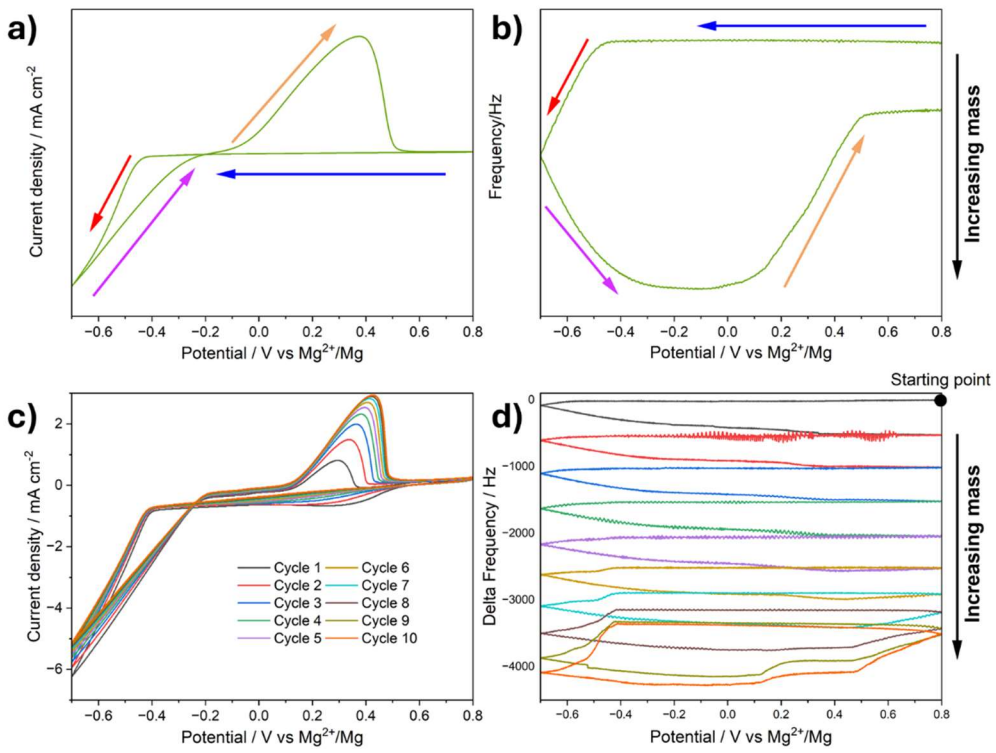

Figure 4.6, Example cyclic voltammogram (a) and frequency response (b) of Mg plating and stripping with the arrows showing the cycling direction. Cyclic voltammograms of (c) $MgTFSI_2$/2G, along with the EQCM frequency potential plot (d), with the starting point of the frequency plot labelled. Cyclic voltammograms were recorded at an Au EQCM quartz crystal working electrode with a Mg counter and reference at a scan rate of 100 mV s^{-1}.

The CVs recorded at the Au EQCM electrode all have a lower CE than those recorded with the Cu WE. This is because different electrodes can lead to different electrochemical responses, gold is less electrochemically active than copper, and with the need to use a larger quantity of electrolytes due to the larger cell volumes, the amount of impurities present would be higher, leading to more potential passivation of the electrode surface.[40] Figures 4.6a and b show examples of an EQCM plot with the arrows showing the direction of cycling and the colours to link corresponding processes. All EQCM data presented in this section starts from the top right of the plot as this is where the change in frequency is 0 and the starting potential is 0.8 V vs Mg^{2+}/Mg. Once the EQCM measurements begin the potential sweeps negative, the blue

arrow in Figure 4.6a and b, until the current starts to go negative, the red arrow. This increase in current also leads to an increase in magnitude of the change in frequency which corresponds to an increase in mass. Material is then continually plated on to the surface whilst the current is negative, purple arrow, up until the current crosses over. The positive stripping current is then measured which corresponds to a decrease in magnitude in the change in frequency on the EQCM plot. This relates to a decrease in mass on the electrode surface.

The CE for the CVs taken in the EQCM cell for $MgTFSI_2$/2G, Figure 4.6c, averages 18 %. The poor efficiency is seen as the CV has a small stripping current, relative to the plating current, and this reduction in CE is likely due to the factors mentioned above. The frequency response of this system is surprising. For the first cycle, the plating of material onto the electrode doesn't begin until -0.60 V vs Mg^{2+}/Mg, whereas in the CV, the plating process starts at -0.41 V; this discrepancy in plating potential only appears during the first cycle, then afterwards, the potential at which plating starts is the same.

Over the first 6 cycles record, once the potential reaches the stripping process in the CV, there is no corresponding decrease in magnitude of the frequency, i.e. moving closer to 0. Instead, the frequency increases in magnitude, indicating an increase in mass on the electrode. This is not in the potential region where Mg is plated on the electrode surface, which likely corresponds to the reaction between the plated Mg metal and the electrolyte or impurities in the electrolyte. These reactions then lead to forming an SEI. At the 6th cycle, Mg starts to be stripped from the surface, reaching 100 % stripping efficiency in cycle 10. This 100 % efficiency in stripping likely isn't caused by the electrochemical process, on the 10^{th} cycle in the EQCM plot, Figure 4.6d, between 0.1 and 0.5 V vs Mg^{2+}/Mg there is a small amount of the Mg stripped from the surface, and this section matches up with the stripping peak in the voltammetry, Figure 4.6c. After this, a large amount of material is removed whilst no charge is being passed, meaning this is likely due to the detachment of the Mg deposits from the electrode surface and these then dissolving into

the solution, giving the appearance of 100 % stripping efficiency. This would then lead to a loss of active material from the electrode surface, which would significantly impact the battery's performance.

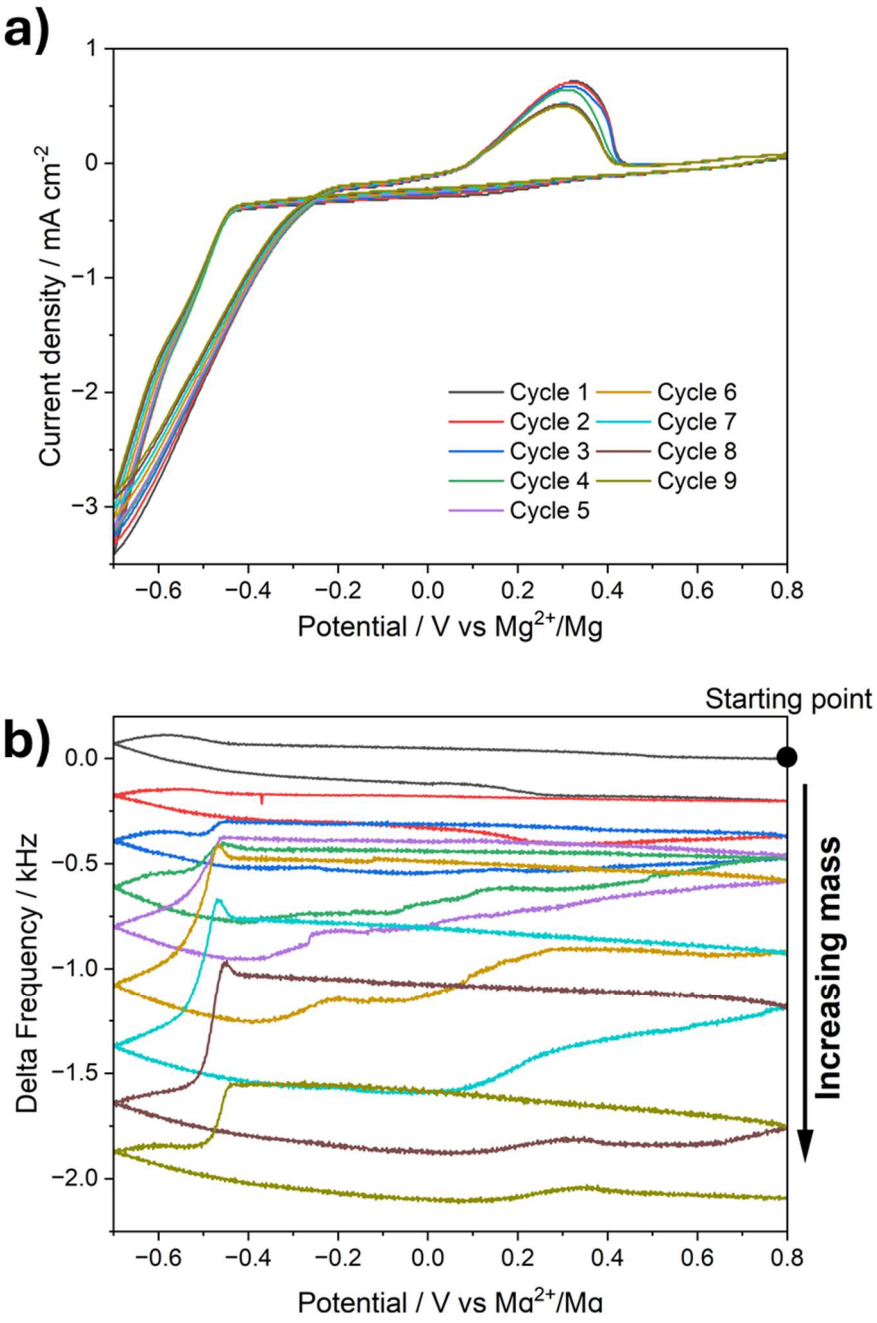

Figure 4.7, cyclic voltammograms of (a) $MgTFSI_2$+$Pry_{14}TFSI$/2G, along with the EQCM frequency potential plot (b) with the starting point of the frequency plot labelled. Cyclic voltammograms were recorded at an Au EQCM quartz crystal working electrode with a Mg counter and reference at a scan rate of 100 mV s^{-1}.

For the EQCM measurements of the $MgTFSI_2$+$Pry_{14}TFSI$/2G, the CE is again much lower than that recorded against the Cu WE earlier, 10 % in the EQCM cell, Figure 4.7a. The change in the frequency value at -0.6 V vs Mg^{2+}/Mg during the first cycle is likely due to impurities on the electrode surface, Figure 4.7b. Then as with $MgTFSI_2$/2G, in the region where stripping of Mg typically occurs, at 0.15 V vs Mg^{2+}/Mg on the positive potential sweep, there is an increase in the frequency magnitude, meaning that the plated Mg is likely reacting with the electrolyte to form an interphase, and this process occurs for the first two cycles, after which the frequency magnitude decreases in that potential region implying that Mg is being stripped form the electrode surface. Unlike $MgTFSI_2$/2G, material removal of material from the electrode surface mainly occurs when a stripping current is passed. So, the deposits do not detach from the electrode surface, causing a loss of materials.

Adding magnesium chloride to $MgTFSI_2$/2G to $MgTFSI_2$+$MgCl_2$/2G improves the performance of the EQCM cell. The voltammetry is more consistent, with a CE of around 60 %, Figure 4.8a. The frequency response with the EQCM is also more consistent through progressive cycles, and frequency changes mainly occur when current is passing for either plating or stripping, Figure 4.8b, leading to an increase and decrease in the frequency magnitude respectively. After the first cycle, the amount of Mg plated onto the electrode surface stays consistent with each cycle, with a frequency magnitude increasing approximately 500 Hz. The first cycle has a larger frequency magnitude increase due to having a larger active surface area before any passivation has occurred. The average stripping efficiency of the last 9 cycles is ~ 50 %. At the end of each cycle, once Mg has been stripped from the surface at 0.49 V vs Mg^{2+}/Mg, the frequency magnitude increases afterwards. This frequency increase doesn't correspond to a current being passed, so it can be attributed to the reaction between the electrolyte and the bare Mg left on the surface, contributing to the poorer stripping efficiency.

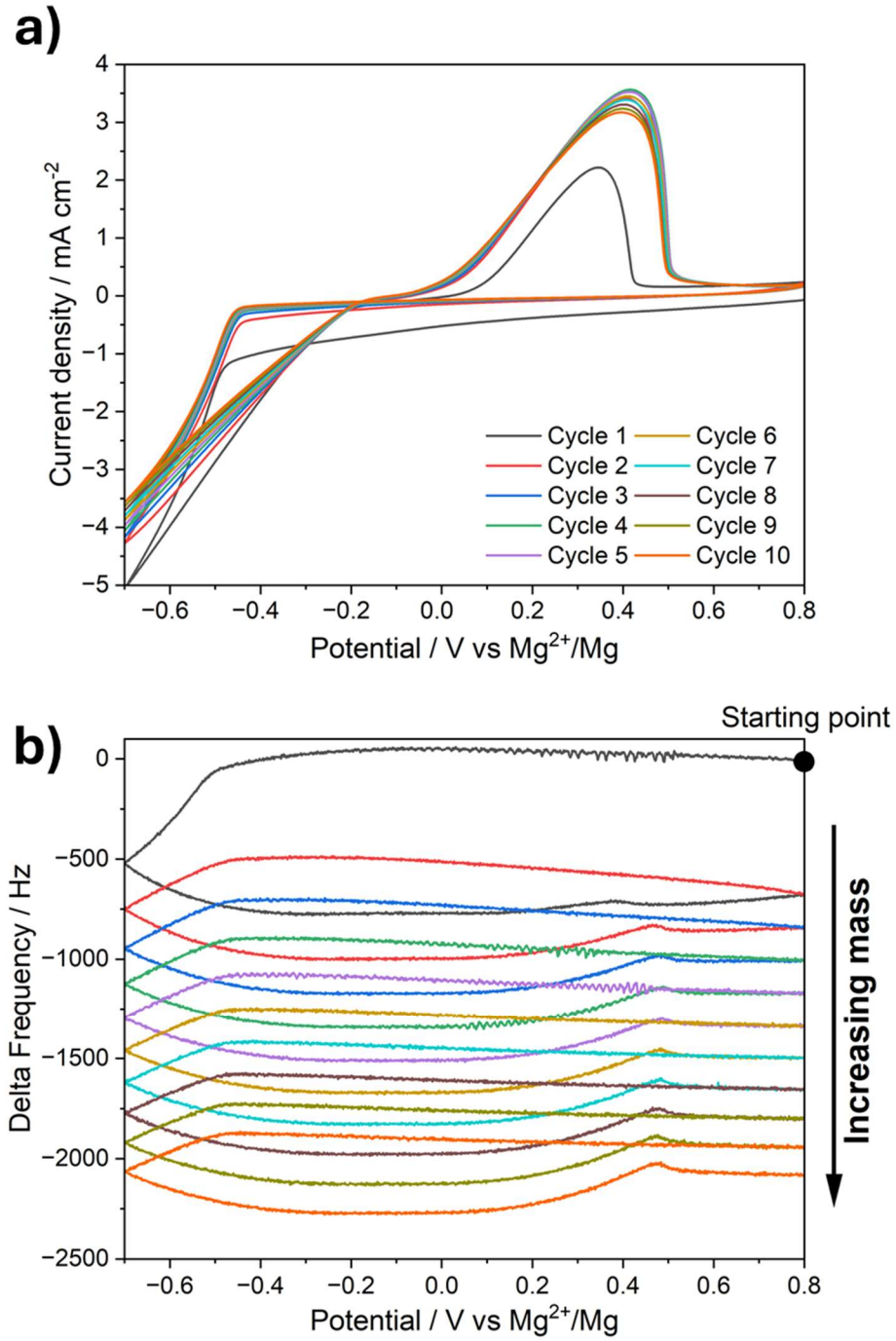

Figure 4.8, cyclic voltammograms of (a) $MgTFSI_2$+$MgCl_2$/2G, along with the EQCM frequency potential plot (b) with the starting point of the frequency plot labelled. Cyclic voltammograms were recorded at an Au EQCM quartz crystal working electrode with a Mg counter and reference at a scan rate of 100 mV s^{-1}.

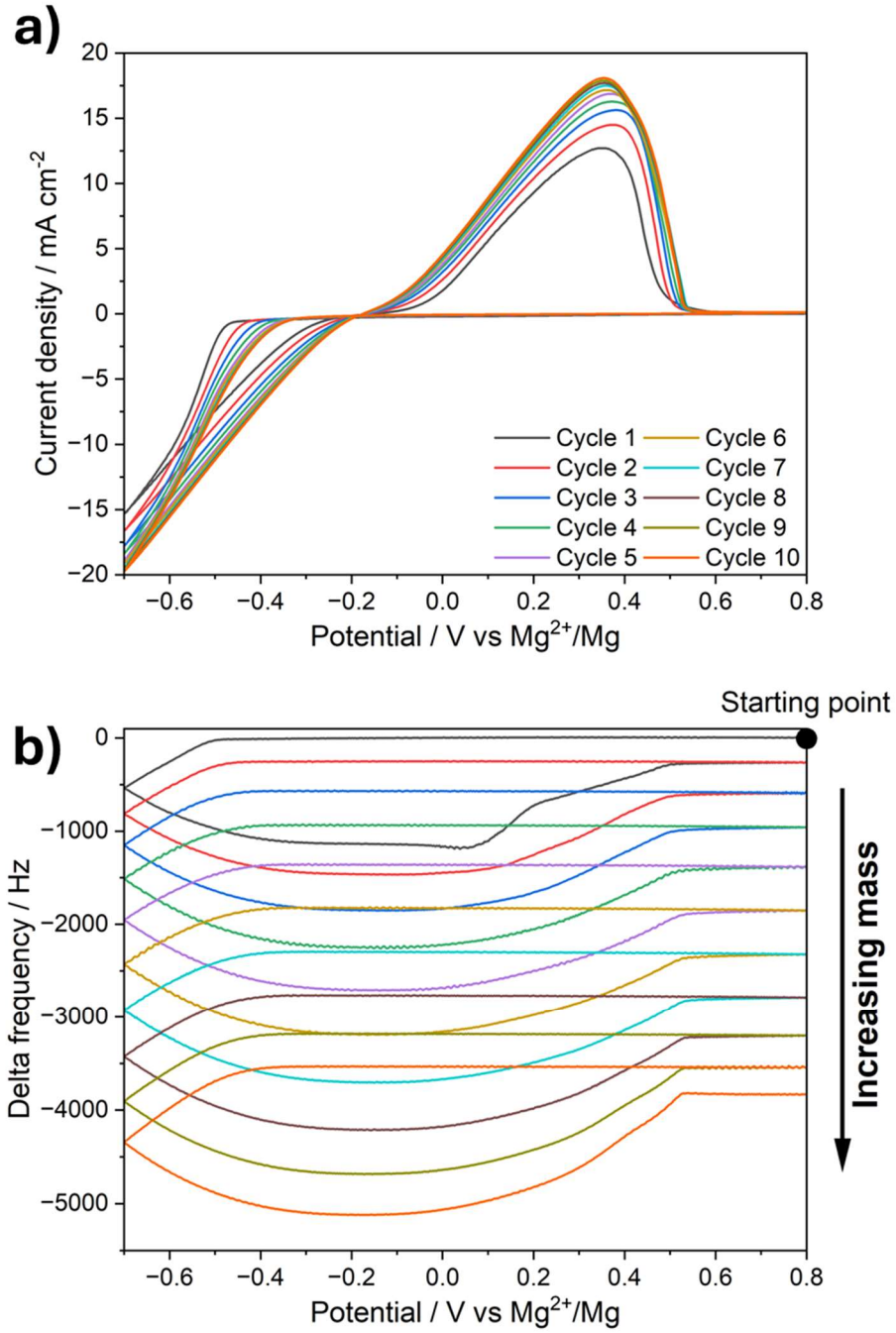

Figure 4.9, cyclic voltammograms of (a) $MgTFSI_2$+$MgCl_2$/1G, along with the EQCM frequency potential plot (b) with the starting point of the frequency plot labelled. Cyclic voltammograms were recorded at an Au EQCM quartz crystal working electrode with a Mg counter and reference at a scan rate of 100 mV s^{-1}.

When changing from 2G to 1G, there is significant improvement in the CE in the EQCM cell, up to 85 %, and the peak current density for both the plating and stripping have also increased. This increase in current and charge passed

during cycling means a larger frequency magnitude increase is observed, a 1500 Hz increase per cycle. In the first cycle, after plating Mg at -0.2 V vs Mg^{2+}/Mg on the reverse sweep, there is a slight mass increase at 0.02 V vs Mg^{2+}/Mg before Mg is stripped from the surface. This mass increase is likely the reaction of electrolyte with fresh Mg which has become available following the initial stripping of materisl. Following the first cycle, the plating and stripping go in a loop with no other observable processes present apart from the plating and stripping of Mg. This gives an average stripping efficiency of 70 %.

The final electrolyte system to compare is $Mg[B(hfip)_4]_2$/1G. A wider potential window was needed for the EQCM measurements of $Mg[B(hfip)_4]_2$/1G, this is due to a late onset potential of plating in the EQCM cell, Figure 4.10a. For the first four cycles, the stripping efficiency gradually increases from 30 % up to 90 %, after which each cycle's plating and stripping efficiency is 100 %, Figure 4.10b. This increase over the first few cycles is due to the formation of an SEI, which then allows for the reversible plating and stripping of Mg in later cycles. With each cycle, the onset of plating and stripping also reduce, going from -0.71 V to -0.56 V and -0.17 to -0.2 vs Mg^{2+}/Mg, meaning the overpotential between plating and stripping is reduced. Its also observed that the magnitude of the frequency increase during each plating step increase from ~ 1100 Hz during the first cycle to ~3000 Hz during the tenth cycle. This increase in amount of Mg plated on to the electrode surface is likely due to the increase in Mg coverage over the initial cycles increasing the amount of active sites for Mg to plate on the surface. A key difference between the $Mg[B(hfip)_4]_2$ is that for the stripping process during the first few cycles it appears as two peaks which merge over successive cycling. This additional oxidation peak could be due to the oxidation of the electrolyte salt with the Au electrode, as it isn't seen with the Cu electrode, but this would need to be investigated further.

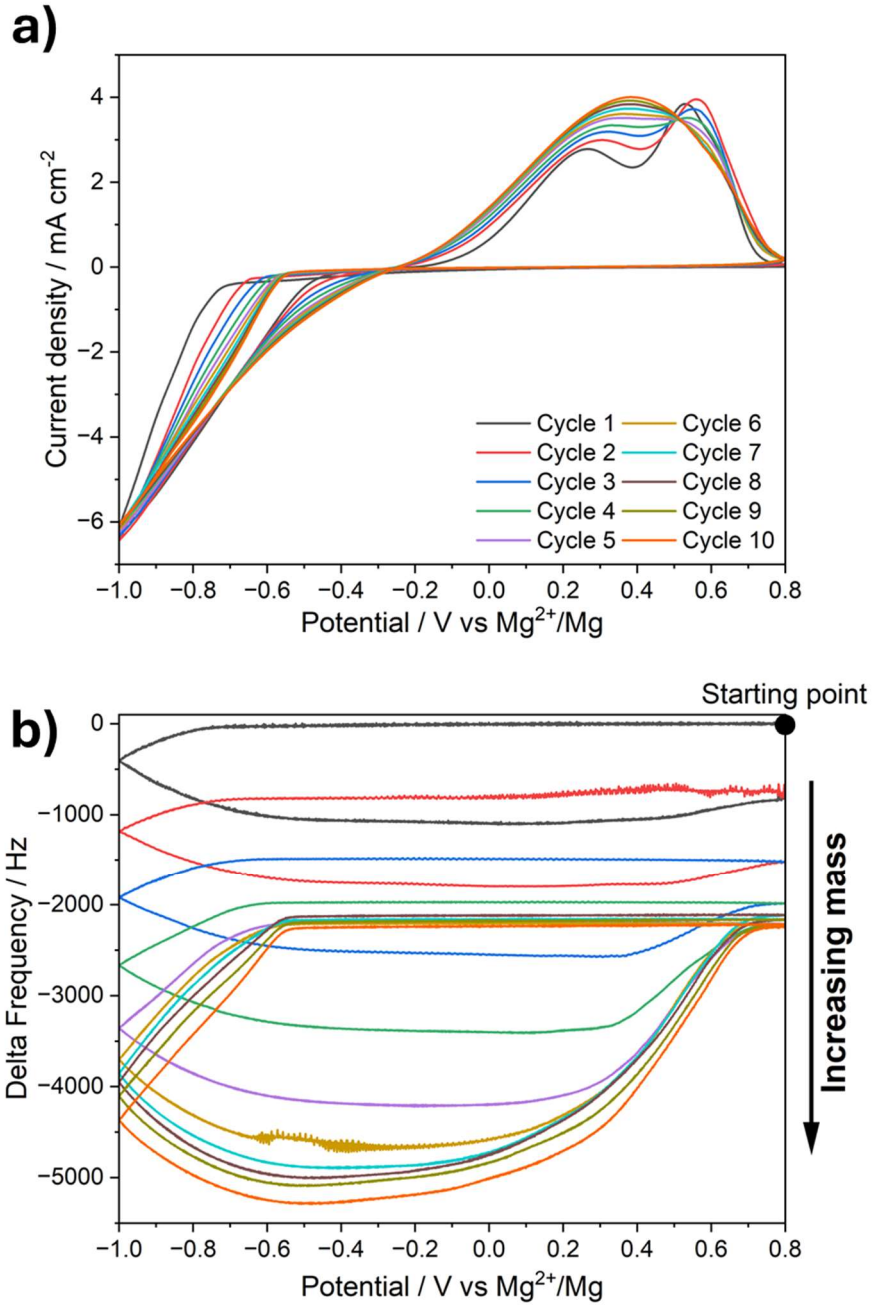

4.10, cyclic voltammograms of (a) $Mg[B(hfip)_4]_2$/1G, along with the EQCM frequency potential plot (b) with the starting point of the frequency plot labelled. Cyclic voltammograms were recorded at an Au EQCM quartz crystal working electrode with a Mg counter and reference at a scan rate of 100 mV s^{-1}.

4.2.3 Electrode morphology of different electrolyte systems

Another key aspect of the different electrolytes to investigate is how cycling changes the surface of the electrode. For an ideal system, all the Mg plated on to the electrode surface would be removed during stripping, leaving no inactive material on the surface. However, from the EQCM measurements and previous work, Chapter 3, we know from the electrode's cycling mechanism that growth of these deposits occurs over time.

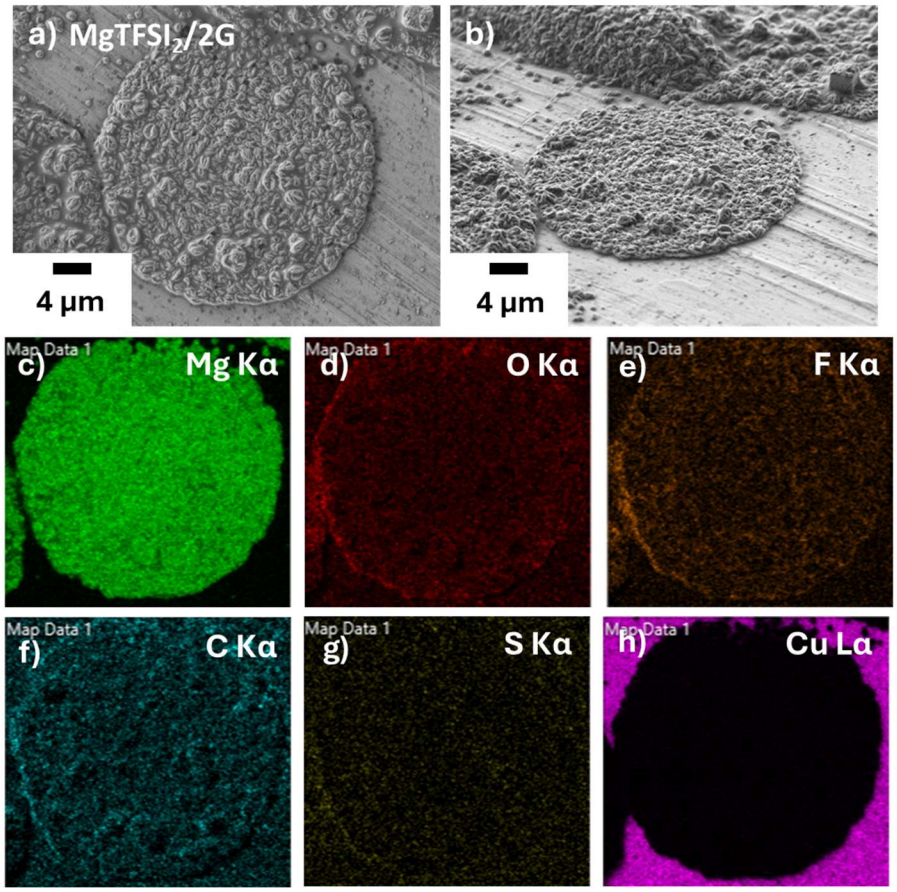

Figure 4.11, SEM images of (a and b) $MgTFSI_2$/2G, (c-h) corresponding EDX maps for (c) Mg, (d) O, (e) F, (f) C, (g) S and (h) Cu. All images are after 30 cycles between -0.7 and 0.8 V vs Mg^{2+}/Mg, at a scan rate of 100 mV s^{-1} and are on a Cu ribbon electrode and after discharge.

When looking at the surface morphology for each electrolyte system, all the surface deposit morphologies are different from each other. For the $MgTFSI_2$/2G electrolyte system, the Mg deposits form flat, pancake-like structures over the electrode surface, Figure 4.11a and b. There are some areas

where these flat structures overlap and form higher domed ridge structures, as seen at the top of Figure4.11b. These flat disc structures, which form, seem to be made up of concentric rings of deposited Mg, Figure 4.11a, suggesting that there is an initial nucleation on the electrode surface; grooves can be seen in Figure 4.11b below the deposit, which are more favourable nucleation sites. From the initial nucleation deposit, the sites adjacent to it must then be more favourable for further nucleation and deposit growth. The EDX maps for $MgTFSI_2$/2G deposits show a high concentration of Mg in the deposit, which would agree with the poor stripping seen in the EQCM, along with O and F on the surface of the deposit, which would be present from the degradation of 2G and $TFSI^-$, Figure 4.11c-h. The uniform C presence is from the degradation of 2G.

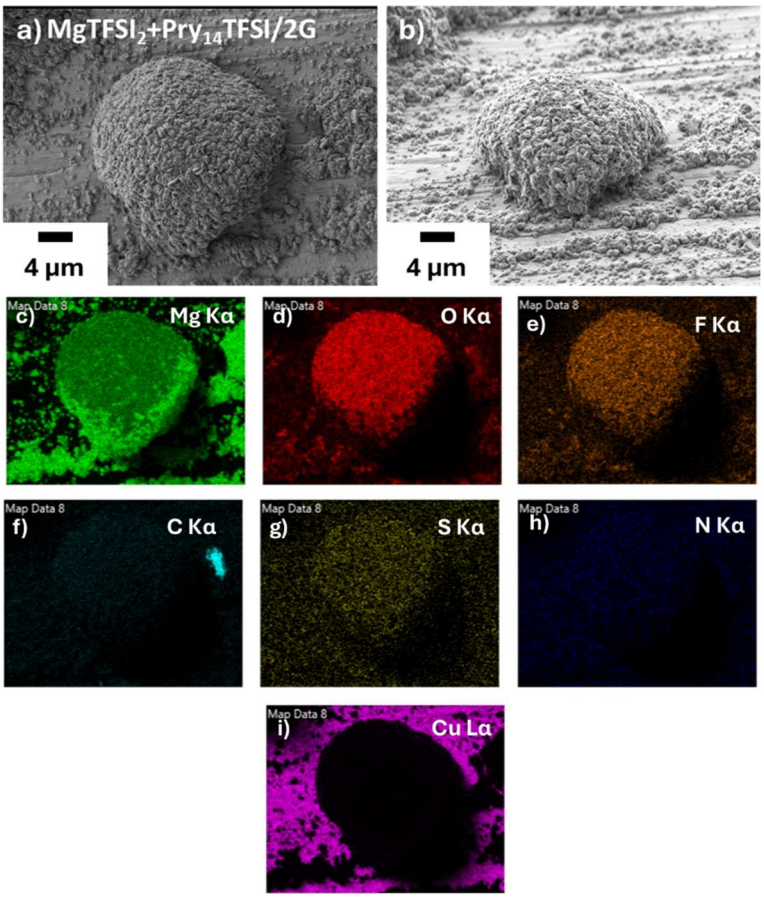

Figure 4.12, SEM images of (a and b) $MgTFSI_2$+$Pry_{14}TFSI$/2G, (c-i) corresponding EDX maps for (c) Mg, (d) O, (e) F, (f) C, (g) S, (h) N and (i) Cu. All images are after 30 cycles between -0.7 and 0.8 V vs Mg^{2+}/Mg, at a scan rate of 100 mV s^{-1} and are on a Cu ribbon electrode and after discharge.

The $MgTFSI_2$+$Pry_{14}TFSI$/2G forms different structures than $MgTFSI_2$/2G, even though the only difference in the electrolyte system is 10 mM $Pry_{14}TFSI$. $MgTFSI_2$+$Pry_{14}TFSI$/2G forms a mixture of small hemispherical deposits, ~16 µm in size, along with much smaller, sub-micron size structures littering the electrode surface, Figure 4.12a and b. There are also areas on the electrode surface where these larger hemispherical structures have nucleated so close together that the deposits agglomerate into thick surface coverings, Figure A7. The EDX maps of the deposit, Figure 4.12c-i, show a high concentration of Mg, O and F in the deposit but only trace amounts of N are present.

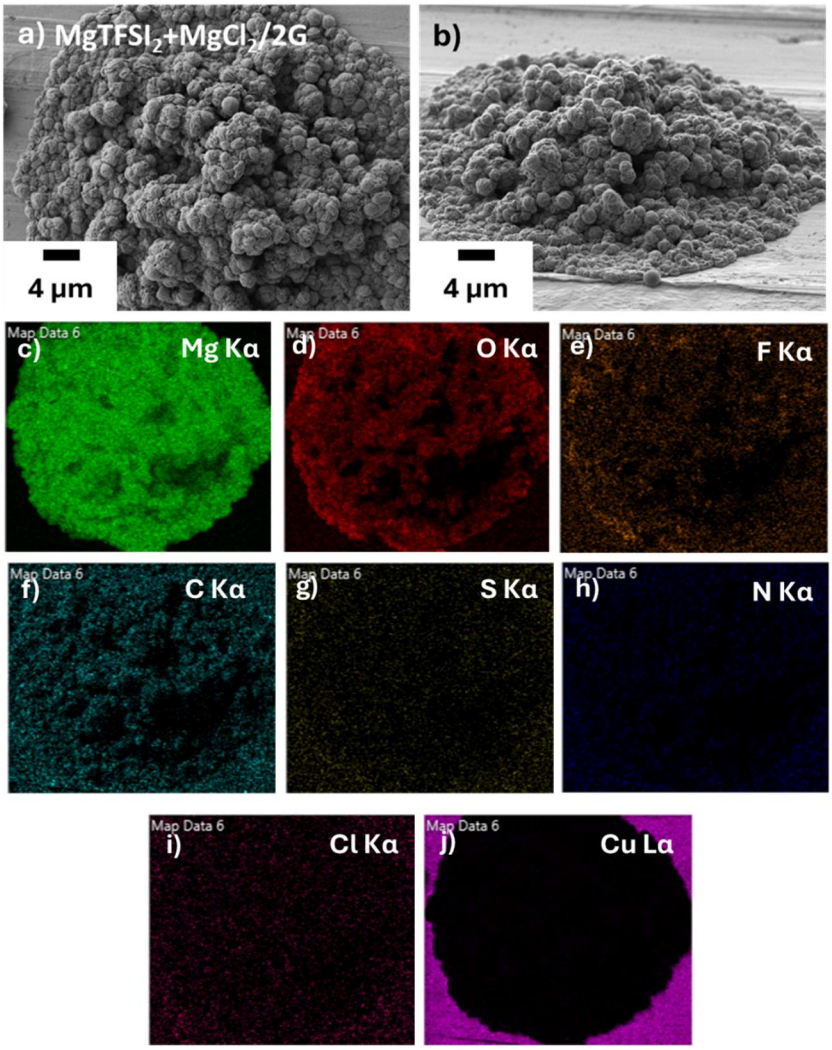

Figure 4.13, SEM images of $MgTFSI_2$+$MgCl_2$/2G, (c-j) corresponding EDX maps for (c) Mg, (d) O, (e) F, (f) C, (g) S, (h) N, (i) Cl and (j) Cu. All images are after 30 cycles between -0.7 and 0.8 V vs Mg^{2+}/Mg, at a scan rate of 100 mV s^{-1} and are on a Cu ribbon electrode and after discharge.

For the $MgTFSI_2$+$MgCl_2$/2G electrolyte system, the deposit structure is similar to that seen in the $MgTFSI_2$/2G system. The deposits seem to form a disc like the $MgTFSI_2$/2G systems but then deposits also seem to grow on top of this disc, forming a hilly agglomerate structure, Figure 4.13a and b, and these hilly disc structures are the primary structure of deposits which form on the electrode surface. The main elements present in these deposits are Mg, O and F, as before, with C seeming to coat the structure, Figure 4.13c-j. Considering that the ratio of TFSI to Cl is 2:1, its surprising that there is a very small presence of Cl in the EDX map, indicating that the chloride is washed off during the sample preparation step for the SEM samples.

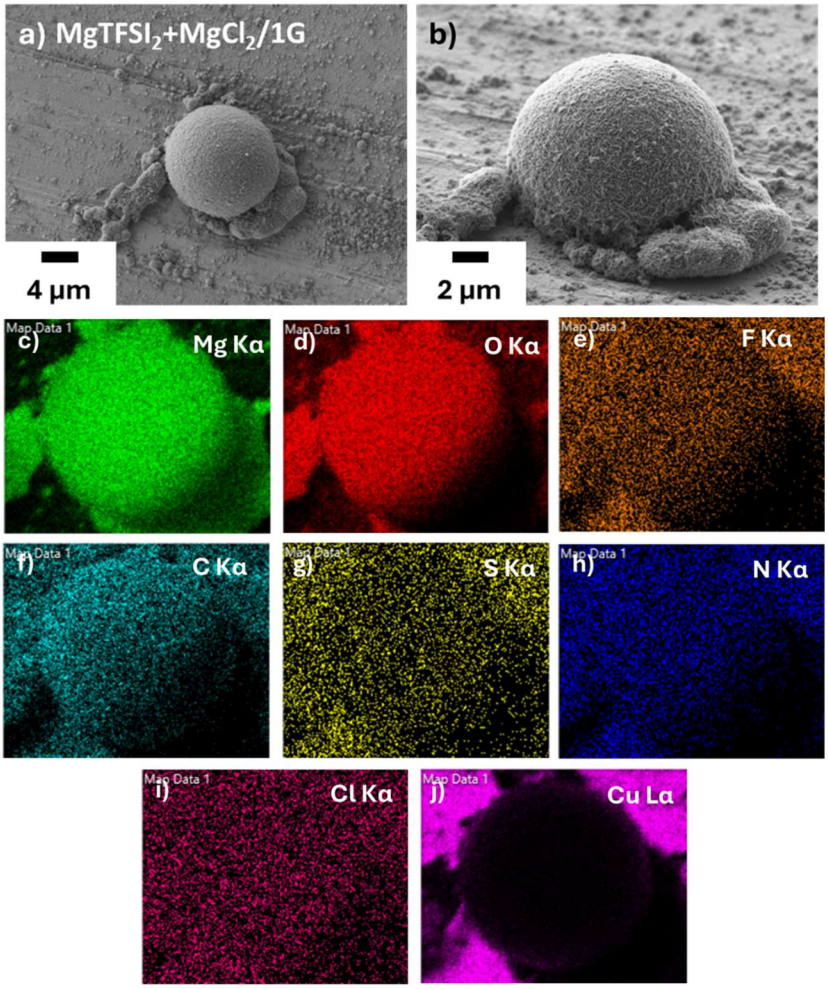

Figure 4.14, SEM images of (a and b) $MgTFSI_2$+$MgCl_2$/1G, (c-j) corresponding EDX maps for (c) Mg, (d) O, (e) F, (f) C, (g) S, (h) N, (i) Cl and (j) Cu. All images are after 30 cycles between -0.7 and 0.8 V vs Mg^{2+}/Mg, at a scan rate of 100 mV s^{-1} and are on a Cu ribbon electrode and after discharge.

The structures are significantly different when the solvent is changed from 2G to 1G. For the $MgTFSI_2$+$MgCl_2$/1G electrolyte system, discreet hemispheres are formed on the electrode surface; Figure 4.14 a and b are much smaller than the deposits seen with the other electrolyte systems. Like the other electrolytes, these hemispheres cover most of the electrode surface along with much smaller deposits, the small structures seen around the deposit in Figure 4. 14a and b. The much smaller deposits likely lead to the high efficiency seen in the CVs and EQCM measurements; with them being smaller, the diffusion of Mg in and out of the structure is easier, allowing for higher efficiency. The EDX maps for this system, Figure 4.14c-j, show that the main elements present in the deposit are Mg and O, which are only located in the deposit from the maps. The other elements, F, S, N, C, and Cl, all seem uniform over the mapping area due to electrolyte degradation, with one side of the maps, bottom right, being darker due to the 3 dimensionality of the structure.

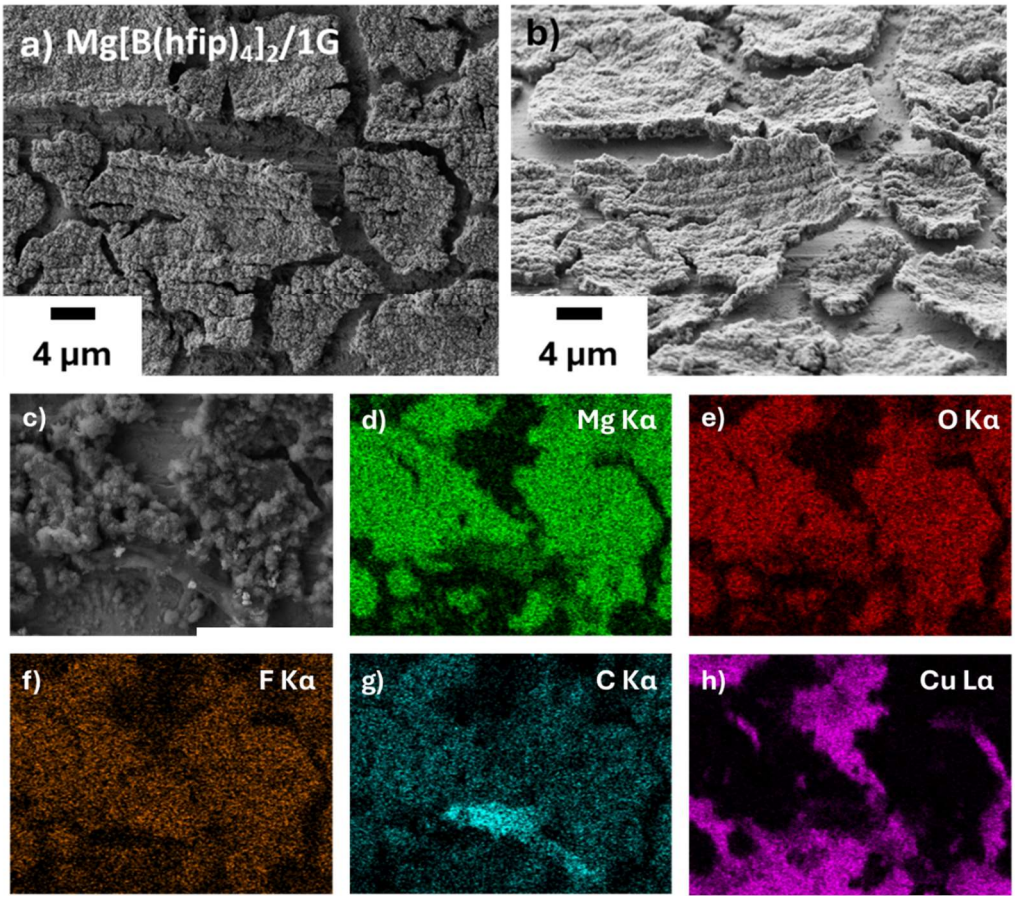

Figure 4.15, SEM images of (a and b) $Mg[B(hfip)_4]_2$/1G, (d-h) corresponding EDX maps for (d) Mg, (e) O, (f) F, (g) C and (h) Cu all to the same scale as (c) which has a scale bar of 5 µm. All images are after 30 cycles between -0.7 and 0.8 V vs Mg^{2+}/Mg, at a scan rate of 100 mV s^{-1} and are on a Cu ribbon electrode and after discharge.

When changing to the $Mg[B(hfip)_4]_2$/1G electrolyte system, another morphology is observed. After cycling in this system, the electrode surface shows platelets covering the electrode surface with cracks throughout the structure with some curling observed, Figure 4.15a-c. The curling and cracking observed are likely from the preparation of the electrodes for imaging. This is more towards the ideal scenario for Mg plating and stripping, where a uniform layer of deposition forms. The EDX maps of $Mg[B(hfip)_4]_2$/1G, Figure 4.15d-h, show that the deposit plates consist of mainly Mg and O with some F present in the structure as well; B isn't detectable with EDX; thus isn't shown in the maps. At higher magnifications, the surface of the deposits varies with respect to the solvent used, either 1G or 2G, Figure A8. The surface of the deposits formed in the 2G electrolytes form thick crystalline rods, Figures A8a and b,

whilst those in the 1G electrolyte form thin plate structures, Figures A8 c and d. This is potentially due to the solvation shell around the Mg ions affecting how they plate and potentially react with other species in solution once on the electrode surface.

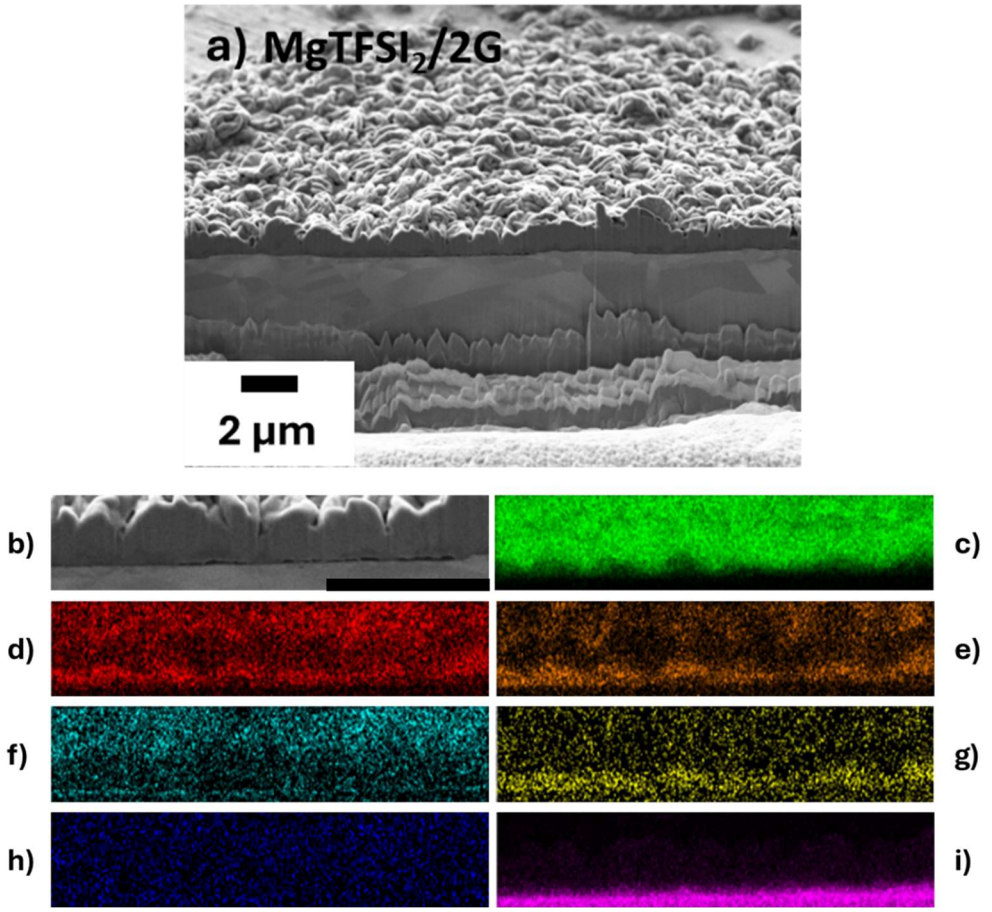

Figure 4.16, Cross sectional SEM images of (a and b) $MgTFSI_2$/2G, (c-i) EDX maps for (c) Mg, (d) O, (e) F, (f) C, (g) S, (h) N and (i) Cu. EDX maps all to the same scale as (b) which has a scale bar of 2.5 µm. All images are after 30 cycles between -0.7 and 0.8 V vs Mg^{2+}/Mg, at a scan rate of 100 mV s^{-1} and are on a Cu ribbon electrode and after discharge.

Cross-sectioning was carried out to understand the internal structure and gain insight into how these deposits grow and to understand the cycling mechanism of all these systems fully. The cross-section of the deposits formed in the $MgTFSI_2$/2G shows that the disc-like structures are dense with deposited material, showing no internal porosity or cavities, Figure 4.16a and b. The EDX maps show the bulk of the internal structure is Mg, with the maps for the other

elements being sparse in the centre but more concentrated on the exterior, Figure 4.16c-i. This suggests that the plated Mg is trapped under an impassable layer of MgO, MgF_2 and other electrolyte degradation products, leading to poor cycling and stripping efficiency.

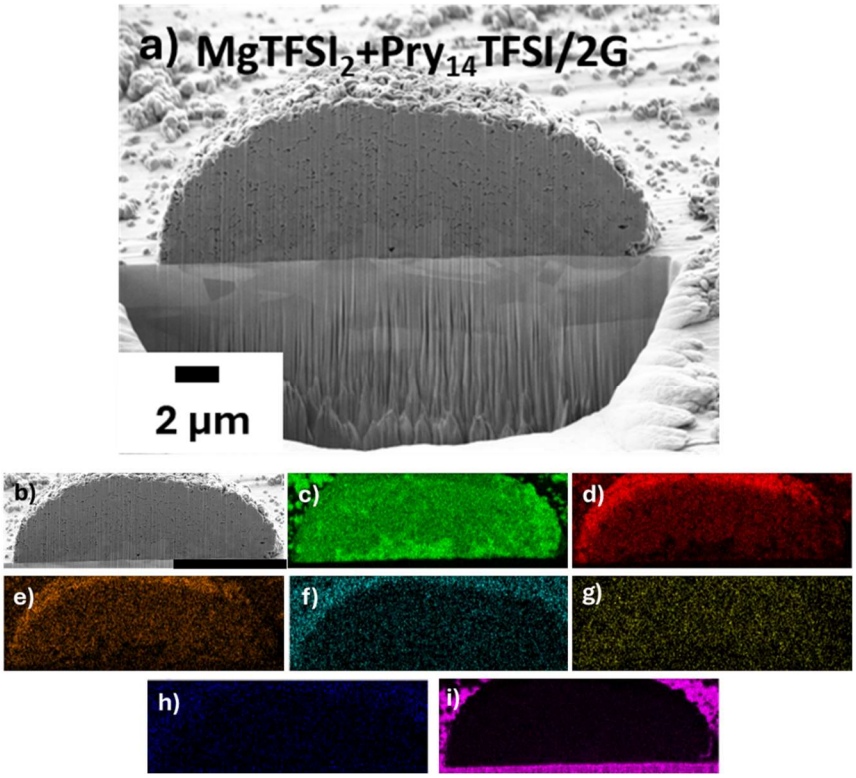

Figure 4.17, Cross sectional SEM images of (a and b) $MgTFSI_2$+$Pry_{14}TFSI$/2G, (c-i) EDX maps for (c) Mg, (d) O, (e) F, (f) C, (g) S, (h) N and (i) Cu. EDX maps all to the same scale as (b) which has a scale bar of 10 µm. All images are after 30 cycles between -0.7 and 0.8 V vs Mg^{2+}/Mg, at a scan rate of 100 mV s^{-1} and are on a Cu ribbon electrode and after discharge.

The cross sections for the $MgTFSI_2$+$Pry_{14}TFSI$/2G appear similar to those seen for the cross sections in Chapter 3, Figure 4.17a and b. The deposits have a high porosity throughout, spanning from the core through to the exterior of the structure. The EDX shows a core that is rich in only Mg, as shown in Figure 4.17c-i. Moving out from the rich Mg core, O and F increase in intensity as the intensity of Mg decreases. This implies that these deposits have a core rich with Mg metal, and moving out from this core, the structure consists of a mixture of MgO and MgF_2.

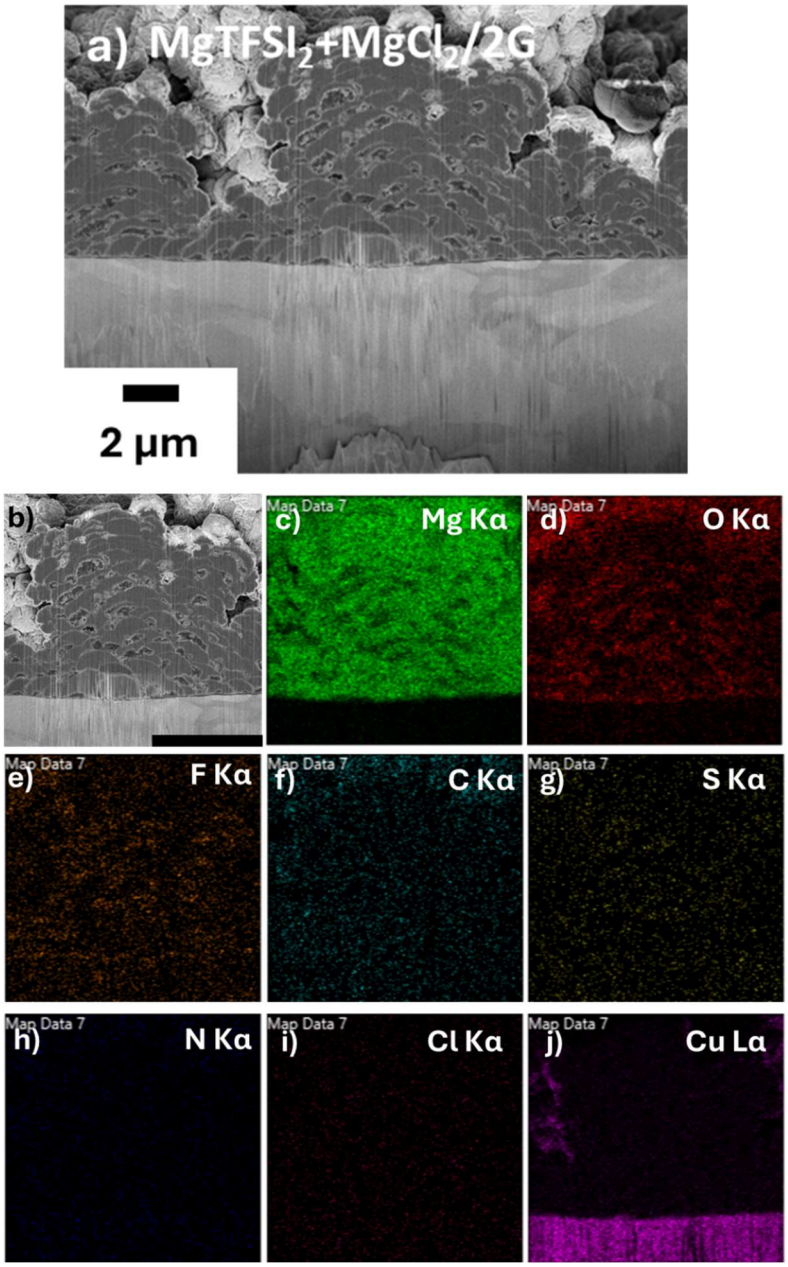

Figure 4.18, Cross sectional SEM images of (a and b) $MgTFSI_2$+$MgCl_2$/2G, (c-j) EDX maps for (c) Mg, (d) O, (e) F, (f) C, (g) S, (h) N, (i) Cl and (j) Cu. EDX maps all to the same scale as (b) which has a scale bar of 5 µm. All images are after 30 cycles between -0.7 and 0.8 V vs Mg^{2+}/Mg, at a scan rate of 100 mV s^{-1} and are on a Cu ribbon electrode and after discharge.

For the structure of the deposits formed in the $MgTFSI_2$+$MgCl_2$/2G electrolyte, the cross-sectioning confirms previously mentioned hypotheses about how the deposit structures form, Figure 4.18a and b. The cross-sectioning reveals that these structures form through the repeated deposition of small hemispherical

structures, one on top of another. This can be informed by the lighter arcs of contrast through the cross-section and the corresponding areas of higher O intensity on the EDX maps, Figure 4.18c-j.

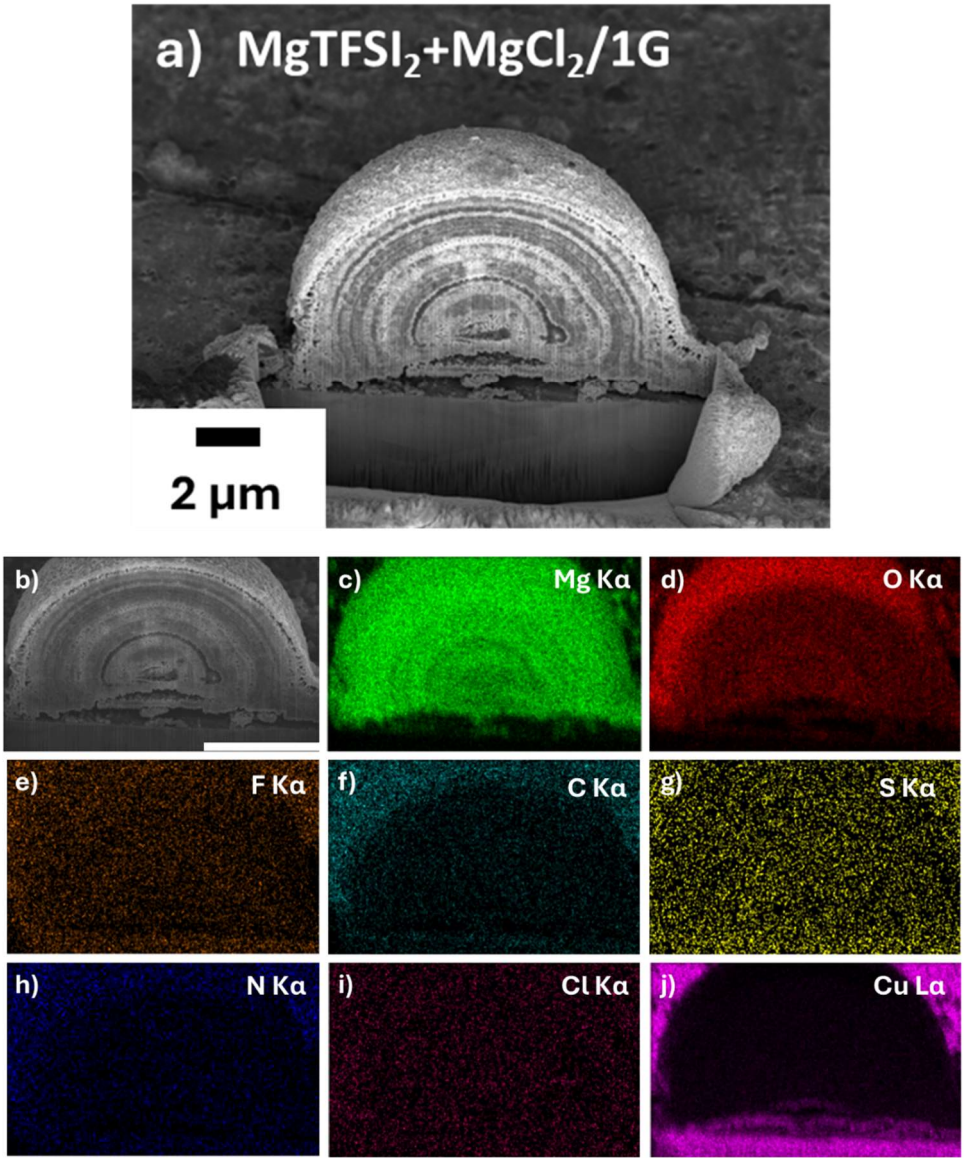

Figure 4.19, Cross sectional SEM images of (a and b) $MgTFSI_2$+$MgCl_2$/1G, (c-j) EDX maps for (c) Mg, (d) O, (e) F, (f) C, (g) S, (h) N, (i) Cl and (j) Cu. EDX maps all to the same scale as (b) which has a scale bar of 5 µm. All images are after 30 cycles between -0.7 and 0.8 V vs Mg^{2+}/Mg, at a scan rate of 100 mV s^{-1} and are on a Cu ribbon electrode and after discharge.

Another type of deposit structure is seen in the $MgTFSI_2$+$MgCl_2$/1G electrolyte. The milling of these structures reveals a layered structure, Figure 4.19a and b.These layers are concentric rings, like those seen in a tree or an

onion, and mainly constitute Mg, O, and F, Figure 4.19c-j, which is expected as after stripping, little Mg metal would be left in the structure. The cycling mechanism for this electrolyte system will be discussed in-depth in Chapter 5.

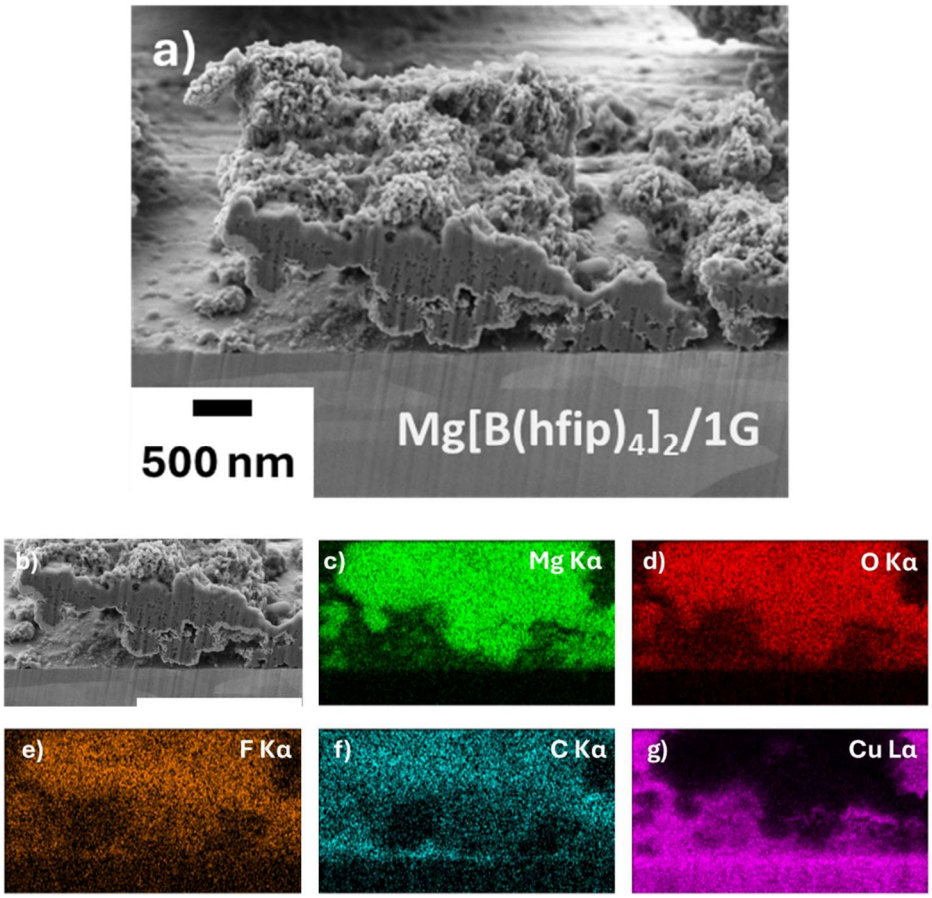

Figure 4.20, Cross sectional SEM images of (a and b) $Mg[B(hfip)_4]_2$/1G, (c-g) EDX maps for (c) Mg, (d) O, (e) F, (f) C, and (g) Cu. EDX maps all to the same scale as (b) which has a scale bar of 2 µm. All images are after 30 cycles between -0.7 and 0.8 V vs Mg^{2+}/Mg, at a scan rate of 100 mV s^{-1} and are on a Cu ribbon electrode and after discharge.

For the final electrolyte system $Mg[B(hfip)_4]_2$/1G, the deposit structures are much thinner than all the other structures, <1 µm, Figure 4.20a and b. The cross-section shows that the interior structure is highly porous, with the pores being nanometres in diameter. The EDX map of the cross-section reveals a high concentration of Mg, O and F, corresponding to MgO and MgF_2 from both the 1G and the borate salt, Figure 4,20c-g. Comparing between the SEM images of the cross-section charged and discharged deposits, along with the EQCM data

from earlier, help to give the likely cycling mechanism of the $Mg[B(hfip)_4]_2$/1G electrolyte.

Each of the electrolyte systems form different deposit structures from flat discs to hemispheres. The difference in structures is likely due to a combination of factors, such as the solvent coordination around Mg, with 2G coordinating to the Mg ion more than 1G. Also the addition of chloride to the electrolytes likely forms a stable SEI, meaning fewer potential nucleation sites. This could explain the sparseness in surface structures for the chloride containing systems. With regards to the structures formed in the borate containing electrolyte, borates often lead to more controlled and uniform deposition of Mg due to their less nucleophilic nature and ability to form stable ion complexes.[41]

From the EQCM and SEM data the cycling mechanism can be deduced. The EQCM measurements for the $Mg[B(hfip)_4]_2$/1G electrolyte show that after the first four cycles the stripping efficiency is 100 % meaning all plated Mg in the following cycles is removed. This implies that during these initial cycles a stable structure for Mg to plate and strip on to forms. The SEM images of the discharged deposits show a thin highly porous layer <1 µm, Figure 4.21a, which when correlating to the EQCM data would imply that this is the layer that forms during the first few cycles which allows for the subsequent cycles to have a stripping efficiency of 100 %. Then when looking at cross sectioned images of the charged deposits, Figure 4.21b, there is a thick deposit of Mg on top of the porous structure seen in the discharged deposit. This implies that the cycling mechanism occurs through the initial formation of a stable Mg surface structure over the first few cycles, after which Mg can be reversibly plated and stripped from that structure with 100 % efficiency.

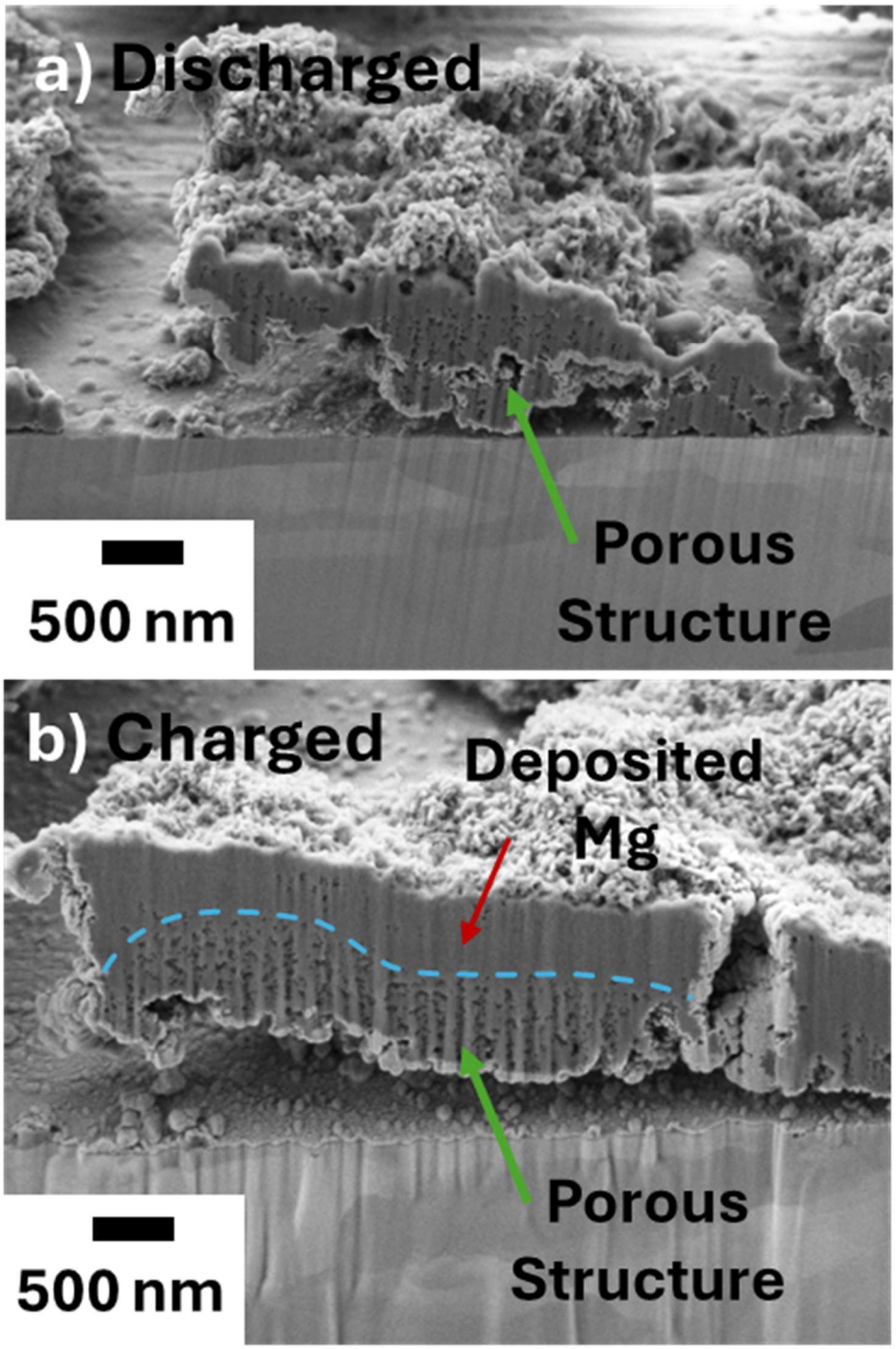

Figure 4.21, Cross sectional SEM images of $Mg[B(hfip)_4]_2$/1G after (a) discharge and (b) charge. All images are after 30 cycles and are on a Cu ribbon electrode, with the porous structure and deposited Mg labelled and separated by the blue dashed line.

4.3 Conclusions

Direct comparison of different electrolyte systems using the same techniques has shown that they can vary greatly with respect to their electrochemistry and surface deposits. The cyclic voltammetry measurements have shown that adding additives or changing the solvent used can have a large impact on the efficiency; adding $MgCl_2$ increases the efficiency by 30 %, and changing the glyme length from 2G to 1G improves the efficiency further by 4%. This all culminates in getting closer to the ideal 99.99 % efficiency desired by battery development.

The EQCM measurements helped show that even if the CE is relatively poor compared to the CVs in another cell, the stripping efficiency can be relatively higher, for instance, with the $Mg[B(hfip)_4]_2$/1G. These measurements also showed a correlation between the improvement in efficiency during the initial cycles and conditioning, which is linked to an improvement in stripping efficiency, showing that the conditioning process helps the CE and the stripping efficiency.

The microscopy analysis showed how even a slight change in electrolyte composition can have a large impact on the electrode morphology. The addition of 10 mM $Pry_{14}TFSI$ changed the surface structures from flat disc structures to porous hemispheres, and changing solvents also affected the finer surface structures of these deposits.

Comparing the different electrolyte systems from this section shows that the $Mg[B(hfip)_4]_2$/1G and $MgTFSI_2$+$MgCl_2$/1G systems perform the best. This is due to their high CE, 96 and 95 %, respectively, and their high Mg stripping efficiency on the electrode surface. They both still show electrolyte degradation, due to the surface structure left on the electrode, but not as much as the other systems tested. This is likely due to them forming stable SEI layers early on in their cycling which is stable through the following cycles. The $MgTFSI_2$+$MgCl_2$/1G system will be investigated further using the methodology developed in Chapter 3 in the following chapter.

4.4 Experimental

4.4.1 Chemicals

Diglyme (2G) (~300 – 400 mL) (Sigma Aldrich, $\geq$ 99.9 %) was distilled under vacuum over sodium (0.7 g) (Sigma Aldrich, 99 %) and benzophenone (4 g) (Sigma Aldrich, 99 %). The distilled 2G was stored in a N_2 glovebox and was dried using 4 Å molecular sieves (Sigma Aldrich) for 3 days. $Mg(TFSI)_2$ (Solvionic, 99.5 %) was dried under vacuum at 120 °C for 3 days and stored in an N_2 glovebox. Dimethoxy ethane (DME) (Sigma Aldrich, 99 %), magnesium chloride ($MgCl_2$) (Sigma Aldrich, 99.9 %), sodium borohydride ($NaBH_4$) (Sigma Aldrich, 99.5 %), butyl-methylpyrrolidinium bis(trifluoromethanesulfonyl)imide ($Pry_{14}TFSI$) (Sigma Aldrich, 99.9 %), hexafluoroisopropanol (HFIP) (Sigma Aldrich, 99.9 %), 1 M dibutyl magnesium ($MgBu_2$) in hexane (Sigma Aldrich, 99.9 %) and 2 M trimethyl aluminium ($AlMe_3$) (Sigma Aldrich, 99.9 %) were all used as supplied and stored in a N_2 glovebox (O_2 <0.1 ppm, H_2O < 0.1 ppm)

4.4.2 Synthesis of $MgBH_4$

$MgCl_2$ (12.78 g, 0.13 mol) and $NaBH_4$ (10.16 g, 0.26 mol) were milled in a Fritsch P6 Planetary ball mill at 400 rpm for 12 hr (ZrO_2 grinding bowl and balls), grinding bowl was sealed in a glovebox. Approximately 3 g of the resulting powder was transferred to a two-neck round bottom flask and dissolved in diethyl ether (200 ml) inside a glovebox. The suspension was then transferred to a Schlenk line before being stirred for 24 hrs under reflux. The mixture was filtered through canular filtration, and the solvent was removed from the filtrate under vacuum. The remaining powder was heated at 190 °C for 1 hr under vacuum before being transferred to a glovebox and then 180 °C for 2 hrs in a Buchi oven under vacuum. The yield ranged from 43 – 67 % and was a fine white powder1H NMR (400 MHz, THF) δ 3.63 (s, 0H), 3.40 (q, J = 7.0 Hz, 0H), 1.76 (s, 0H), 0.15 – -0.77 (m, 1H). 11B NMR (128 MHz, THF) δ -40.10 (p, J = 82.3 Hz).

4.4.3 Synthesis of $Mg[B(hfip)_4]_2$

Synthesised $MgBH_4$ (0.81 g, 15 mM) was dissolved in 30 mL of DME in a two-necked round bottom flask inside a glovebox. This flask was then sealed and

connected to a Schlenk line before HFIP (20.5 g, 12.9 mL, 123 mM) was added dropwise throughout 1 hr, and the resulting solution was stirred for 24 hrs. The resulting mixture was refluxed at 85 °C for a further 2 hours. After cooling, the solvent was removed under vacuum. The resulting powder was then dried further under a vacuum for 24 hours. This gave a fine white powder with a yield of 70 %. ^{1}H NMR (400 MHz, THF) δ 4.76 (br, 1H), 3.61 (s, 1H), 3.46 (d, *J* = 1.3 Hz, 1H), 3.31 (d, *J* = 1.3 Hz, 1H), 1.76 (s, 1H). ^{11}B NMR (128 MHz, THF) δ 1.67. 19F NMR (376 MHz, THF) δ -75.38.

4.4.4 Synthesis of $Mg[Al(hfip)_4]_2$

HFIP (3.44 g, 2.2 mL, 20.5 mmol) was dissolved in 30 mL of DME in a glovebox. Then 10 mL of 1 M dibutyl magnesium ($MgBu_2$) in hexane was slowly added dropwise to the HFIP solution and left to stir for 6 hrs at room temperature. A solution of 2 M trimethyl aluminium ($AlMe_3$) in toluene was added. Further, HFIP (12.04 g, 7.6 mL, 70.7 mmol) was added gradually over 1 hr and further stirred for 24 hrs. The solution was concentrated to ~ 15 mL by solvent evaporation before being added slowly dropwise to 150 mL of hexane. This mixture formed two layers; the top hexane layer was then removed by a syringe and vacuumed before the remaining layer was dried under a vacuum for 24 hours, giving a viscous gel. ^{1}H NMR (400 MHz, DMSO) δ 4.68 – 4.57 (m, 1H), 3.43 (s, 2H), 3.24 (s, 3H). ^{19}F NMR (376 MHz, DMSO) δ -76.13 (d, *J* = 6.4 Hz), -76.26 – -76.37 (m).

4.4.5 NMR spectroscopy

NMR solutions were prepared by dissolving 10 mg or 10 µL of a compound or mixture in 0.75 mL of deuterated dimethyl sulfoxide (DMSO) or tetrahydrofuran (THF).^{1}H, ^{11}B and ^{19}F NMR were recorded on a Bruker Ascended 400 MHz spectrometer using 16, 256 and 64 scans respectively

4.4.6 Electrolyte preparation

The electrolytes were made by dissolving the desired amount of salt into the desired solvent and left to stir overnight until colourless. After which 4 Å molecular sieves were added, and the electrolyte was then left to dry for a week. The following electrolytes were prepared:

1. 0.5 M $Mg(TFSI)_2$ in 2G
2. 0.5 M $Mg(TFSI)_2$ and 10 mM $Pry_{14}TFSI$ in 2G
3. 0.25 M $Mg(TFSI)_2$ and 0.125 M $MgCl_2$ in 2G
4. 0.4 M $Mg[Al(hfip)_4]_2$ in 2G
5. 0.125 M $Mg(TFSI)_2$ and 0.25 M $MgCl_2$ in 1G
6. 0.3 M $Mg[B(hfip)_4]_2$ in 1G

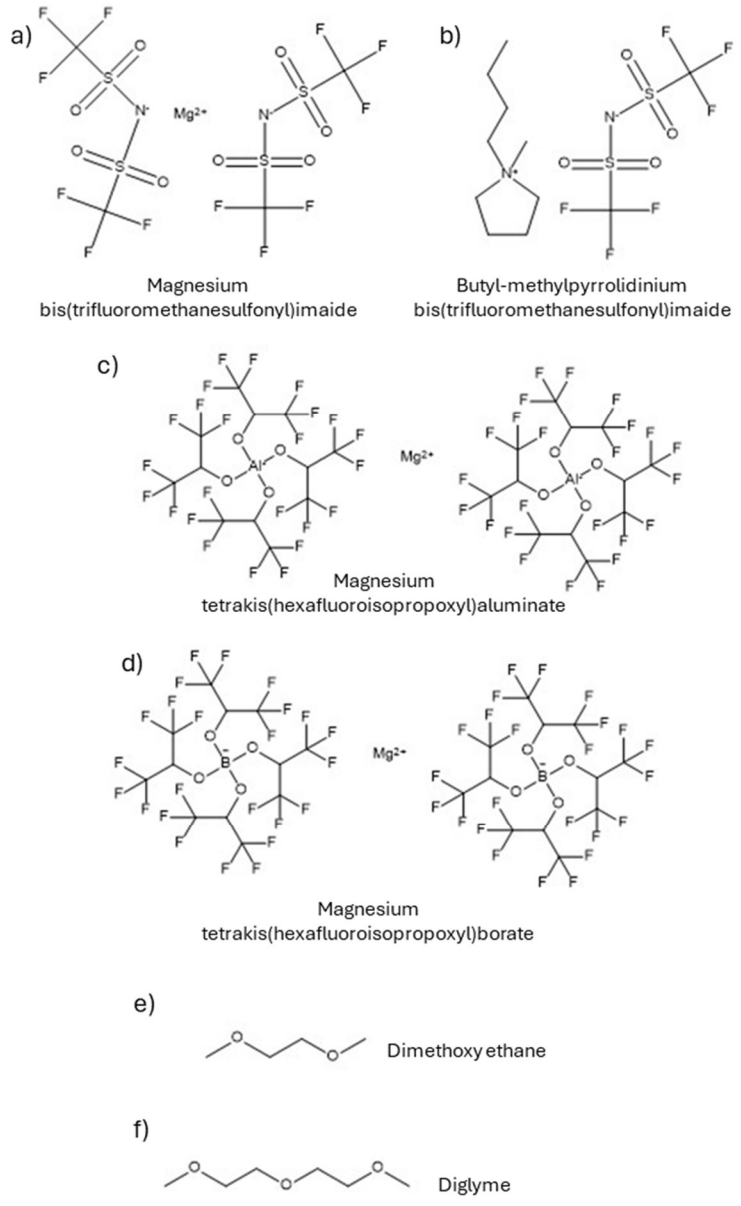

Figure 4.E, Chemical structures of (a) magnesium bis(trifluoromethanesulfonyl)imide, (b) butyl-methyl-pyrrolidinium bis(trifluoromethanesulfonyl)imide, (c) magnesium tetrakis(hexafluoisopropoxy)aluminate, (d) magnesium tetrakis(hexafluoisopropoxy)borate, (e) dimethoxy ethane and (f) diglyme.

4.4.7 Electrochemical experiments

All electrochemical experiments were performed inside an N_2 glovebox. Before use, all glassware was cleaned and dried overnight at 70 °C under vacuum. Cyclic voltammetry and galvanostatic measurements were recorded on a Biologic SP-300 potentiostat using three electrodes: a Cu ribbon (Sigma-Aldrich) working electrode and an Mg ribbon (Sigma-Aldrich) counter and reference. The Mg ribbons were scratched beforehand to remove the oxidised layer and reveal the fresh Mg surface. The copper foil was cut into ribbons and dried at 120 °C under vacuum before being stored in the glove box.

EQCM experiments were performed with a CHI 450 potentiostat. The working electrode was either a gold or copper EQCM crystal (CH Instruments, United States of America) inside a PTFE cell, the diagram in Figure 2.1b.

4.4.8 Surface characterisation

Before surface characterisation, the cycled Cu electrodes were washed with DME (Sigma-Aldrich, purity 99.5%) (dried using 4 Å molecular sieves) and dried under vacuum for 30 minutes in a glovebox mini-antechamber. For transferring samples into the Zeiss Crossbeam 550 FIB-SEM (Carl Zeiss, Germany), the samples were loaded air-free from the glovebox using a Quorum PP3006 CoolLok Transfer port mounted directly onto the glovebox. The sample was transferred to a Quorum PP3010 FIB/SEM Preparation system before being loaded into the SEM chamber. SEM images were taken at an accelerating voltage of 2 kV. A Ga ion FIB source was used for milling the sample at an accelerating voltage of 30 kV with FIB currents between 50 and 700 pA. EDX analysis was performed with an Oxford Instruments Ultimax 170 X-ray microanalysis detector (Oxford Instruments, UK) and analysed using Aztec software (v 4.3) at an accelerating voltage of 5 kV. The 3D structures, cross sections and deposit volumes were generated using Dragonfly software (v 2021.3 for Windows).

4.5 References

1 Y. Man, P. Jaumaux, Y. Xu, Y. Fei, X. Mo, G. Wang and X. Zhou, *Science Bulletin*, 2023, **68**, 1819–1842.

2 M. Fichtner, *Magnesium Batteries: Research and Applications*, Royal Society of Chemistry, 2019, vol. 2020.

3 L. Luo, X. Yang, Z. Gao, X. Li, J. Xu, Y. Zhang, R. Deng, G. Huang, J. Wang and F. Pan, *Electrochimica Acta*, 2024, **478**, 143815.

4 K. Xu, *Commun Mater*, 2022, **3**, 31.

5 A. K. Stephan, *Joule*, 2021, **5**, 1–2.

6 Y.-K. Sun, *ACS Energy Lett.*, 2021, **6**, 2187–2189.

7 R. Attias, B. Dlugatch, O. Blumen, K. Shwartsman, M. Salama, N. Shpigel and D. Sharon, *ACS Appl. Mater. Interfaces*, 2022, acsami.2c08008.

8 D. Aurbach, M. Moshkovich, A. Schechter and R. Turgeman, *Electrochemical and Solid-State Letters*, 2000, **3**, 31–34.

9 M. Biermann, C. Leppin, A. Langhoff, T. Ziemer, C. Rembe and D. Johannsmann, *Analyst*, 2024, **149**, 2138–2146.

10 B. W. Schick, X. Hou, V. Vanoppen, M. Uhl, M. Kruck, E. J. Berg and T. Jacob, *ChemSusChem*, 2023, e202301269.

11 S. Fan, S. Cora and N. Sa, *ACS Appl. Mater. Interfaces*, 2022, acsami.2c13037.

12 K. D. Ralston, S. Thomas, G. Williams and N. Birbilis, *Applied Surface Science*, 2016, **360**, 342–348.

13 R. Xu, X. Gao, Y. Chen, C. Peng, Z. Zhang, C. Wang, H. Sun, X. Chen and L. Cui, *Materials Today Physics*, 2023, **36**, 101186.

14 D. Aurbach, Z. Lu, A. Schechter, Y. Gofer, H. Gizbar, R. Turgeman, Y. Cohen, M. Moshkovich and E. Levi, *Nature*, 2000, **407**, 724–727.

15 I. Shterenberg, M. Salama, H. D. Yoo, Y. Gofer, J.-B. Park, Y.-K. Sun and D. Aurbach, *Journal of The Electrochemical Society*, 2015, **162**, A7118–A7128.

16 C. J. Barile, E. C. Barile, K. R. Zavadil, R. G. Nuzzo and A. A. Gewirth, *The Journal of Physical Chemistry C*, 2014, **118**, 27623–27630.

17 T. Mandai, *ACS Appl. Mater. Interfaces*, 2020, **12**, 39135–39144.

18 T. Pavčnik, M. Lozinšek, K. Pirnat, A. Vizintin, T. Mandai, D. Aurbach, R. Dominko and J. Bitenc, *ACS Appl. Mater. Interfaces*, 2022, **14**, 26766–26774.

19 J. Wang, W. Zhao, H. Dou, B. Wan, Y. Zhang, W. Li, X. Zhao and X. Yang, *ACS Applied Materials and Interfaces*, 2020, **12**, 19601–19606.

20 S. B. Son, T. Gao, S. P. Harvey, K. X. Steirer, A. Stokes, A. Norman, C. Wang, A. Cresce, K. Xu and C. Ban, *Nature Chemistry*, 2018, **10**, 532–539.

21 Y. Zhang, J. Li, W. Zhao, H. Dou, X. Zhao, Y. Liu, B. Zhang and X. Yang, *ADVANCED MATERIALS*, 2022, **34**, e2108114.

22 Z. Meng, Z. Li, L. Wang, T. Diemant, D. Bosubabu, Y. Tang, R. Berthelot, Z. Zhao-Karger and M. Fichtner, *ACS Appl. Mater. Interfaces*, 2021, **13**, 37044–37051.

23 K. Tang, A. Du, S. Dong, Z. Cui, X. Liu, C. Lu, J. Zhao, X. Zhou and G. Cui, *Advanced Materials*, 2020, **32**, 1904987.

24 T. Chen, G. Ceder, G. S. Gautam and P. Canepa, *Frontiers in Chemistry*, 2019, **7**, 1–10.

25 R. Mohtadi, M. Matsui, T. S. Arthur and S. J. Hwang, *Angewandte Chemie International Edition*, 2012, **51**, 9780–9783.

26 J. T. Herb, C. A. Nist-Lund and C. B. Arnold, *ACS Energy Lett.*, 2016, **1**, 1227–1232.

27 T. Ruman, A. Kuśnierz, A. Jurkiewicz, A. Leś and W. Rode, *Inorganic Chemistry Communications*, 2007, **10**, 1074–1078.

28 D.-T. Nguyen, A. Y. S. Eng, R. Horia, Z. Sofer, A. D. Handoko, M.-F. Ng and Z. W. Seh, *Energy Storage Materials*, 2022, **45**, 1120–1132.

29 Z. Hu, L. Huang, X. Gan, Y. Han, J. Chu and Z. Song, *ACS Appl. Mater. Interfaces*, 2024, acsami.4c02399.

30 T. Pavčnik, J. Imperl, M. Kolar, R. Dominko and J. Bitenc, *J. Mater. Chem. A*, 2024, **12**, 3386–3397.

31 K. B. Hatzell, *ACS Energy Lett.*, 2023, **8**, 4775–4776.

32 S. H. Park, D. Jun, G. H. Lee, S. G. Lee and Y. J. Lee, *J. Mater. Chem. A*, 2021, **9**, 14656–14681.

33 N. Sa, B. Pan, A. Saha-Shah, A. A. Hubaud, J. T. Vaughey, L. A. Baker, C. Liao and A. K. Burrell, *ACS Applied Materials & Interfaces*, 2016, **8**, 16002–16008.

34 C. Holc, K. Dimogiannis, E. Hopkinson and L. R. Johnson, *ACS Appl. Mater. Interfaces*, 2021, **13**, 29708–29713.

35 Y. Shao, T. Liu, G. Li, M. Gu, Z. Nie, M. Engelhard, J. Xiao, D. Lv, C. Wang, J. G. Zhang and J. Liu, *Scientific Reports*, 2013, **3**, 4–10.

36 T. Mandai, Y. Youn and Y. Tateyama, *Mater. Adv.*, 2021, **2**, 6283–6296.

37 B. Dlugatch, M. Mohankumar, R. Attias, B. M. Krishna, Y. Elias, Y. Gofer, D. Zitoun and D. Aurbach, *ACS Applied Materials & Interfaces*, DOI:10.1021/acsami.1c13419.

38 R. S. Patil, V. A. Juvekar and V. M. Naik, *Ind. Eng. Chem. Res.*, 2011, **50**, 12946–12959.

39 S. E. Waters, B. H. Robb and M. P. Marshak, *ACS Energy Lett.*, 2020, **5**, 1758–1762.

40 N. Elgrishi, K. J. Rountree, B. D. McCarthy, E. S. Rountree, T. T. Eisenhart and J. L. Dempsey, *Journal of Chemical Education*, 2018, **95**, 197–206.

41 A. Du, Z. Zhang, H. Qu, Z. Cui, L. Qiao, L. Wang, J. Chai, T. Lu, S. Dong, T. Dong, H. Xu, X. Zhou and G. Cui, *Energy Environ. Sci.*, 2017, **10**, 2616–2625.

Chapter 5: Structural and chemical composition of the Mg electrode in a chloride glyme electrolyte

5.1 Background

Chloride-containing electrolytes have shown promise in overcoming the inherent challenges of Mg metal deposition by improving Mg-ion solubility and facilitating a more reversible Mg plating and stripping process. However, these electrolytes are also prone to instability and side reactions, which lead to passivation layers on the anode surface, ultimately limiting the battery's electrochemical performance.[1]

Despite the improved deposition behaviour observed with chloride-containing electrolytes, challenges remain in controlling side reactions and managing the formation of surface passivation layers, particularly magnesium oxide (MgO) and magnesium fluoride (MgF_2).[2] These products, formed during reactions with the electrolyte, reduce the reversibility of Mg deposition and lead to increased resistance at the anode surface, impairing overall battery performance.[3]

As shown in the previous chapters, the structures that form on the electrode surface can possess complex chemical and structural properties.[4] For chloride-containing systems, the degradation of electrolytes, forming MgO and MgF_2 primarily, causes onion-like structures on the electrode surface through cycling. The work so far, however, does not show the role that Cl plays in the cycling mechanism, as the EDX maps show a small amount with little arrangement in distribution.

This chapter aims to further investigate the morphology and chemical composition of the Mg deposits that form in the $MgCl_2$-containing electrolyte using advanced characterisation techniques, including TEM, EDX, SEM, and XPS. It will also look at how different cycling conditions affect the efficiency of cycling through surface passivation. This work will show how the surface chemistry evolves through cycling along with the nano structure of the deposits which form with a nanometre thick organic interphase.

5.2 Results and Discussion

5.2.1 Chemical evolution of the Cu electrode surface

The cyclic voltammetry in Figure 5.1a is the same as shown in the previous chapter for the 0.25 M $MgCl_2$ and 0.125 $Mg(TFSI)_2$ in 1G electrolyte system. As stated previously, the CVs show little change over the 30 cycles, with a slight increase and then a decrease in peak current. During this, it maintains a high coulombic efficiency of 95 % over the 30 cycles, with no increase over the first few cycles due to any conditioning process or decrease in later cycles due to an unstable interphase.

With these measurements, the cycling time is relatively quick and might mask any degradation. Running measurements at lower scan rates will allow for analysis of these processes, as batteries can be charged and discharged over long periods. When varying the CVs' scan rate, the coulombic efficiency varies (Figure 5.1b) it is poor, about 25 % at 1 mV s^{-1}, whereas at higher scan rates and is almost 100 %, 98 % at 400 mV s^{-1}. This variation in coulombic efficiency with scan rate shows that in short experimental times, with higher scan rates, the Mg could be oxidised more reversibly due to less time to react with the electrolyte. Whereas at longer experimental times and slower scan rates, the oxidation of Mg cannot be fully reversibly oxidised as there is more time for the plated Mg metal to react with and degrade the electrolyte.

This is also observed when, in measurements where a potential of 0 V vs Mg^{2+}/Mg was held for difference lengths of time before another CV is measured, Figure 5.1c. This plot shows that increasing rest times between measurements increases the overpotential at which plating occurs, indicating a surface interphase that is harder for Mg to diffuse through to plate or that the surface has been passivated through reactions between Mg and the electrolyte.

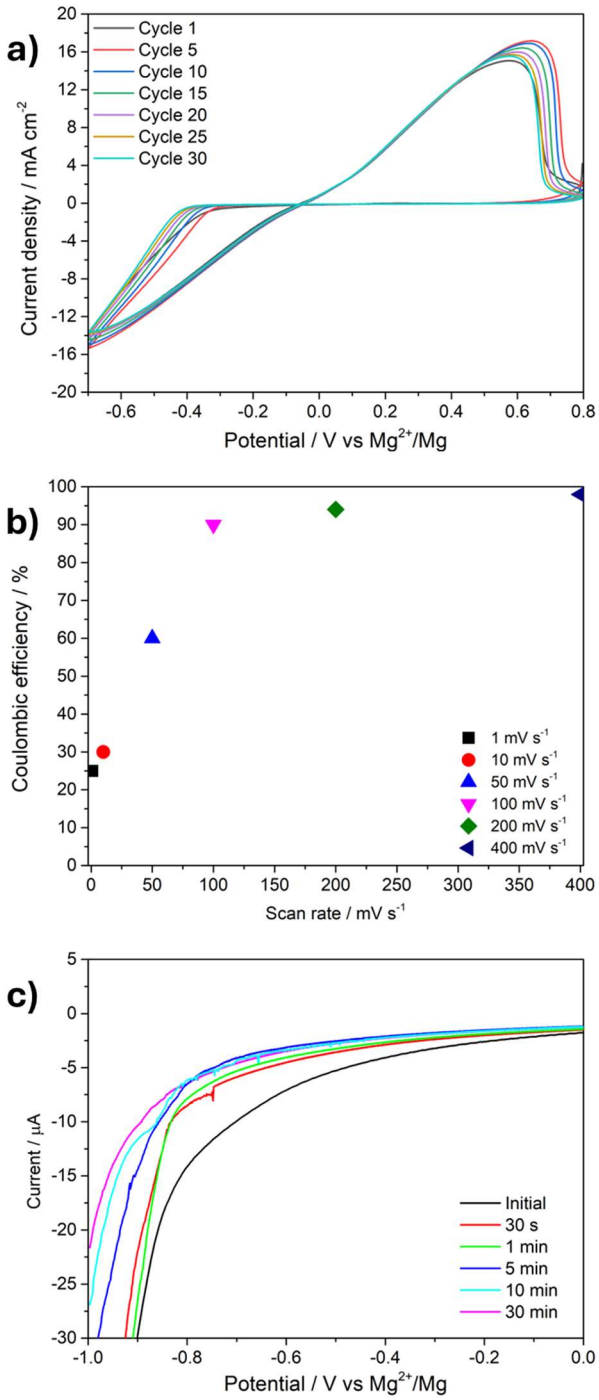

Figure 5.1, (a) Cyclic voltammetry of 0.25 M $MgCl_2$ and 0.125 M $Mg(TFSI)_2$ in 1G for 30 cycles, (b) coulombic efficiency average of 30 CV cycles at different scan rates and (c) linear sweep voltammograms following different lengths of potential hold at 0 V vs Mg^{2+}/Mg. All CVs and LSVs were recorded at a Cu working electrode with a Mg counter and reference and at a scan rate of 100 mV s^{-1} over 30 cycles.

To develop an understanding of the chemical composition of the interphase, XPS was employed to characterise the surface of a Cu electrode after 10 and

30 cycles, Figure 5.2, the complete XPS spectra for both samples are shown in Figure 5.2i and j. The C 1s spectra recorded after 10 and 30 cycles both show the presence of C-C (248.8 eV), C-O (287.0 eV), C=O (288.7 eV), O-C=O (290.7 eV) and C-F_x (294.5 eV) environments, Figure 5.2a and e. These environments are formed from the degradation of both the 1G and $Mg(TFSI)_2$ present during cycling.

The F 1s spectra for both samples show the presence of 2 different F 1s environments, those being C-F (690.3 eV) and MgF_2 (687.2 eV), Figure 5.2b and f, both of which are due to decomposition of the $TFSI^-$ anion. Comparing the relative areas of both peaks present in the F 1s spectra can indicate how the interphase is evolving over time. The ratio of C-F to MgF_2 after 10 cycles is 56.8:43.2, indicating a predominately organic interphase layer. Whereas after 30 cycles, that ratio changes to 38.9:61.1, which shows that the interphase becomes more inorganic through progressive cycling, showing continuous decomposition of TFIS. The ratios of all the peaks present in the XPS are shown in Table 5.1.

The Mg 2p spectra show 3 different environments present, MgF_2 (52.2 eV), MgO/MgS (50.9 eV) and Mg metal (49.6 eV), Figure 5.2c and g. Between cycle 10 and cycle 30 there is a significant change in the relative amounts of each Mg 2p environment. For cycle 10, the ratio of MgF_2 to MgO/S to Mg metal is 49.1:23.1:27.7 respectively, and after 30 cycles, the ratio is 79:19.8:1.2 respectively. The significant decrease in the relative amount of Mg metal present at the surface of the deposits isn't surprising, as seen in the EQCM earlier, and later, the efficiency of Mg stripping reaches 100 %, so there would be very little Mg metal left at the surface as most of it is stripped on oxidation.

Comparing the environments in the S 2p spectra shows a similar trend to the F 1s spectra, Figure 5.2d and h. The environments in the S 2p spectra are for S=O (169.3 eV) and MgS (164.0 eV). During consecutive cycling the ratio between these peaks' changes from 73.9:26.1 for S=O:MgS at 10 cycles to 27.3:72.7 at 30 cycles, which shows the surface is becoming more inorganic through progressive cycles.

Table 5.1, The percentage composition of the different environments presents in the F 1s, Mg 2p, S 2p and C 1s spectra shown in Figure 5.2.

XPS spectrum	XPS peak	Composition after 10 cycles (%)	Composition after 30 cycles (%)
F 1s	C-F	56.8	38.9
	MgF_2	43.2	61.1
Mg 2p	MgF_2	49.1	79.0
	MgO/S	23.1	19.8
	Mg metal	27.7	1.2
S 2p	MgS	26.1	72.7
	S=O	73.9	27.3
C 1s	C-C	20.7	21.6
	C-O	58.2	58.4
	C=O	12.7	7.6
	O-C=O	6.7	10.8
	$C\text{-}F_X$	1.7	1.6

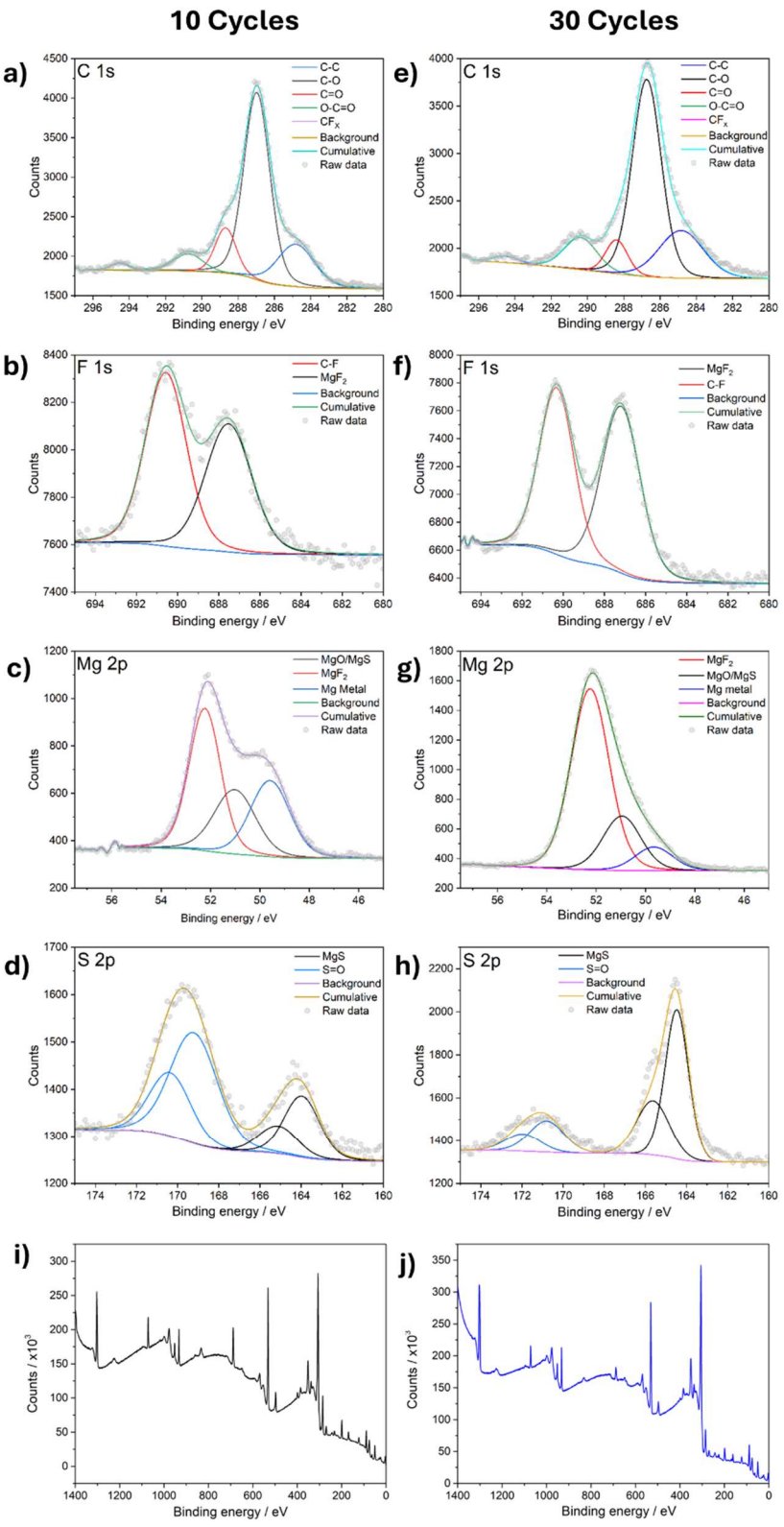

Figure 5.2, XPS spectra of C 1s, F 1s, Mg 2p and S 2p on a Cu electrode surface (a-d) after 10 cycles and (e-h) after 30 cycles, respectively and XPS wide scans for (i) 10 scans and (j) 30 scans. The conditions for cycling were the same as those in Figure 5.1a, stopped at 0.8 V vs Mg^{2+}/Mg.

Although CVs are helpful in showing how efficiently Mg is plated and stripped from the electrode surface, they are not representative of how an actual Mg electrode would perform during cell cycling. So galvanostatic cycling was performed to see how the efficiency of the electrolyte system performs under cell conditions for short- and long-term cycling, Figure 5.3. The standard cell cycling profile, shown in Figure 5.3a, where the cell is charged/discharged at 1 mA cm^{-2}, which both last for 30 mins, or until the potential limit of 0.8V vs Mg^{2+}/Mg is reached. Cycling starts with the charging process, where Mg is deposited onto the electrode surface. All electrolyte systems were conditioned before cycling as previous work showed this greatly improved efficiency; this involved 30 CV cycles, as shown in Figure 5.1a.[4] This process starts with an overpotential spike (-0.21 V vs. Mg^{2+}/Mg) before levelling at -0.16 V vs. Mg^{2+}/Mg and dipping slightly at the end of the charge.

During the discharge process, a plateau is observed at 0.02 V vs Mg^{2+}/Mg, but as the discharge process continues, the potential gradually increases to 0.09 V Mg^{2+}/Mg and then suddenly increases until the potential limit of 0.8 V vs Mg^{2+}/Mg is reached. This limit is reached before the end of the 30-minute discharge time, meaning the coulombic efficiency is less than 100 %, which is also shown in the CVs for longer experiment times. This increase in potential towards the potential limit is likely caused by the depletion of Mg metal from the electrode surface. This is due to some of the deposited Mg being passivated from electrolyte degradation products which either form passivating films or byproducts such as MgO, MgS and MgF_2, which can't be electrochemically oxidised back to Mg^{2+} in this potential window. The extended cycling with the above parameters is shown in Figure 5.3 b. It's observed that after the first few cycles, the plateau for charge decreases to -0.08 V Mg^{2+}/Mg, indicating that the plating of Mg metal onto the surface becomes easier whilst still having the initial potential spike of -0.21 V Mg^{2+}/Mg at the start of each charge process. However, as cycling continues, the potential of both the charge and discharge increase to -0.23 V and 0.146 V vs Mg^{2+}/Mg, respectively. This indicates that through extended cycling, resistance increases, meaning that higher potentials

are needed to drive the processes of Mg plating and stripping. This increase in resistance can be caused by the growth of a passivating layer on the electrode surface, formed from electrolyte degradation products forming a film which impedes ion transport through to the electrode.[5,6] The coulombic efficiency for this cycling is shown in Figure 5.3c and shows that over the 50 cycles, the average efficiency is 95 %.

To understand if the lack of stability in the interphase over long cycling is the cause of the decreased efficiency, more cycling was done with the same current density but with much shorter charge-discharge times, 12 mins each, Figure 5.3d. This data shows that the potential of the plateaus for charge and discharge are maintained much longer, -0.18 and 0.02 V vs Mg^{2+}/Mg, respectively, for the full 100 cycles. After 60 cycles, the potential during discharge starts to reach the potential limit of 1 V vs Mg^{2+}/Mg, whereas for the 30-minute charge-discharge cycling, that limit was reached in the first cycle. This reaching of the limit also brings down the coulombic efficiency, as seen before, Figure 5.3e, causing the cell to have an average efficiency of 97 %, with the first 60 cycles having an efficiency of 100 %. These measurements confirm the observations seen in the coulombic efficiency data with varying scan rates, that the shorter/faster the cycling, the higher the efficiency.

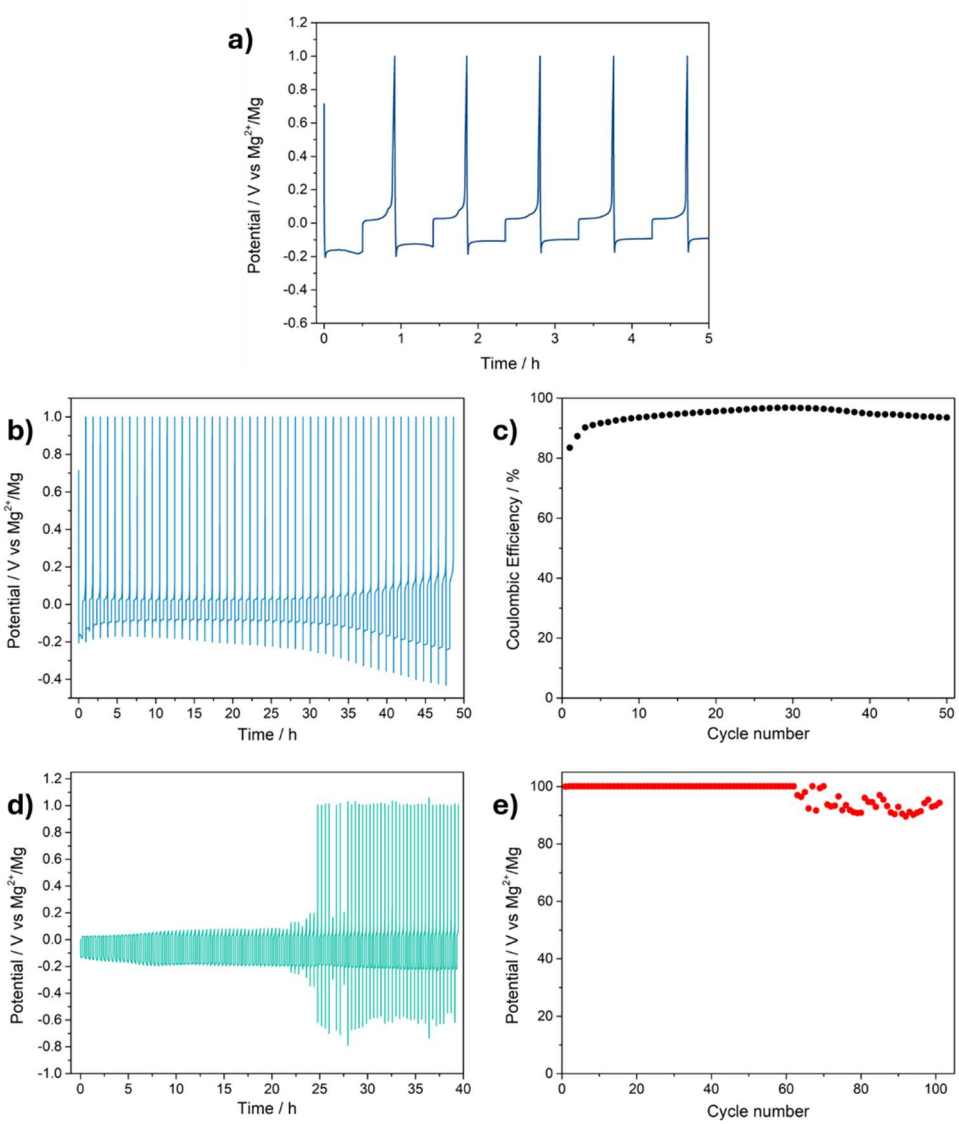

Figure 5.3, Galvanostatic cycling (a) showing the typical shape for cycling of Mg plating and stripping, (b) extended cycling over 50 cycles, with 30 min charge and discharge, and (c) the coulombic efficiency for the cycling shown in (b). (d) galvanostatic cycling over 100 cycles, with 12 min charge and discharge and (e) the respective coulombic efficiency plot. All galvanostatic cycling was done at a current density of 1 mA cm^{-2} on a Cu electrode with a Mg counter and reference electrode using the 0.25 M $MgCl_2$ and 0.125 M $Mg(TFSI)_2$ in 1G electrolyte.

After finishing the galvanostatic measurement, the electrodes are typically black and covered in deposited material, and Figure 5.4 shows the surface morphologies on the electrode surface. These images are from the electrode cycling shown in Figure 5.3b. At low magnifications, SEM images, Figure 5.4 a and b, show a thick layer of Mg which at higher magnification is made up of disc-like structures, Figure 5.4c and d, and spanning between this disc is a carbon film. These disc structures aren't the only morphologies seen on the electrode surface; there is also a highly porous structure, almost petal like morphology observed too, Figure 5.4e-g. When cross-sectioning these structures, Figure 5.4h, the contrast is lighter in the centre of the deposit; this previously indicated more Mg metal than MgO in Chapter 3, which is likely true here as well. This means the structure also contains shard-like structures throughout.

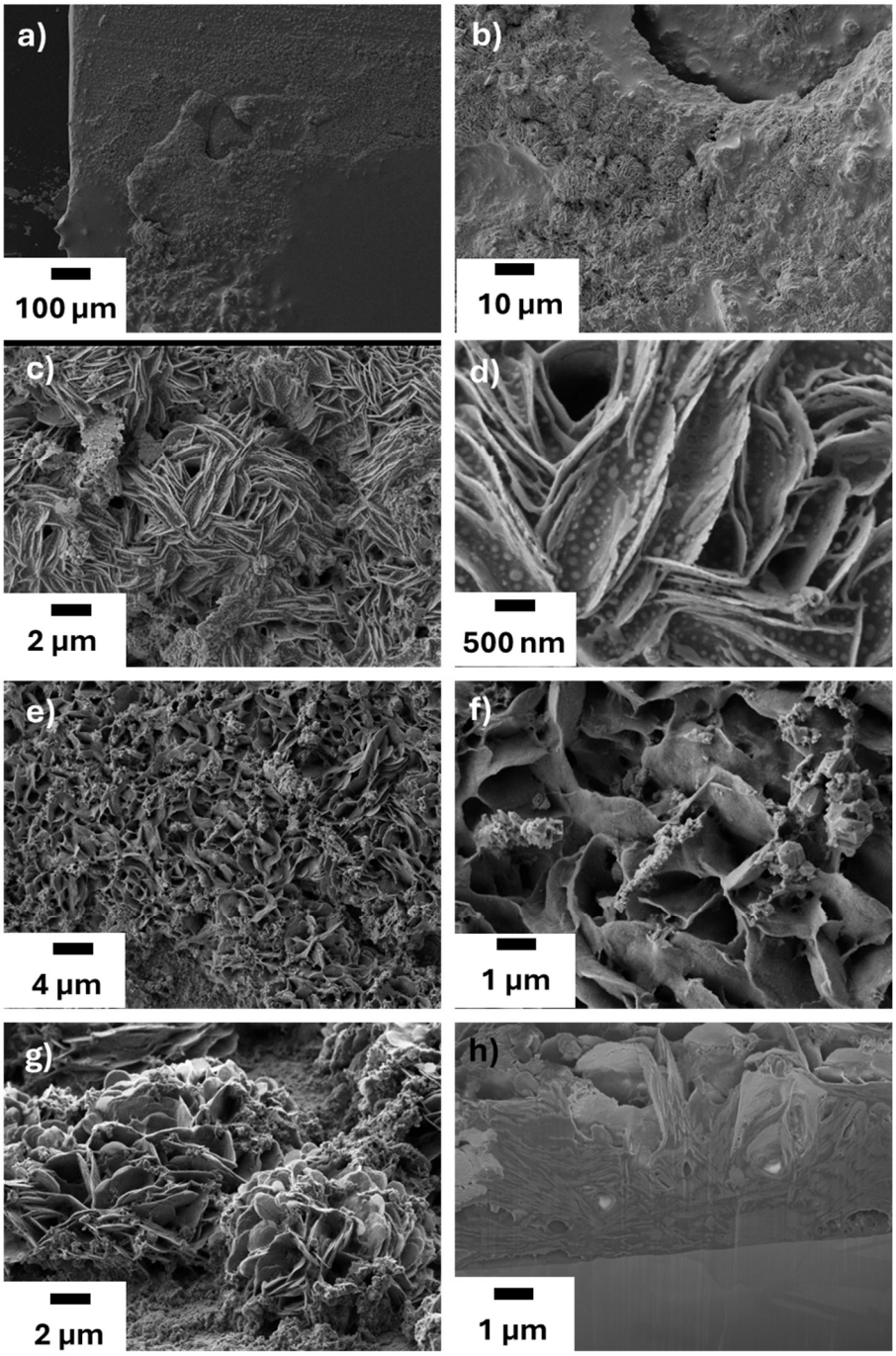

Figure 5.4, (a-g) secondary electron images of a Cu electrode after 50 galvanostatic cycles, as shown in Figure 5.3b, and (h) a cross section of the deposits on the electrode surface.

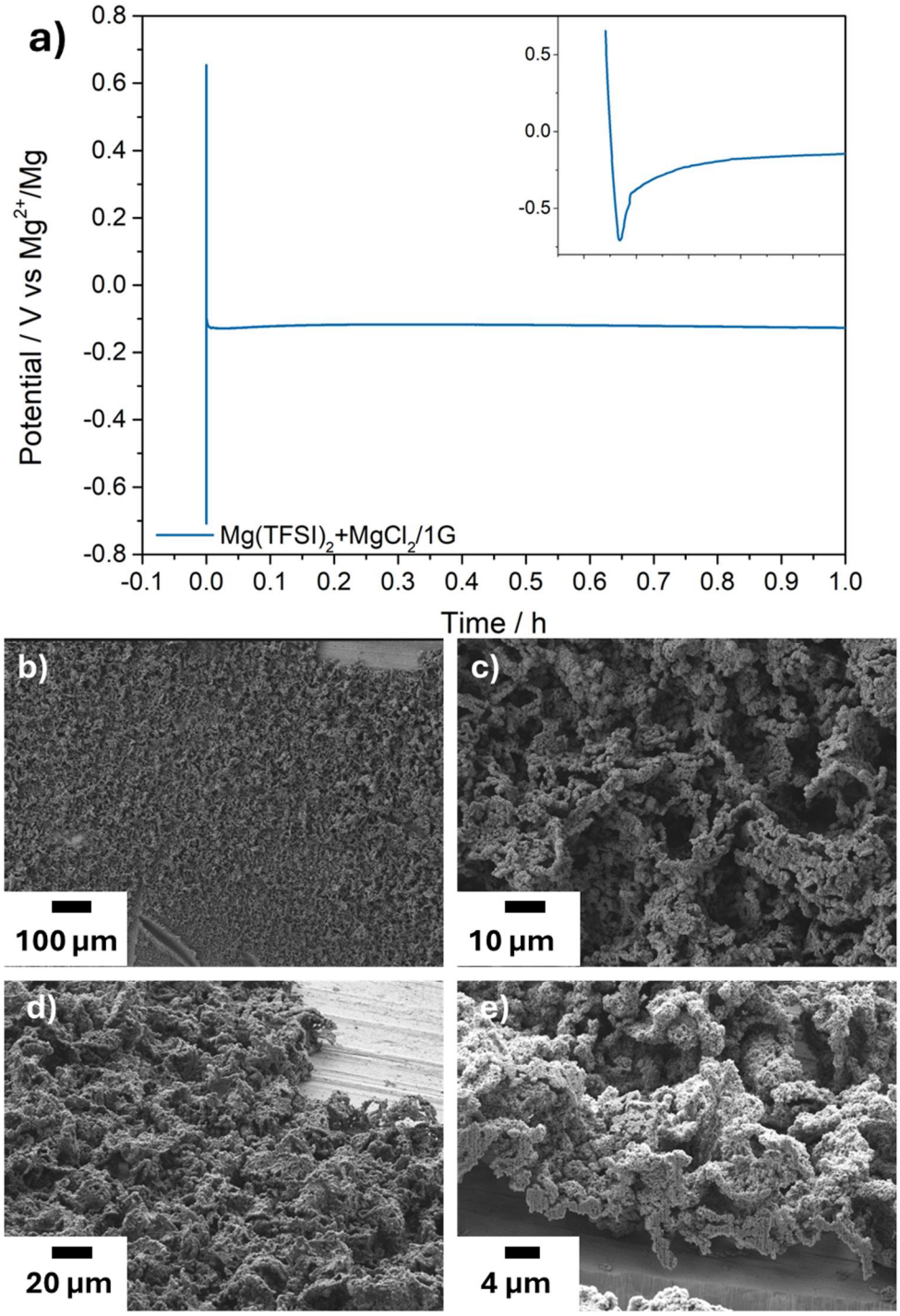

Figure 5.5 (a) galvanostatic cycling of 1 hr plating of Mg onto an electrode surface, with the insert showing the overpotential dip and (b-e) the respective SEM images and FIB cross-section.

To see the surface structures that formed during this 1 hr plating first step, a sample was prepared by performing that charging process and imaged with SEM, as shown in Figure 5.5. The cycling, as before, shows an initial

overpotential spike, -0.71 V vs Mg^{2+}/Mg before plateauing at a constant potential for plating, -0.11 V vs Mg^{2+}/Mg., Figure 5.5a. In an ideal system, the Mg would plate as a uniform layer onto the electrode surface, whereas for this system, it is far from ideal. The SEM images, Figure 5.5b-e, show a highly porous and rough Mg deposit structure formed on the Cu electrode. The Mg has grown in a sponge-like manner with a network of interconnected structures. From the cross-section, this structure is highly porous both within the Mg deposits and between them. The morphology of the structures formed suggests uncontrolled growth of the Mg structure from several different nucleation points, which have then combined as the structure grew; this is also supported by the lack of contact present between the Mg structure and the Cu electrode revealed in the FIB cross-section. The EDX map of the cross-section reveals the structure mainly composes of Mg, O and F, with C being mainly present in the structure, Figure 5.6. The presence of F and O in the same areas as Mg indicates that the plated Mg metal reacts with and degrades the electrolyte, forming MgO and MgF_2.

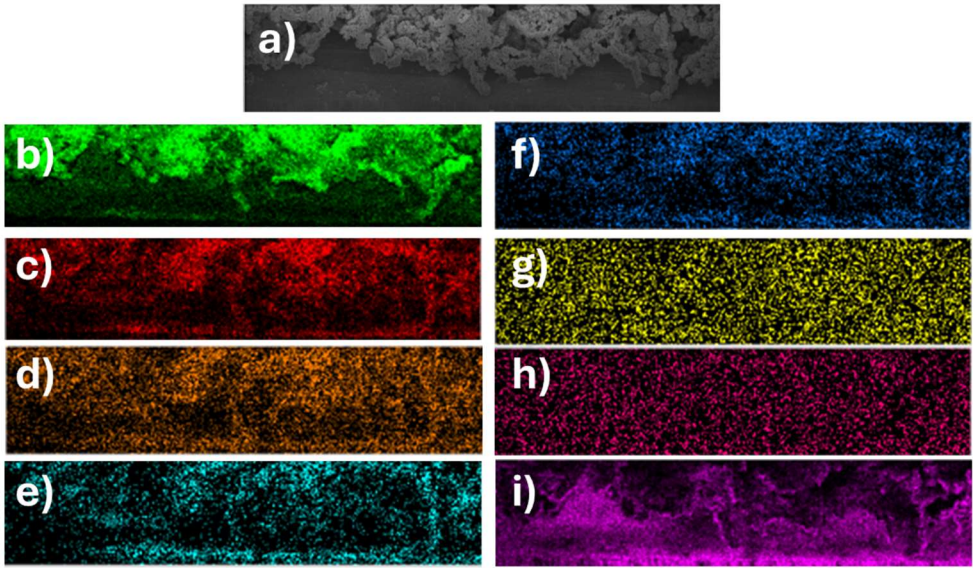

Figure 5.6, (a) SEM images of the mapped area, (b-i) EDX maps of Mg, O, F, C, N, S, Cl and Cu respectively. The imaged area is the same as that in 5.5e.

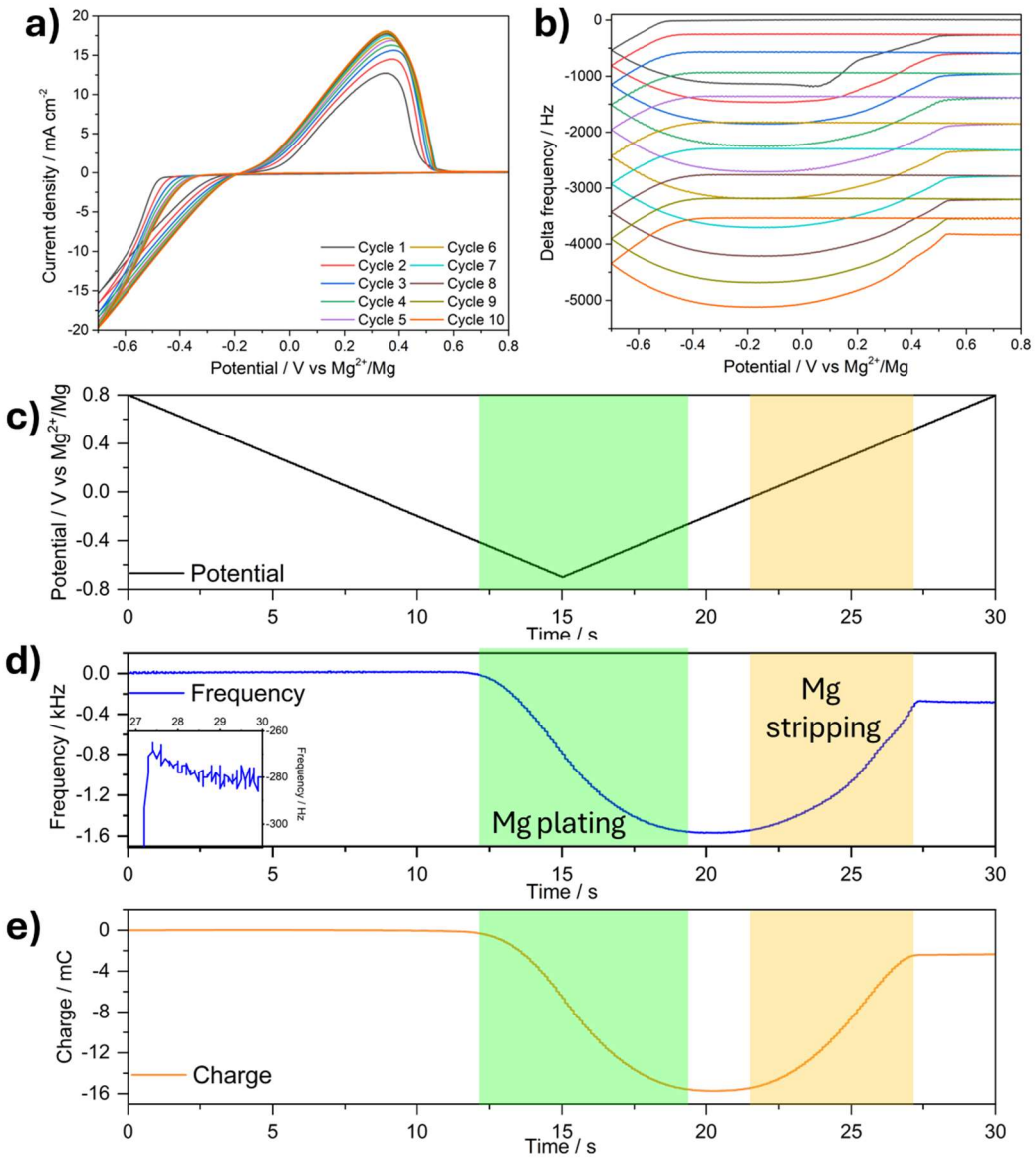

Figure 5.7, (a) cyclic voltammograms of $MgTFSI_2$+$MgCl_2$/1G and (b) the EQCM frequency vs potential. Time plots of (c) potential, (d) frequency and (e) charge over the 10th cycle. The insert in (d) shows the small frequency change recorded towards the end of the cycle. Cyclic voltammograms were recorded at an Au EQCM quartz crystal working electrode with a Mg counter and reference at a scan rate of 100 mV s^{-1} in the 0.25 M $MgCl_2$ and 0.125 M $Mg(TFSI)_2$ in 1G electrolyte.

The standard way of showing EQCM data involves plotting current against potential on one plot and frequency against potential on another, as shown in Figures 5.7a and b.[8,9] This is a useful way to show the data, but if there are large frequency changes in a cycle, smaller frequency change processes can be lost. Especially when plotting multiple cycles together, as shown in Figures 5.7 a and b. A useful way to plot EQCM data is against time; this makes it easier to correlate between changes in frequency and charge, Figure 5.7c-e, and can also reveal processes which otherwise aren't noticeable. For example, in Figure 5.7d, after the Mg stripping process, there is a ~15 Hz increase in the magnitude of the frequency change, indicating that the mass on the electrode is increasing. When this is compared to the charge vs time plot, Figure 5.7e, it shows that this change in frequency doesn't correlate to a passing of charge, meaning this process involves some reaction between the plated Mg left on the surface and the electrolyte.

More of these plots are shown in Figure 5.8a, c, e and g. Plotting them all on the same graphs allows direct comparison between the change in frequency and change in charge to see any correlation and allow the coulombic efficiency and stripping efficiency for each cycle to be compared, Figure 5.9. Another useful plot is having frequency vs charge, Figure 5.8b, d, f and h; this allows for a direct correlation between the frequency change and any electrochemical process as well as allowing for a mechanistic insight into the processes happening depending on the gradient of the plots. The ideal system would have a forward and reverse line, which have the same constant gradient returning to 0,0. This would indicate that Mg has been constantly plated as negative current is passed, and then the reverse stripping process removes all the plated Mg with no side reactions.

Doing these plots over multiple cycles shows how the mechanisms that occur during the electrochemical experiments change, Figure 5.8. Overall, for the first cycle, Figure 5.8a and b, the coulombic efficiency and the stripping efficiency are the same, at 77.5 %. Looking at the frequency and charge vs time plots it can be seen that although they have the same efficiency, some variation in

processes is observed. This is especially true in the lowest points of both plots, between 17 and 24 s. At the dip in charge, it plateaus, meaning no current is being passed, but at the end of this plateau, there is an increase in the frequency magnitude, indicating a mass increase of the electrode. This mass increase is likely due to the passivation of the freshly plated Mg surface through degradation reactions with the electrolyte, as no charge is passed, so it is a chemical process instead of an electrochemical process.

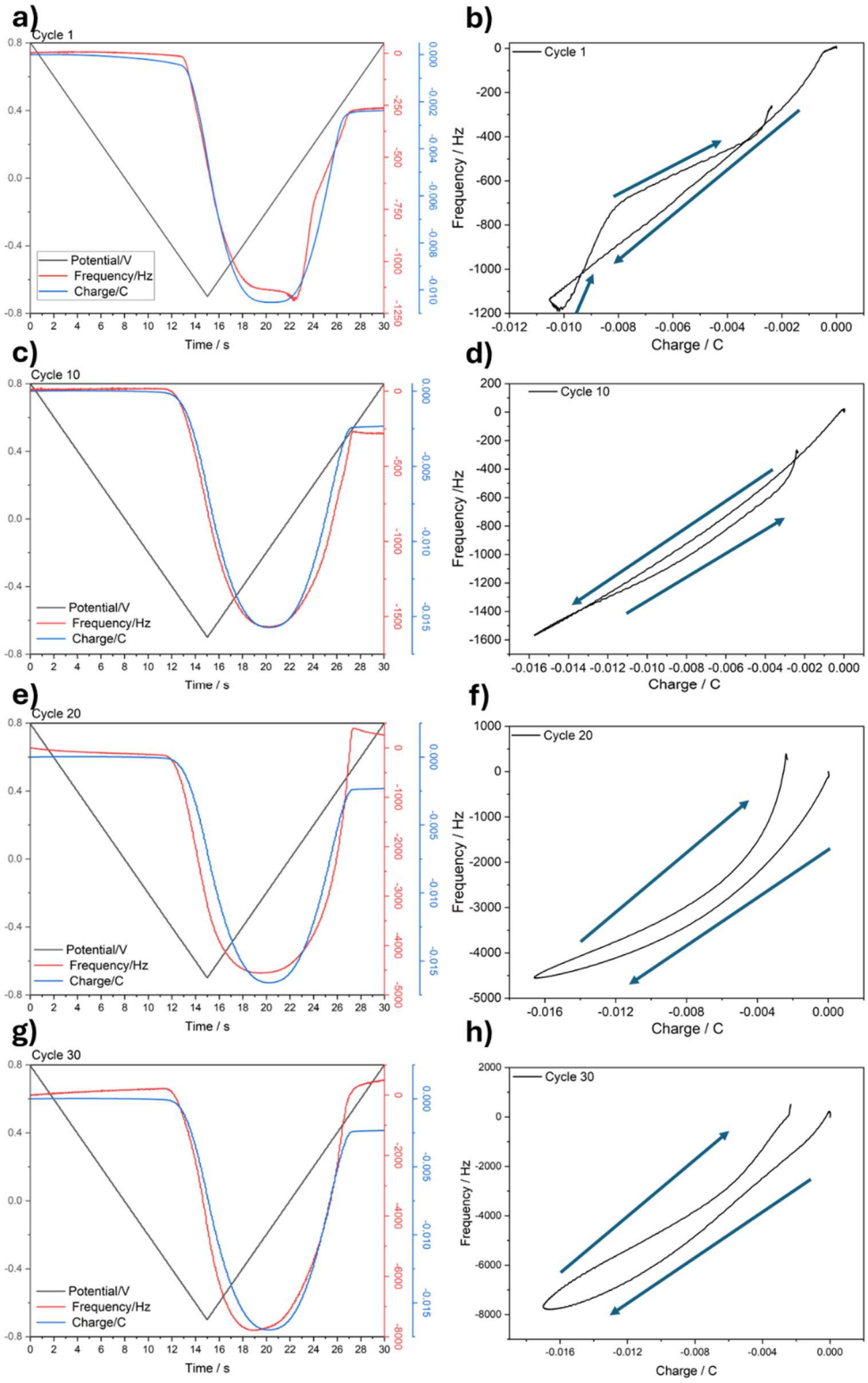

Figure 5.8, (a,c,e,g) plots of potential, frequency and charge vs time plots at cycles 1, 10, 20 and 30, respectively and (b,d,f,h) The frequency charge plots for those cycles, respectively. The EQCM measurement was recorded at an Au EQCM quartz crystal working electrode with a Mg counter and reference at a scan rate of 100 mV s^{-1} in the 0.25 M $MgCl_2$ and 0.125 M $Mg(TFSI)_2$ in 1G electrolyte.

The processes can be more clearly seen in the frequency vs charge plot. The initial slope, starting at 0,0, has a consistent gradient till the frequency reaches~1150 Hz, the constant gradient implies a consistent deposition of Mg occurs. Then after the Mg has all been plated, there is an increase in frequency magnitude again as the charge magnitude decreases from its maximum. This is likely caused by electrolyte degradation. There is then a steep decrease in the frequency magnitude, the gradient of this process is steeper than that of the plating of Mg, this implies that another process is taking place alongside the stripping of Mg. This additional process is likely the dissolution of deposits from the electrode surface, this is also observed following the experiment with black particles dispersed in the solution. The gradient then shallows from this point, meaning more charge is passed relative to the frequency change. This is likely due to some Mg being stripped, leading to a general decrease in frequency, and fresh Mg reacting with the electrolyte to form degradation products like MgO, MgS and MgF_2. At the end of cycling, there is a small decrease in the frequency magnitude, this likely due to the dissolution of surface structures from the electrode surface.

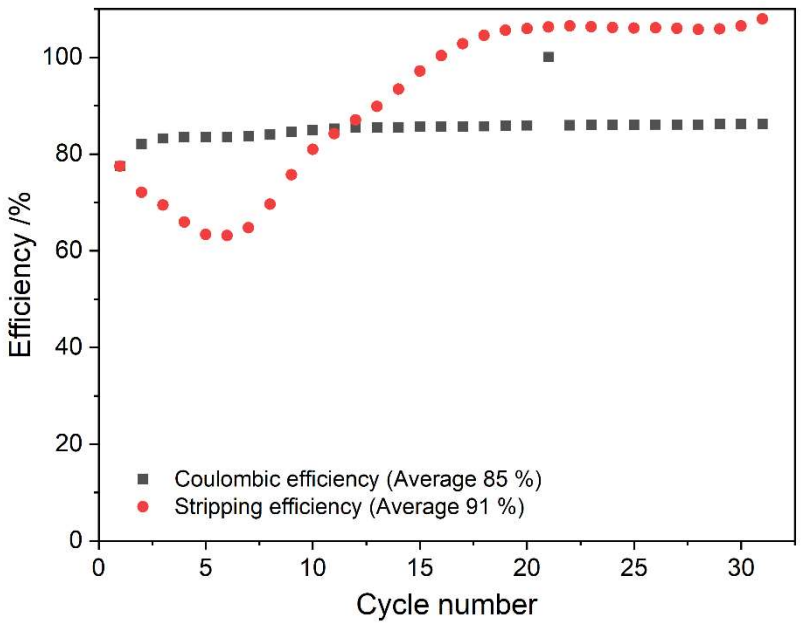

Figure 5.9, Coulombic efficiency and stripping efficiency of EQCM measurement.

For the tenth cycle, the efficiency for the charge and stripping is 85 % and 80 %, respectively, Figure 5.9. The time plot for cycle 10, Figure 5.8c, shows that the charge and frequency follow the same trends, only deviating slightly at the end of cycling, leading to a slighter higher CE. The frequency charge plot for the tenth cycle, Figure 5.8d, is close to ideal; the gradient for both the deposition and plating are almost equal, the gradient for the stripping being slightly lower, which is likely due to the stripping of Mg and the passivation of fresh Mg. At the end of the cycle, there is a decrease in the frequency magnitude but a smaller change in charge. This is likely from the dissolution of surface structures loosely bound to the electrode surface.

The twentieth and thirtieth cycles follow similar trends in their efficiencies and plots. The coulombic efficiency and stripping efficiency are 86 % and 106 %, respectively. The higher stripping efficiency is likely due to trapped Mg from earlier cycles being stripped due to the removal of passivating layers through repeated plating and stripping, leading to a stripping efficiency of >100 %. The steeper gradient at the start of the frequency charge plots, Figure 5.8 f and h, would be caused by the plating of Mg then reacting to form MgO, MgS or MgF_2 as there is a larger rate of frequency magnitude increase when compared to the charge. The lower gradient following this is likely from bulk Mg deposition onto the electrode surface, and the initial shallow gradients on the return are again from the stripping of Mg, revealing fresh Mg, which then reacts to form degradation products. Then, they both end with a slightly steeper gradient, corresponding to the stripping of some Mg and the dissolution of poorly connected surface structures on the electrode surface.

When looking at the coulombic efficiency over the 30 cycles recorded, there is a slight increase over the first few cycles, likely the conditioning process, before levelling at 86 % for the remaining cycles. On the other hand, the stripping efficiency has a very different trend. During the first 6 cycles, the stripping efficiency decreases from 77 % to 63 %. This decrease in stripping efficiency is likely due to removing impurities in the electrolyte during the first few cycles, which causes products like MgO and MgF_2 which can’t be

electrochemically stripped from the surface and trap active Mg underneath this inactive layer. From cycle 6 to 20, the efficiency then increases from 63 % to 106 %. This gradual increase is likely due the reversible stripping of Mg over time and increases the stripping efficiency over multiple cycles. The reason the efficiency goes over 100 % is probably due to some of the Mg metal trapped in earlier cycles becoming free and able to be stripped. The average efficiency for the stripping of Mg over the 30 cycles is 95 %. The higher stripping efficiency than coulombic efficiency implies that the lost charge is involved in other processes which aren't detectable using EQCM.

5.2.2 Structural evolution of the Cu electrode surface

The main contributor to the improvement in performance in this electrolyte is the $MgCl_2$. It facilitates higher coulombic and stripping efficiencies than in the other electrolytes screened in Chapter 4, apart from $Mg[B(hfip)_4]_2$. With this fact, it's surprising that with the EDX maps of the electrode surface, relatively small amounts of chloride are seen to have no distribution pattern, and appear as noise in the map, Figure 4.14i. Potentially, the chloride was being washed off with an organic layer. Thus, another sample was imaged, which was gently washed to preserve any organic layers on the surface which might contain the chloride species, Figure 5.10.

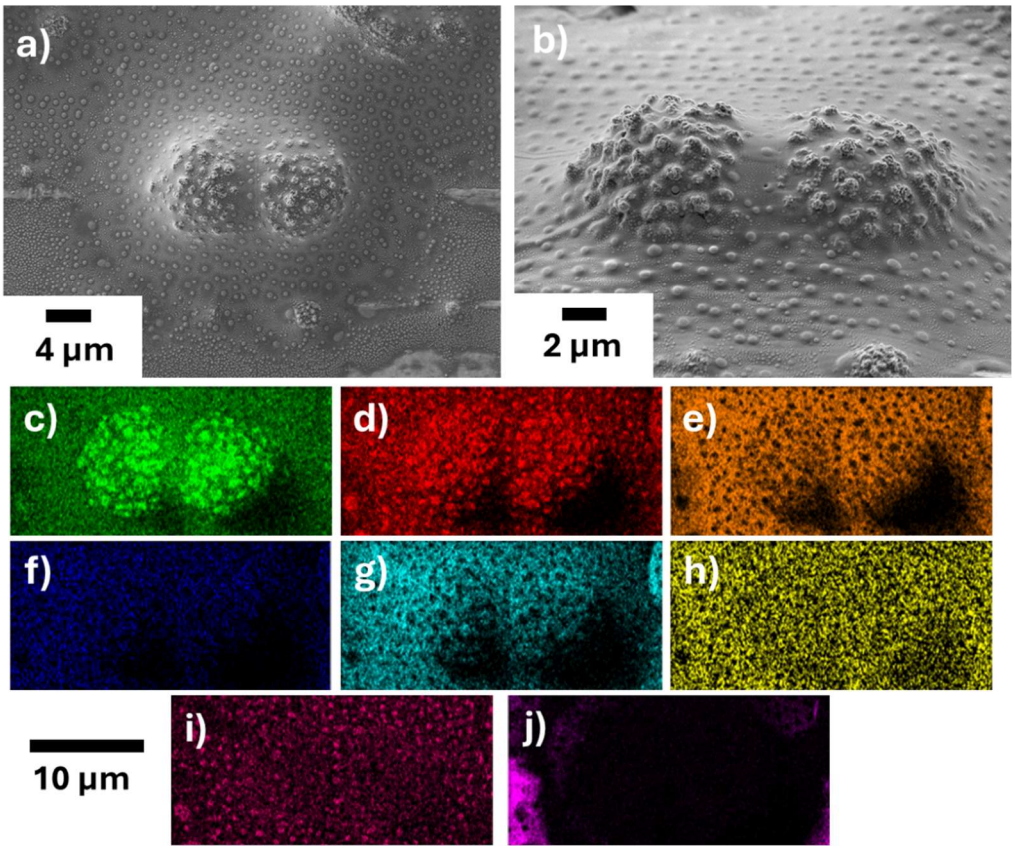

Figure 5.10, (a and b) SEM of a cycled Cu electrode after 30 cycles between -0.7 and 0.8 V vs Mg^{2+}/Mg, at a scan rate of 100 mV s^{-1} for $MgTFSI_2$+$MgCl_2$/1G electrolyte system (c-j) corresponding EDX maps for (c) Mg, (d) O, (e) F, (f) N, (g) C, (h) S, (i) Cl and (j) Cu, all with a scale bar of 10 µm

These SEM images show a film covering most of the electrode surface, Figure 5.10a, which still has the hemispherical structures seen in the previous chapter

underneath. The film is covered with small, round structures from 1 µm to 10's of nm in size. When EDX mapping this area, the EDX maps are rich with elements that previously appeared in relatively low quantities, Figure 4.14, F, C, S and, importantly, Cl, Figure 5.10 and 5.11. The Cl is heavily concentrated in these small round structures littering the film, which mainly contains C, F and S, suggesting that this film is made from degradation products of the $TFSI^-$ anion. Along with these round structures containing mainly Cl, they also have high intensities of O in the EDX maps whilst being deficient in F, S and C, indicating that these structures are potentially implanted in the film. The Cl and O in the film can be seen more easily in the cross-sectional image and EDX maps, Figure 5.11. It also shows the film covering the deposit, and even with the film covering the electrode, the internal layered, onion-like structure remains.

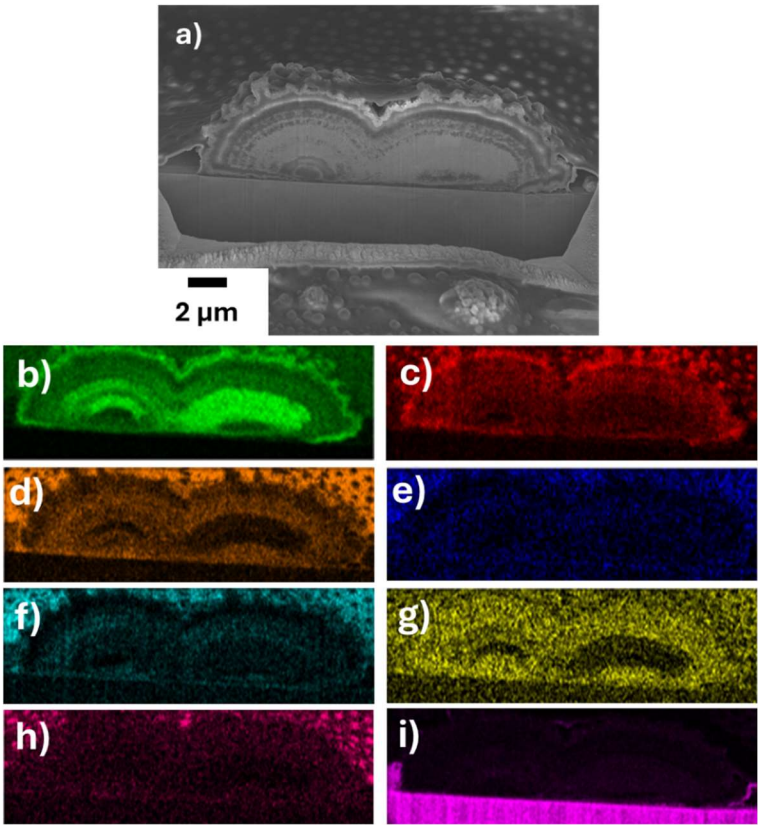

Figure 5.11, (a) SEM of a cycled Cu electrode after 30 cycles between -0.7 and 0.8 V vs Mg^{2+}/Mg, at a scan rate of 100 mV s^{-1} for $MgTFSI_2+MgCl_2$/1G electrolyte system (b-h) corresponding EDX maps for (b) Mg, (c) O, (d) F, (e)N, (f) C, (g) S, (h) Cl and (i) Cu, all to the same scale as the SEM image which has a scale bar of 2 µm

So far, this work has looked at the electrochemical characteristics of this electrolyte system and the surface structures at the microscale. However, as in Chapter 3, there is more structural information to be gained by looking at these structures at the nanoscale to gain more insight into the cycling mechanism. The cross sections revealed so far show a layered onion like structure with hollow sections between each layer. These hollow sections are likely where the Mg is stripped from but so far the SEM images give no indication as to how Mg is transported through the passivating layer. These details can only be discovered at the nanoscale and thus another lift out was performed. The lift-out process is shown in Figure 5.12, with a difference from the previous method being that instead of directly attaching the micromanipulator to the sample, a piece of copper is connected to the micromanipulator, and then the platinum is used to connect the lamella to the copper. This method helps prolong the lifetime of the micromanipulator needle.

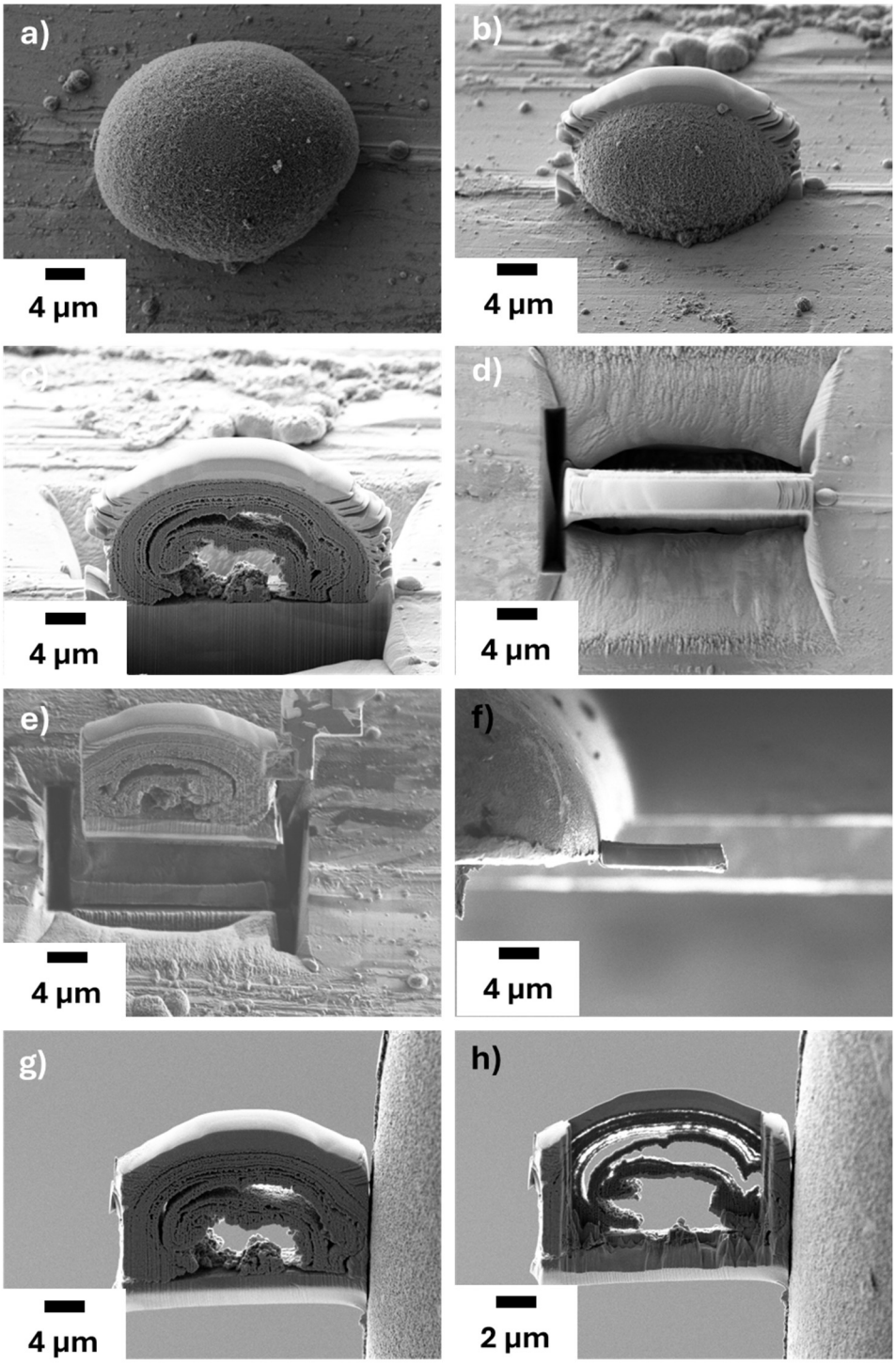

Figure 5.12, (a-h) SEM images of the lift out process and lamella thinning for the discharged sample of the 0.25 M $MgCl_2$ and 0.125 M $Mg(TFSI)_2$ in 1G electrolyte after 30 cycles.

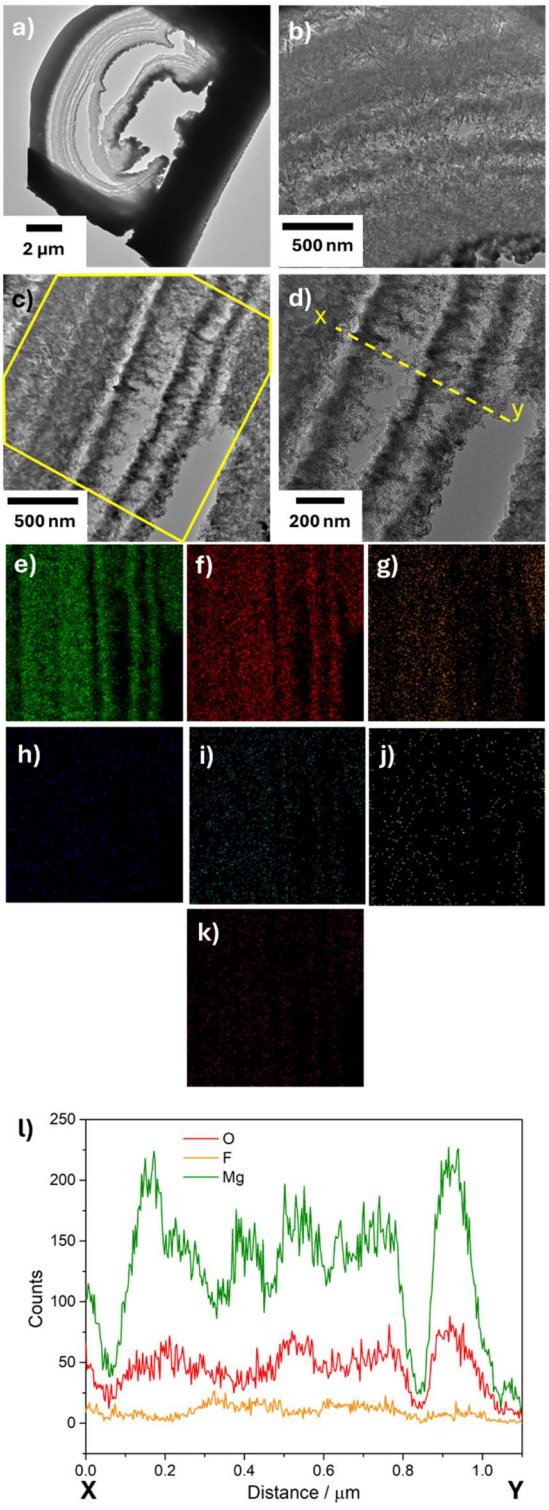

Figure 5.13, (a) low magnification TEM image of the lamella attached to the support grid, (b-d) increasing magnification images of the lamella structure. EDX maps (e-j) for (e) Mg, (f) O, (g) F, (h) N, (i) C, (j) S and (k) Cl for the area in the yellow box in (c). (k) line scan between points X and Y in image (d)

Being able to image the lift-outs of the deposits helps to show their complex structure in more detail. Low magnification TEM images, Figure 5.13a, show that most lamella are thin enough to be imaged via TEM. The lamella is also structurally sound, with no breakages or bending, as seen in Chapter 3. The increased magnification images, Figure 5.13b-d, show the layered structure in more detail and that each layer is about 100 – 150 nm thick, with the gap between layers varying from 10s to 100s nm. The EDX maps of the area outlined in Figure 5.13c show these layers mostly contain Mg, O and F, supporting the assumption that these layers mainly contain MgO and MgF_2. The EDX maps for the other elements present, C, N, S and Cl, show very little amounts present compared to Mg, O and F, Figure 5.13h-k. The line scan in Figure 5.13h shows that the Mg and O appear together throughout the layers but not at a 1:1 ratio, and even considering the F signal, there would still be Mg metal left in the structure. This implies that the layers are made up of Mg metal trapped within the structure by MgO and MgF_2.

Higher magnification TEM images are required to determine the crystalline or amorphous deposit structures. These images, Figure 5.14, show a lot of information about the deposit structure, which previously, with just SEM, could not be revealed. They show a highly crystalline structure, and these crystal domains are a few nanometres in size and all with clear d-spacings, Figure 5.14a. The high magnification image in Figure 5.14a also shows an interphase, a few layers thick, on the surface of the deposit, with the boundary being outlined by the red dashed lines. This shows that the interphase on each layer deposited is in the region of a few nanometres thick. The d-spacings present correlate to MgO (2.21 Å, 2.39 Å) and MgF_2(1.95 Å, 3.4 Å).[4,10–13]

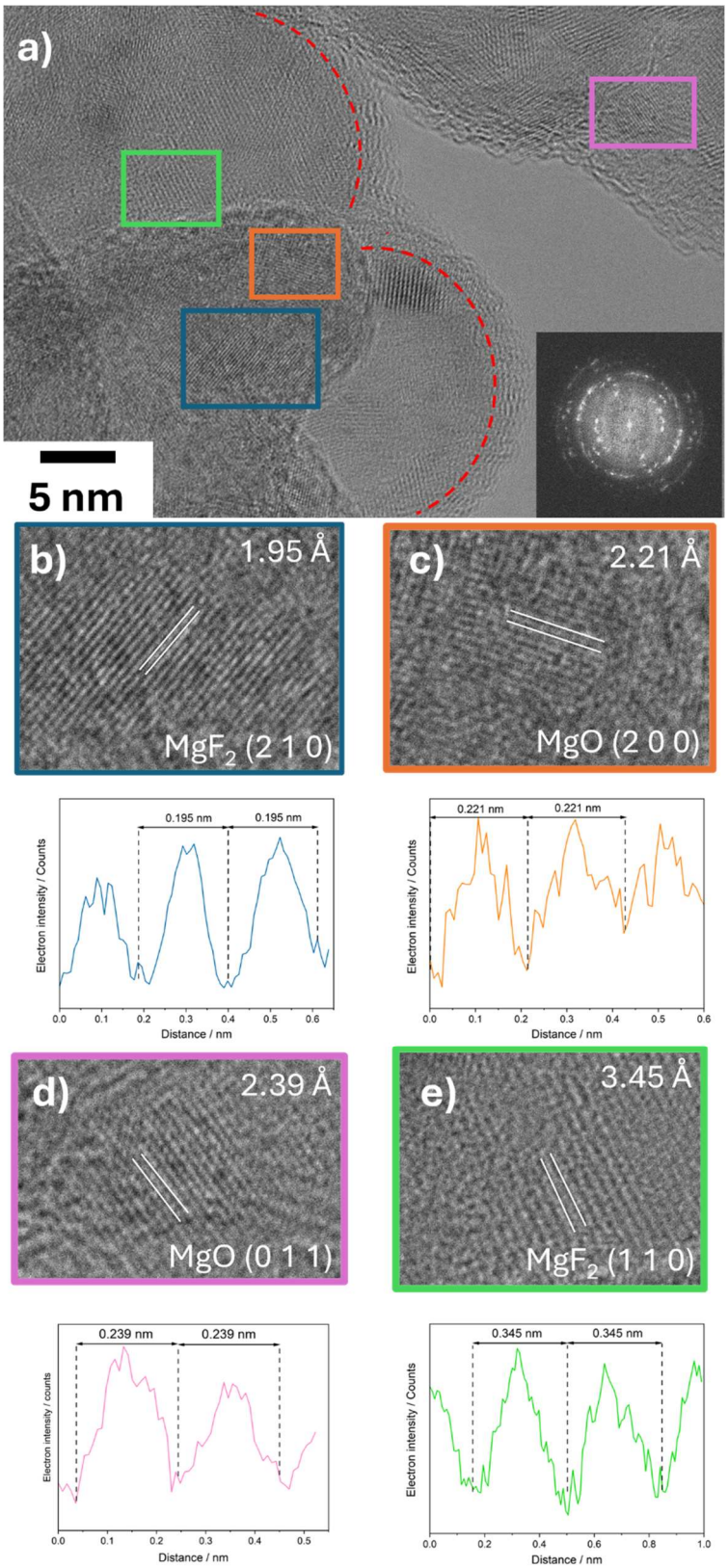

Figure 5.14, (a) high-resolution TEM image of the interphase between layers of the lamella with the insert being the diffraction pattern for the image. (b-e) magnified areas in (a) highlighting the d-spacings present with graphs of electron intensity across the areas showing the d-spacing and crystal planes as well.

One final unanswered question that the high-magnification TEM images answer is how the Mg is able to diffuse through the structure. After being plated and the surface Mg passivated, if this was impermeable, the deposits would be solid, and the stripping efficiency would be considerably lower. TEM images show hollow tube-like structures through the layers; Figure 5.15 shows a tilt series of one of these tubes. These structures likely allow for the transport of Mg through the layers, meaning they are conductive with respect to Mg^{2+} ions.

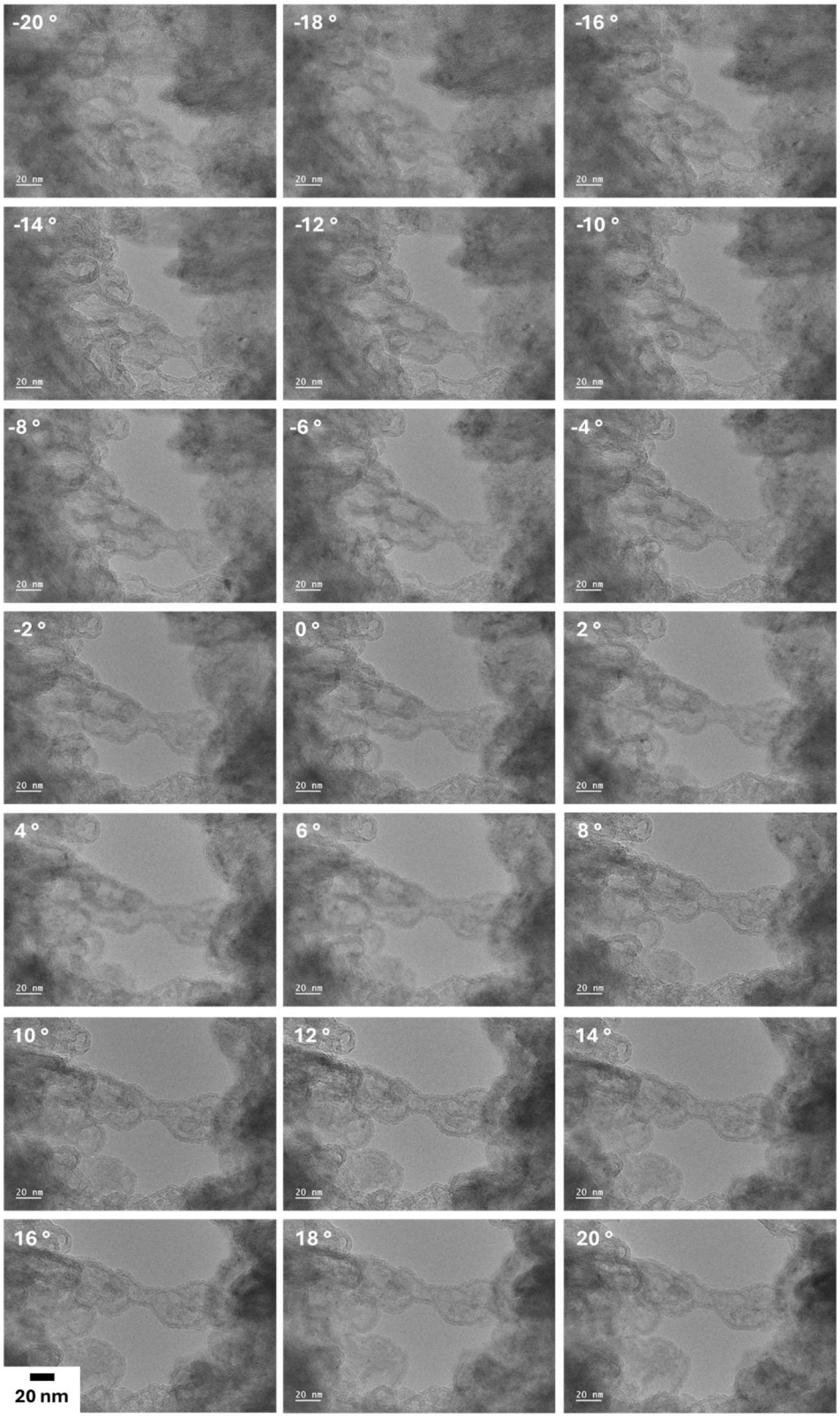

Figure 5.15, A tilt series from -20 ° to 20 ° for a tubular structure between Mg layers, with the number in the image being the tilt angle.

5.3 Conclusions

Using new workflows from previous chapters and advanced electrochemical analysis has provided several insights into the performance of chloride-containing electrolytes, particularly concerning their plating and stripping efficiency. The cyclic voltammetry with variable scan rates demonstrated that at slower experiment times, the surface Mg reacts with the electrolyte, hindering efficiency. Galvanostatic cycling further confirmed these findings, showing shorter cycle time yielded higher efficiencies by minimising the chance for electrolyte degradation. Electrochemical quartz crystal microbalance measurements highlighted the mechanical and electrochemical processes occurring during plating and stripping, showing that while high initial efficiencies are achievable, electrolyte degradation products hinder long-term reversibility.

Surface analysis with SEM and XPS revealed the progressive evolution of the electrode surface through cycling, transitioning from an organic-dominated layer to a more inorganic layer over consecutive cycles. The analysis also showed the organic film that forms over the electrode surface and the role that chloride plays, where previously, it wasn't very present in EDX mapping.

TEM analysis of the Mg deposits further showed the layered structure in more detail, with each layer approximately 100–150 nm thick and varying gaps between them. EDX mapping confirms the significant presence of Mg, O, and F in the layers, indicating the composition of MgO and MgF. Notably, residual Mg metal is still present within these layers. High-resolution TEM images show a crystalline structure with clear d-spacings for the nanoscale crystal domains which make up the deposit structure. The high-resolution images also show a six-layer thick organic interphase covering the surface of the deposit structure. This data provides valuable insight into the structural integrity and composition of the Mg deposits at the nanoscale.

5.4 Experimental

5.4.1 Chemicals

Dimethoxy ethane (DME or 1G) (Sigma Aldrich, 99 %), magnesium chloride ($MgCl_2$) (Sigma Aldrich, 99.9 %) and magnesium bis(trifluoromethanesulfonyl)imide ($Mg(TFSI)_2$) (Solvionic, 99.5 %) were all used as supplied and stored in a N_2 glovebox (O_2 <0.1 ppm, H_2O < 0.1 ppm). The electrolyte was made by dissolving 0.25 M $MgCl_2$ and 0.125 $Mg(TFSI)_2$ in 1G.

5.4.2 Electrochemical experiments

All electrochemical experiments were performed inside an N_2 glovebox. Before use all glassware was cleaned and dried overnight at 70 °C under vacuum. Cyclic voltammetry and galvanostatic measurements were recorded on a Biologic SP-300 potentiostat using three electrodes: a Cu ribbon (Sigma-Aldrich) working electrode and an Mg ribbon (Sigma-Aldrich) counter and reference. The Mg ribbons were scratched beforehand to remove the oxidised layer and reveal the fresh Mg surface. The copper foil was cut into ribbons and dried at 120 °C under vacuum before being stored in the glove box.

EQCM experiments were performed with a CHI 450 potentiostat. The working electrode was either a gold or copper EQCM crystal (CH Instruments, United States of America) inside a PTFE cell, as shown in the diagram in Figure 2.1b.

5.4.3 Surface characterisation

Before surface characterisation, the cycled Cu electrodes were washed with DME (Sigma-Aldrich, purity 99.5%) (dried using 4 Å molecular sieves) and dried under vacuum for 30 minutes in a glovebox mini-antechamber. For transferring samples into the Zeiss Crossbeam 550 FIB-SEM (Carl Zeiss, Germany), the samples were loaded air-free from the glovebox using a Quorum PP3006 CoolLok Transfer port mounted directly onto the glovebox. The sample was transferred to a Quorum PP3010 FIB/SEM Preparation system before being loaded into the SEM chamber. SEM images were taken at an accelerating voltage of 2 kV. A Ga ion FIB source was used for milling the sample at an accelerating voltage of 30 kV with FIB currents between 50 and 700 pA. EDX

analysis was performed with an Oxford Instruments Ultimax 170 X-ray microanalysis detector (Oxford Instruments, UK) and analysed using Aztec software (v 4.3) at an accelerating voltage of 5 kV. The 3D structures, cross sections and deposit volumes were generated using Dragonfly software (v 2021.3 for Windows). Lift-outs of the deposits were prepared for TEM using an in-situ micromanipulator (Omniprobe 200, Oxford Instruments) and transferred to a Cu support grid (EM Resolutions) before final thinning to electron transparency.

TEM, EELS, STEM and electron beam diffraction were performed using a JEOL 2100+ TEM and a JEOL 2100F field emission gun (FEG)-TEM at an accelerating voltage of 200 kV. The samples were loaded in a glovebox and transferred to the TEM using a Gatan HHST4004-010 Environmental cell heating holder. Image analysis and electron diffraction data were analysed using Gatan Digital Micrograph software and CysTBox Server.

X-ray photoelectron spectroscopy (XPS) was performed using a SPEC DeviSims NAP-XPS instrument fitted with a Phoibos 150 hemispherical analyser equipped with a monochromatic Al Kα radiation source (1486.6 eV). All experiments were performed in the main analysis chamber under ultra-high vacuum conditions, and all samples were loaded air-free. The parameters for a typical experiment were as follows: step size 0.1 eV, dwell time 0.3 s, and a pass energy of 50 eV. Spectrum analysis was carried out using CasaXPS software. A Shirley background correction was applied to all spectra before analysis, and all spectra were charge-corrected to the adventitious carbon peak at 284.8 eV. The full width half maximum were also constrained and a Gaussian-Lorentzian distribution of 30 was used, GL(30).

5.5 References

1 Y. Man, P. Jaumaux, Y. Xu, Y. Fei, X. Mo, G. Wang and X. Zhou, *Science Bulletin*, 2023, **68**, 1819–1842.

2 D. J. Wetzel, M. A. Malone, R. T. Haasch, Y. Meng, H. Vieker, N. T. Hahn, A. Gölzhäuser, J.-M. Zuo, K. R. Zavadil, A. A. Gewirth and R. G. Nuzzo, *ACS Applied Materials & Interfaces*, 2015, **7**, 18406–18414.

3 H. D. Yoo, S.-D. Han, I. L. Bolotin, G. M. Nolis, R. D. Bayliss, A. K. Burrell, J. T. Vaughey and J. Cabana, *Langmuir*, 2017, **33**, 9398–9406.

4 K. Dimogiannis, A. Sankowski, C. Holc, C. D. J. Parmenter, G. N. Newton, D. A. Walsh, J. O'Shea, A. N. Khlobystov and L. R. Johnson, *Energy Storage Materials*, 2024, **67**, 103280.

5 P. Canepa, G. Sai Gautam, D. C. Hannah, R. Malik, M. Liu, K. G. Gallagher, K. A. Persson and G. Ceder, *Chem Rev*, 2017, **117**, 4287–4341.

6 R. Mohtadi and F. Mizuno, *Beilstein Journal of Nanotechnology*, 2014, **5**, 1291–1311.

7 R. Attias, B. Dlugatch, O. Blumen, K. Shwartsman, M. Salama, N. Shpigel and D. Sharon, *ACS Appl. Mater. Interfaces*, 2022, acsami.2c08008.

8 W.-Y. Tsai, P.-L. Taberna and P. Simon, *J. Am. Chem. Soc.*, 2014, **136**, 8722–8728.

9 M. Biermann, C. Leppin, A. Langhoff, T. Ziemer, C. Rembe and D. Johannsmann, *Analyst*, 2024, **149**, 2138–2146.

10 L.-P. Zenser, R. Gruehn and B. H. Liebscher, *Journal of Solid State Chemistry*, 2001, **157**, 30–39.

11 K. D. Salman, H. H. Abbas and H. A. Aljawad, *J. Phys.: Conf. Ser.*, 2021, **1973**, 012104.

12 P. Jain, V. Dixit, A. Jain, O. Srivastava and J. Huot, *Energies*, 2015, **8**, 12546–12556.

13 G. Zhang, X. Fu, S. Song, K. Guo and J. Zhang, *Coatings*, 2019, **9**, 834.

Conclusions and Future Work

The research field of magnesium batteries is still in its early stages compared to lithium-ion battery research and has significant challenges to overcome. Some of these challenges concern the magnesium negative electrode and the surface chemistry that occurs during cycling. Surface changes through passivation and loss of active material greatly impact the cyclability of magnesium batteries and are an area lacking full understanding.

In this thesis, I've developed a workflow for analysing the electrode surface at both the micro and nanoscale. This workflow was initially tested with a simple glyme electrolyte, which didn't contain chloride ions, and showed how complex 3D structures form during cycling. These structures have intricate porosities, shown through 3D models, and have complex chemical distributions. Along with this, the changes have also been observed between states of charge which gives insights into how the structure changes and grows through progressive cycling.

Along with this, in literature, there isn't a standard methodology for comparing different electrolytes, as in literature different current densities or cycling times are used, making it hard to accurately compare different systems accurately. The work in Chapter 4 of this thesis starts to use methods on different electrolyte systems to compare them directly. Using electrochemistry and microscopy, it was shown that the best systems were $MgCl_2$ and $Mg[B(hfip)_4]_2$ containing systems, the former of which was then analysed at the micro and nanoscale using the workflow developed earlier.

Developing this work further would allow us to fully compare different electrolyte systems through more methods, such as XPS, HPLC (for electrolyte degradation products), and other spectroscopic techniques. Cryo-microscopy would also be used to image the surface structures in a close to in situ state, allowing for a better understanding of how magnesium diffuses through the structure and helping to understand the process.

Appendix

Chapter 3 appendix

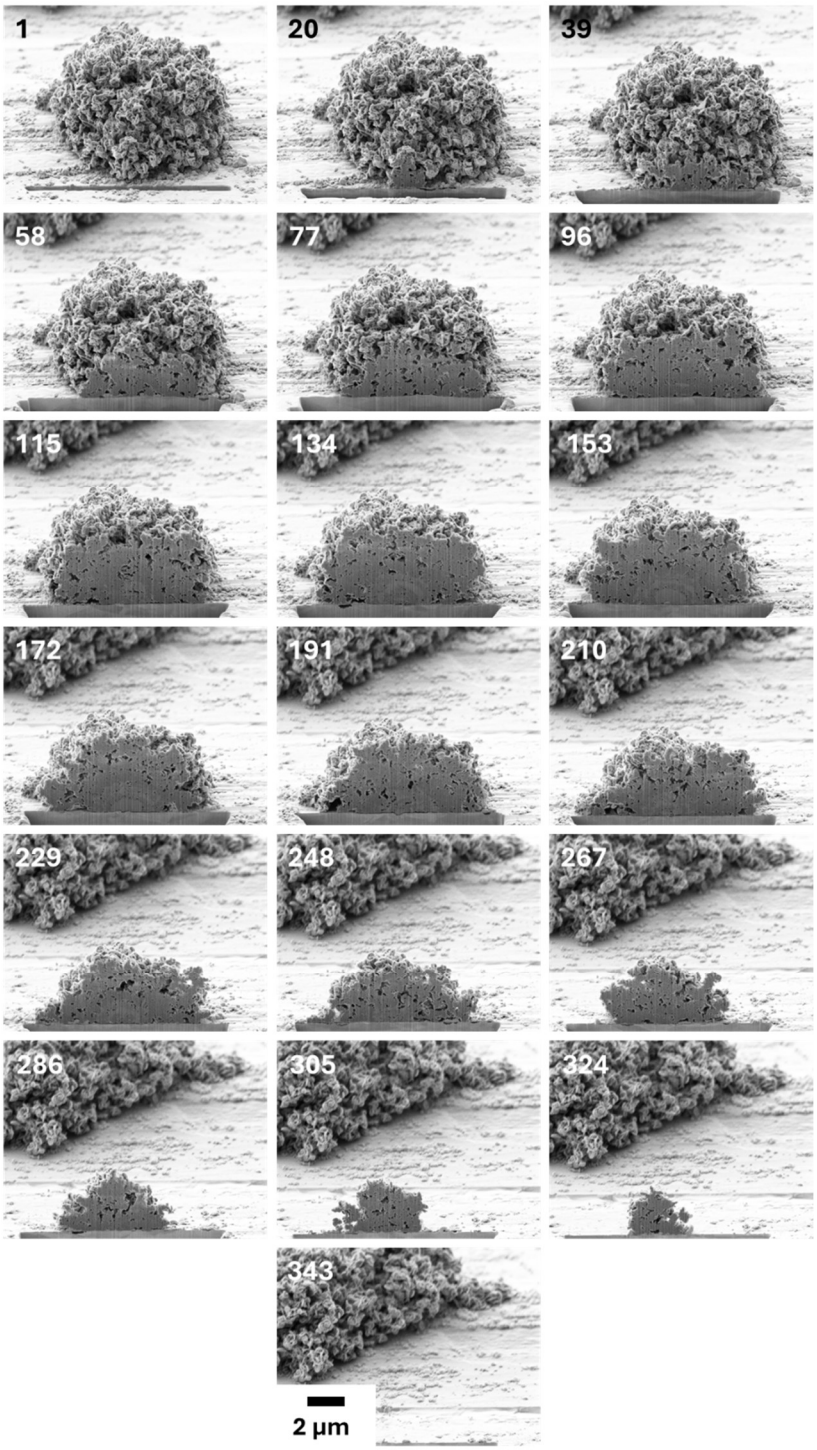

Figure A1, SEM images taken throughout the segmentation process, the number representing the slice number.

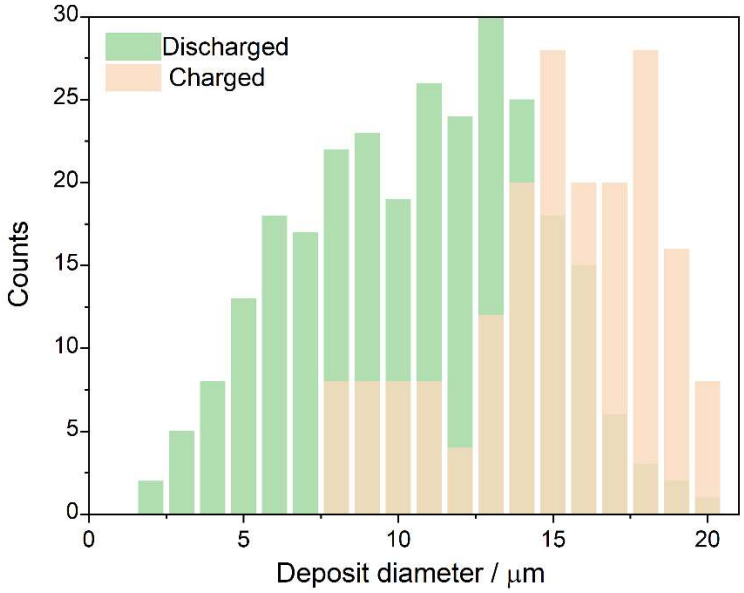

Figure A2, bar chart showing the size distributions of charged and discharged deposits after 30 cycles.

Chapter 4 appendix

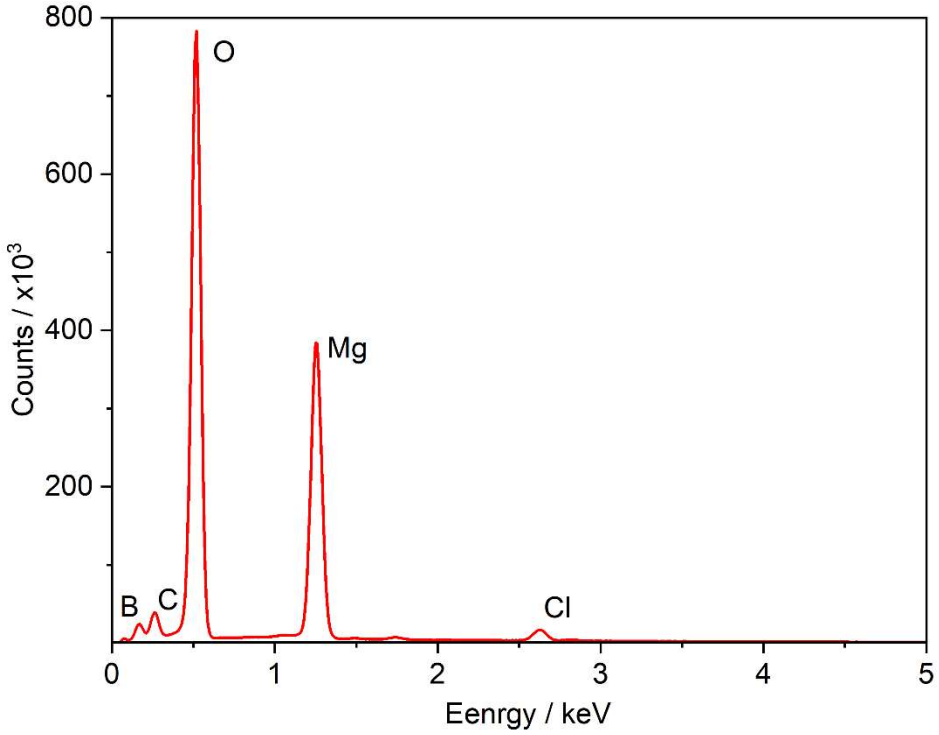

Figure A3, EDX spectra of $Mg(BH_4)_2$.

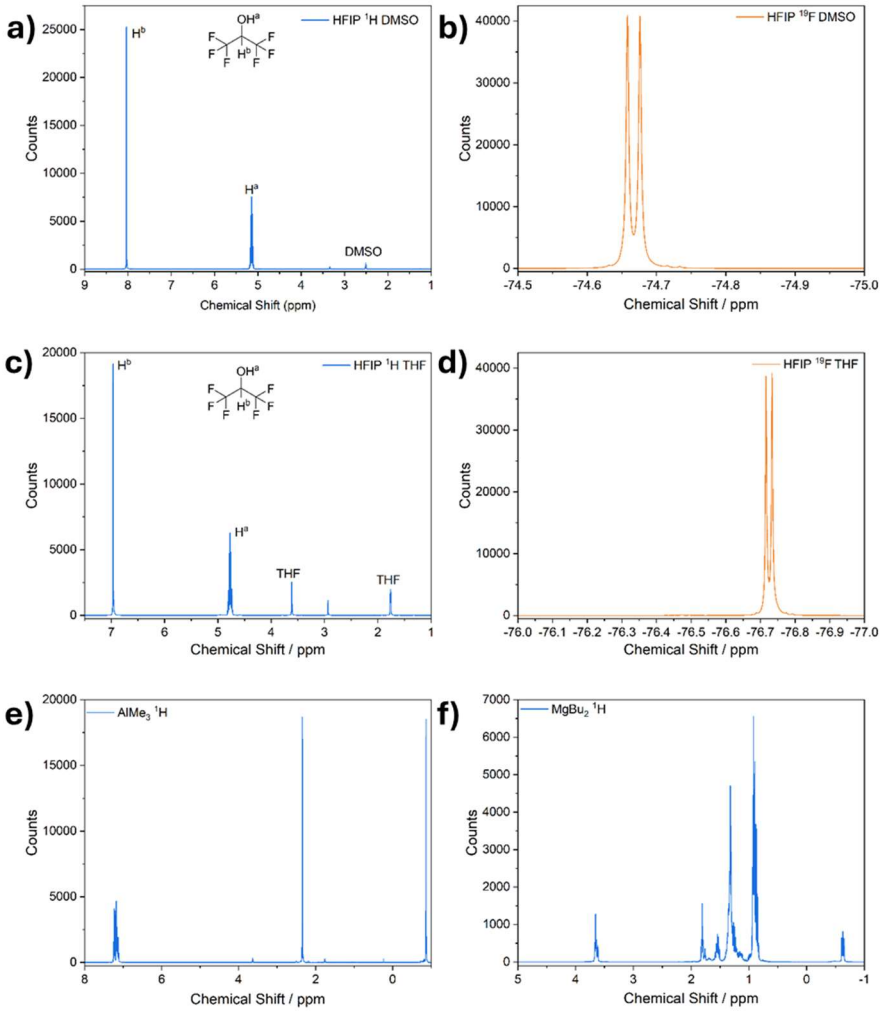

Figure A4, (a) ^{1}H NMR spectrum of HFIP in DMSO-d_6, (b) ^{19}F NMR spectrum of HFIP in DMSO-d_6, (c) ^{1}H NMR spectrum of HFIP in THF-d_8, (d) ^{19}F NMR spectrum of HFIP in THF-d_8, (e) ^{1}H NMR spectrum of $AlMe_3$ in DMSO-d_6 and (f) ^{1}H NMR spectrum of $MgBu_2$ in DMSO-d_6.

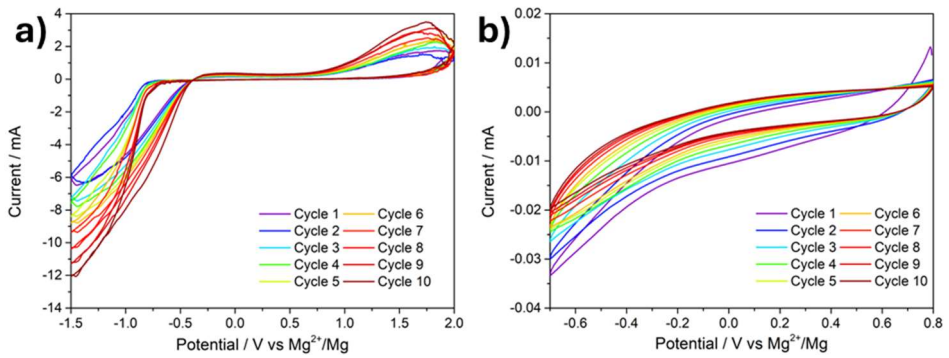

Figure A5, Cyclic voltammetry of (a) 0.5 M $MgTFSI_2$ in 1G and (b) 0.5 M $MgTFSI_2$ and 10 mM $Pry_{14}TFSI$in 1G.All CVs were recorded at a Cu working electrode with a Mg counter and reference, and at a scan rate of 100 mV s^{-1} over 10 cycles.

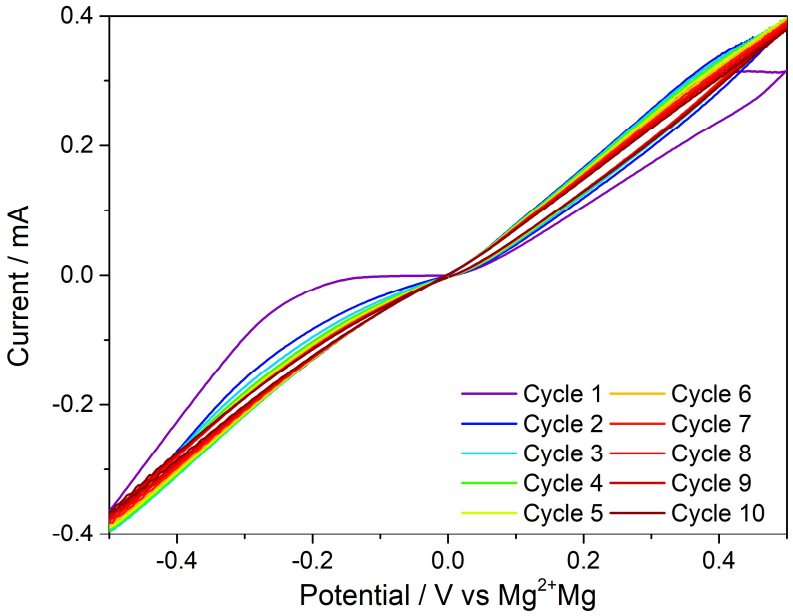

Figure A6, CV 2 M BuMgCl in THF over 10 cycles between the potential limits of 0.5 and -0.5 vs Mg^{2+}/Mg at a scan rate of 100 mV s^{-1} with a Cu working electrode and a Mg counter and reference

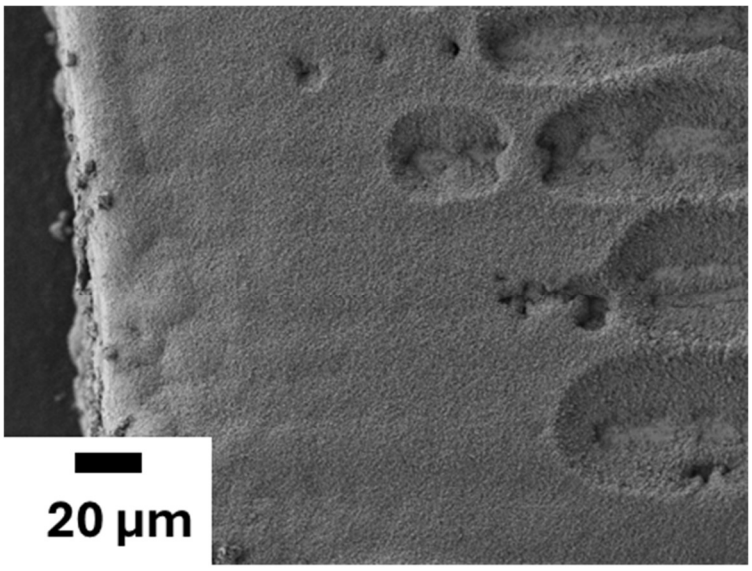

Figure A7, SEM of a cycled Cu electrode after 30 cycles between -0.7 and 0.8 V vs Mg^{2+}/Mg, at a scan rate of 100 mV s^{-1} for $MgTFSI_2$+$Pry_{14}TFSI$/2G electrolyte system.

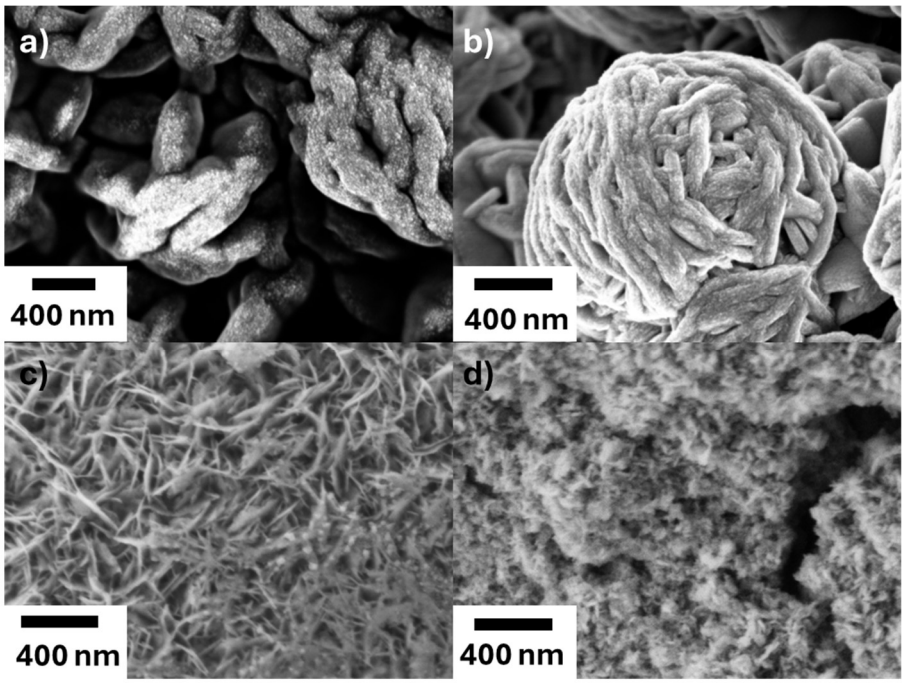

Figure A8, high magnification SEM images of (a) $MgTFSI_2$/2G (b) $MgTFSI_2$+$MgCl_2$/2G (c) $MgTFSI_2$+$MgCl_2$/1G and (d) $Mg[B(hfip)_4]_2$/1G